

A DOCTORAL DISSERTATION
PREPARED IN THE INSTITUTE OF PHYSICS
OF THE JAGIELLONIAN UNIVERSITY,
SUBMITTED TO THE FACULTY OF PHYSICS, ASTRONOMY
AND APPLIED COMPUTER SCIENCE
OF THE JAGIELLONIAN UNIVERSITY



Determination of performance characteristics of the J-PET tomograph

Monika Pawlik-Niedźwiecka

SUPERVISOR:
PROF. DR HAB. PAWEŁ MOSKAL
AUXILIARY SUPERVISOR: DR MICHAŁ SILARSKI

Cracow, 2023

ROZPRAWA DOKTORSKA
PRZYGOTOWANA W INSTYTUCIE FIZYKI
UNIwersYTETU Jagiellońskiego,
ZŁOŻONA NA WYDZIALE FIZYKI, ASTRONOMII
I INFORMATYKI STOSOWANEJ
UNIwersYTETU Jagiellońskiego



Wyznaczenie charakterystyk działania tomografu J-PET

Monika Pawlik-Niedźwiecka

PROMOTOR:
PROF. DR HAB. PAWEŁ MOSKAL
PROMOTOR POMOCNICZY: DR MICHAŁ SILARSKI

Kraków, 2023

Wydział Fizyki, Astronomii i Informatyki Stosowanej
Uniwersytet Jagielloński

Oświadczenie

Ja niżej podpisana Monika Pawlik-Niedźwiecka (nr indeksu: 1069039) doktorantka Wydziału Fizyki, Astronomii i Informatyki Stosowanej Uniwersytetu Jagiellońskiego oświadczam, że przedłożona przeze mnie rozprawa doktorska pt. "Determination of performance characteristics of the J-PET tomograph" jest oryginalna i przedstawia wyniki badań wykonanych przeze mnie osobiście, pod kierunkiem prof. dr hab. Pawła Moskala. Pracę napisałam samodzielnie.

Oświadczam, że moja rozprawa doktorska została opracowana zgodnie z Ustawą o prawie autorskim i prawach pokrewnych z dnia 4 lutego 1994 r. (Dziennik Ustaw 1994 nr 24 poz. 83 wraz z późniejszymi zmianami).

Jestem świadoma, że niezgodność niniejszego oświadczenia z prawdą ujawniona w dowolnym czasie, niezależnie od skutków prawnych wynikających z ww. ustawy, może spowodować unieważnienie stopnia nabytego na podstawie tej rozprawy.

Kraków, dnia

.....

Abstract

The aim of this work was to determine the performance characteristics of the Jagiellonian Positron Emission Tomography (J-PET) detector according to the worldwide National Electrical Manufacturers Association (NEMA) norm for PET scanners. NEMA norm defines parameters and procedures of their measurements such as spatial resolution, sensitivity, scatter fraction, count losses, randoms measurement and corrections for count losses and randoms as well as image quality. These parameters allow to compare PET scanners between different manufacturers.

J-PET scanner was built out of three layers of axially arranged organic scintillators which forms a cylindrical chamber and it was optimized for detection of back-to-back gamma quanta from electron-positron annihilations. These gamma quanta interact with scintillator material via Compton scattering. Light produced in this way in the scintillator is detected by two photomultipliers placed at opposite ends of each scintillator strip.

Measurements described in this thesis were performed according to the recommendations included in the NEMA norm and the gathered data was analyzed using the J-PET Framework, a dedicated processing algorithms written in object-oriented C++ language with BOOST and ROOT libraries included.

Measurements of the J-PET detector sensitivity were conducted with PET Sensitivity Phantom for two positions specified by the NEMA norm. The obtained sensitivity value was equal to $0.130 \pm 0.014 \frac{\text{cps}}{\text{kBq}}$ and $0.0789 \pm 0.0061 \frac{\text{cps}}{\text{kBq}}$ for 0 and 10 cm radial offset, respectively. Low sensitivity of the J-PET detector comes from the sparse detector geometry and can be improved in the future.

Spatial resolution of the J-PET detector was estimated based on results of measurements performed with point source placed inside the detector in six positions specified by the NEMA norm. Data was reconstructed with Filtered Back-Projection algorithm with cutoff value equal to 3.0 and Ridgelet filter. Tangential spatial resolution for the J-PET detector was equal to 0.635 ± 0.092 cm, 0.715 ± 0.092 cm and 0.630 ± 0.092 cm for position 1, 10 and 20 cm from the detector center, respectively. Radial spatial resolution for the same positions was equal to 0.280 ± 0.092 cm, 0.500 ± 0.092 cm and 0.445 ± 0.092 cm, respectively, and the axial spatial resolution was equal to 3.850 ± 0.028 cm, 3.667 ± 0.048 cm and 3.788 ± 0.053 cm. Tangential and radial spatial resolution values of the J-PET detector are of the same order as for commercial PET devices. Axial spatial resolution will be improved in the future by application of the wavelength shifters.

Scatter fraction for the J-PET detector was estimated based on results obtained from measurements with PET Scatter Phantom. Collected data was analyzed with post-processing algorithm with Single Slice Rebinning method. Obtained value of scattered fraction on the level of 35.41 ± 0.19 [%] is comparable to the commercial PET devices.

Streszczenie

Głównym celem prezentowanej pracy było wyznaczenie charakterystyk tomografu J-PET w oparciu o ogólnoświatową normę opracowaną przez National Electrical Manufacturers Association (NEMA). Norma ta definiuje parametry takie jak rozdzielczość przestrzenna, czułość detektora, frakcja rozproszeniowa, straty zliczeń, pomiar koincydencji losowych, korekcje na straty zliczeń i koincydencje losowe, a także jakość obrazu oraz standaryzuje procedury ich szacowania. Pozwala to na porównanie skanerów PET pomiędzy różnymi producentami.

Skaner J-PET został zbudowany z trzech warstw plastikowych scyntylatorów ułożonych osiowo i tworzących cylindryczną komorę. Działanie skanera zostało zoptymalizowane pod kątem detekcji kwantów gamma pochodzących z anihilacji elektron-pozyton. Kwanty te oddziałują z materiałem scyntylatora poprzez efekt Comptona. Produkowane w ten sposób światło rejestrowane jest poprzez dwa fotopowielacze umieszczone na przeciwnych końcach każdego scyntylatora.

Badania zostały przeprowadzone w oparciu o opis pomiarów zawarty w normie NEMA i opracowane przy wykorzystaniu dedykowanego oprogramowania J-PET Framework, które zostało napisane w języku C++ i wykorzystuje biblioteki BOOST i ROOT.

Pomiary czułości detektora J-PET zostały wykonane przy użyciu dedykowanego fantomu czułości w dwóch pozycjach określonych przez normę NEMA. Otrzymane wyniki są równe $0.130 \pm 0.014 \frac{\text{cps}}{\text{kBq}}$ oraz $0.0789 \pm 0.0061 \frac{\text{cps}}{\text{kBq}}$ dla przesunięcia radialnego wynoszącego odpowiednio 0 i 10 cm. Niska czułość detektora J-PET wynika z "rzadkiej" geometrii detektora i może być poprawiona w przyszłości.

Rozdzielczość przestrzenna detektora J-PET została określona w oparciu o wyniki pomiarów przeprowadzonych z wykorzystaniem punktowego źródła, które zostało umieszczone w sześciu pozycjach wewnątrz detektora wskazanych przez normę NEMA. Zebrane dane zostały zrekonstruowane przy użyciu algorytmu projekcji wstecznej z cięciem równym 3.0 oraz przy użyciu filtra Ridgelet. Transwersalna rozdzielczość przestrzenna detektora J-PET jest równa 0.635 ± 0.092 cm, 0.715 ± 0.092 cm oraz 0.630 ± 0.092 cm dla pozycji odległych odpowiednio o 1, 10 oraz 20 cm od środka detektora. Radialna rozdzielczość przestrzenna, określona dla tych samych pozycji, jest odpowiednio równa 0.280 ± 0.092 cm, 0.500 ± 0.092 cm i 0.445 ± 0.092 cm, podczas, gdy osiowa rozdzielczość przestrzenna jest równa 3.850 ± 0.028 cm, 3.667 ± 0.048 cm oraz 3.788 ± 0.053 cm. Wartość transwersalnej i radialnej rozdzielczości przestrzennej detektora J-PET jest tego samego rzędu co rozdzielczość przestrzenna komercyjnych skanerów PET. Osiowa rozdzielczość przestrzenna może zostać poprawiona w przyszłości poprzez wykorzystanie przesuwników długości fali.

Frakcja rozproszeniowa detektora J-PET została określona na podstawie wyników otrzymanych podczas pomiarów z dedykowanym fantomem rozproszeniowym. Zebrane dane zostały przeanalizowane przy użyciu metody Single Slice Rebinning. Otrzymana

wartość frakcji rozproszeniowej, równa 35.41 ± 0.19 [%], jest porównywalna z komercyjnymi urządzeniami PET.

Acknowledgements

First and foremost, I would like to express my deepest gratitude to prof. dr hab. Paweł Moskal and dr Michał Silarski without whom this thesis would not exist. I would like to thank my supervisor for the opportunity to be a part of the J-PET project and for all the outstanding guidance, support and feedback. I would like to thank my co-supervisor for unlimited support and unconditional guidance during writing this thesis.

I want to also thank my Colleagues from the J-PET collaboration: dr Aleksander Gajos, dr Kamil Dulski, dr inż. Wojciech Krzemień, mgr Kamil Rakoczy and Krzysztof Kacprzak for continuous support with analysis in the J-PET Framework, dr Sushil Sharma for his help with energy calibration procedure, mgr Szymon Parzych for unwavering support with the SSRB algorithm, dr Grzegorz Korcyl for his assistance during data gathering and dr Eryk Czerwiński for his patience during data taking and saving on the J-PET servers.

I am very grateful to the Świerk Computing Center in Warsaw for providing computational resources to process and analysis of the experimental data and for providing of enormous disk space.

I want to also give thanks to the current and former members of the J-PET group: dr Dominika Alfs, dr Magdalena Skurzok, dr Oleksandr Rundel, dr Juhi Raj, dr Muhsin Mohammed, dr Ewelina Kubicz, dr Daria Kisielewska, dr Paweł Kowalski, dr Aleksander Khreptak, dr Łukasz Kapłon, dr Neha Gupta-Sharma, dr Meysam Dadgar, dr Tomasz Bednarski, dr Marek Gorgol, mgr Faranak Tayefi, mgr Neha Chug, dr Kacper Topolnicki, mgr Shivani, mgr Nikodem Krawczyk, Konrad Wysogład for the great work atmosphere, good words and official and unofficial meetings. I am grateful to have the pleasure of working with you.

A lot of thanks to dr Kamila Zelga, dr Natalia Gorczowska, dr Magdalena Garbacz, dr inż. Jakub Baran, mgr Barbara Bednarska, Anna Kotowicz for the coffee, gossips and believing in me.

Dziękuję serdecznie Dyrekcji i Gronu Pedagogicznemu Szkoły Podstawowej nr 27 im. Marii Konopnickiej w Krakowie za okazywaną życzliwość i wsparcie, które otrzymałam w ostatnich miesiącach pisania pracy. Dziękuję za każdą rozmowę i każde dobre słowo.

Dziękuję mojemu mężowi, dr Szymonowi Niedźwieckiemu, za miłość, cierpliwość i towarzyszenie mi podczas każdego etapu tworzenia tej pracy. Bez Twojego wsparcia nie byłabym tu, gdzie jestem. Dziękuję mojemu synowi, Filipowi, za każdy uśmiech, przytulenie, nieskończoną miłość i cierpliwość do zawsze zapracowanej mamy. Ogromnie dziękuję także moim rodzicom, babci, bratu oraz teściom za nieustanne wspieranie mnie w tym co robię i nieustanną wiarę we mnie.

Na koniec chciałabym wyrazić podziękowanie moim wspaniałym nauczycielkom, Pani Małgorzacie Kaczor oraz Pani Edycie Górz, za pokazanie mi piękna fizyki i rozbudzenie mojej miłości do tej dziedziny nauki.

Contents

1	Introduction	15
2	General overview of Positron Emission Tomography	21
2.1	β^+ decay and interaction of 511 keV photons with matter	21
2.2	Detection of the 511 keV photons	25
2.2.1	Scintillators	26
2.2.2	Photodetectors	31
2.3	Detector and scanner design	32
2.4	Coincidence detection and types of events	35
2.5	Time-of-flight method	37
2.6	Radiopharmaceuticals	38
2.7	New trends in PET technology	39
2.8	Total-body PET (EXPLORER)	41
3	NEMA norms	43
3.1	Spatial resolution	43
3.2	Scatter fraction, count losses and random event rate measurement	45
3.3	Sensitivity	49
4	J-PET scanner	53
4.1	General concept of the J-PET detector	54
4.2	J-PET design	55
4.3	Data acquisition system	57
4.4	J-PET Framework	58
5	Measurements performed with the J-PET scanner	61
5.1	Radioactive sources	61
5.2	Measurements with the PET Scatter Phantom	64
5.3	Point-spread function measurements (with point-like source)	66
5.4	Measurements using the PET Sensitivity Phantom	67

6	Data preselection and detector calibration procedures	69
6.1	Time and velocity calibration	69
6.2	Data selection criteria	71
6.3	Energy calibration	78
7	NEMA characteristics studies	89
7.1	Sensitivity	89
7.2	Spatial resolution	96
7.3	Scatter fraction	109
8	Summary and results discussion	117
8.1	Sensitivity	117
8.2	Spatial resolution	118
8.3	Scatter fraction	120
9	Prospects for development of the J-PET tomograph	123
10	Conclusions	127
	List of Abbreviations	132
	Bibliography	133

Chapter 1

Introduction

The main aim of this thesis is to elaborate a performance characteristics of the first full scale prototype of Positron Emission Tomography scanner based on plastic scintillators. Plastic scintillators were proposed for the construction of PET scanner to make the diagnostics cost effective and world-wide accessible [1–7]. PET is the most advanced diagnostics method enabling detection of cancer at its early stage of development [8].

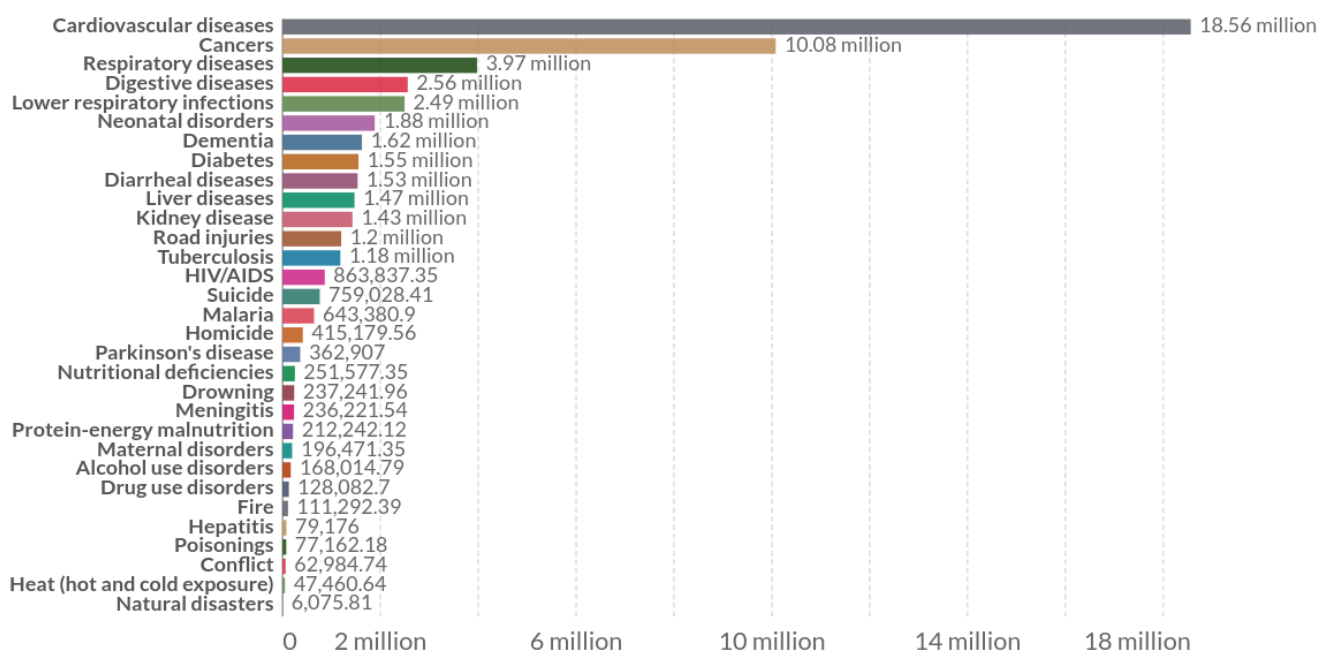


Figure 1.1: A worldwide number of deaths by cause in 2019. Cancer is one of the main causes of death. Data provided by Our World in Data [9].

Cancer, in generic term, is a disease in which body's cells divide and grow uncontrollably and may affect healthy tissues and, moreover, may spread over the patient's body.

According to data provided by World Health Organization (WHO), cancer is the second biggest cause of death just after cardiovascular diseases (see Fig. 1.1) and the number of cases is growing from year to year [10].

Cancer Research UK have reported 17 million of new cancer cases in 2018 and 9.6 million deaths caused by cancer. Almost 33% of cancer cases were linked to exposure to tobacco smoke and this number will grow in future due to the growing number of adults smoking cigarettes (more than 1 billion nowadays). On the other hand, risk factors are similar all over the world and contain also alcohol abuse, low physical activity, unhealthy diet and overweight. Different risk factors prevalence varies between different countries and become a serious problem in low- and middle-income countries [11]. Cancer diseases prevention and access to diagnostics and treatment become an increasingly important issues. These methods are not easily accessible in low-income countries and this fact is the main reason for searching of cheap diagnostic method. Currently, positron emission tomography (PET) is the main early detection method and can show up abnormalities earlier in comparison to Computed Tomography (CT) or Magnetic Resonance Imaging (MRI) examinations [12].

PET is a painless imaging procedure enabling detection of cancerous tumor cells and allowing for receiving information as well as for evaluation of metabolic and biochemical functions of organs and tissues in real time [8, 13]. PET uses radioactive tracer, called radiopharmaceutical, to identify abnormalities in patient's body by measurement of glucose consumption rate. Cancer cells, especially in malignant tumors, show up a much higher radiotracer consumption level in comparison to healthy tissue [14]. PET and PET/CT scans can be performed in order to cancer detection or to check how cancer spread in patient's body and as well as to evaluate treatment effectiveness. PET procedure can be also used to evaluation of nervous system disorders such as seizures, memory disorders, Parkinson's and Alzheimer's disease and even to check heart functions, effects of a heart attack myocardial infarction, heart blood flow or to check abnormalities in heart muscle building [8, 15, 16].

PET scan is a relatively easy examination procedure. Patient, after radiotracer injection, should sit quietly for 45-60 minutes, sometimes 90 minutes, depend on organ of interest due to time needed for radiotracer to reach to a given part of body. Afterwards, PET scan is performed for approximately 30-60 minutes. Whole procedure is not painful and the amount of injected radioactivity is small, so patient exposure for radiation is low [17, 18].

The average activity of most often used radiopharmaceutical (^{18}F FDG) administrated to patient is equal to 370 MBq and this number corresponds to effective dose below 10 mSv per scan [19]. Average annual dose from natural background radiation per person depends on the place of residence and in the U.S. is equal to 6.2 mSv while average dose in Europe

is equal to 3.2 mSv and varies from 1.48 mSv in the Netherlands to 5.83 mSv in the Czech Republic. Average dose in Poland is equal to 2.77 mSv [20,21]. Exposure during the PET scan is equal to natural radiation dose received by person in one to three years.

The average cost of PET scan in the U.S. is equal to 5750 \$, but prices can vary from 1250 \$ to 8225 \$ around the country [22]. Final price depends mainly on four factors such as health insurance, place of residence, facility settings (hospital or outpatient center) and type of scan (whole body scan, brain scan, etc.). Average commercial price of the PET examination in Poland in 2016 was equal to 4320 PLN, while currently whole body scan can reach the price equal to 11000 PLN (for PET/MRI procedure) [23, 24].

The price of PET device is very often an obstacle for hospitals, especially in low-income countries. The price of PET/CT scanner can vary from 1.7 million dollars to 2.5 million dollars (based on prices in 2014) [25]. For PET/MRI devices typical prices vary from 1 million dollars to even 3 million dollars [26]. PET examination is also not a cheap procedure, but possibilities and benefits outweigh the cost and the very important issue is equal and easy access to this procedure for all people all over the world.

The Jagiellonian PET (J-PET) group is working on the cost-effective total body PET device. The whole body J-PET scanner was constructed and made operational thanks to work of international and multidisciplinary team.

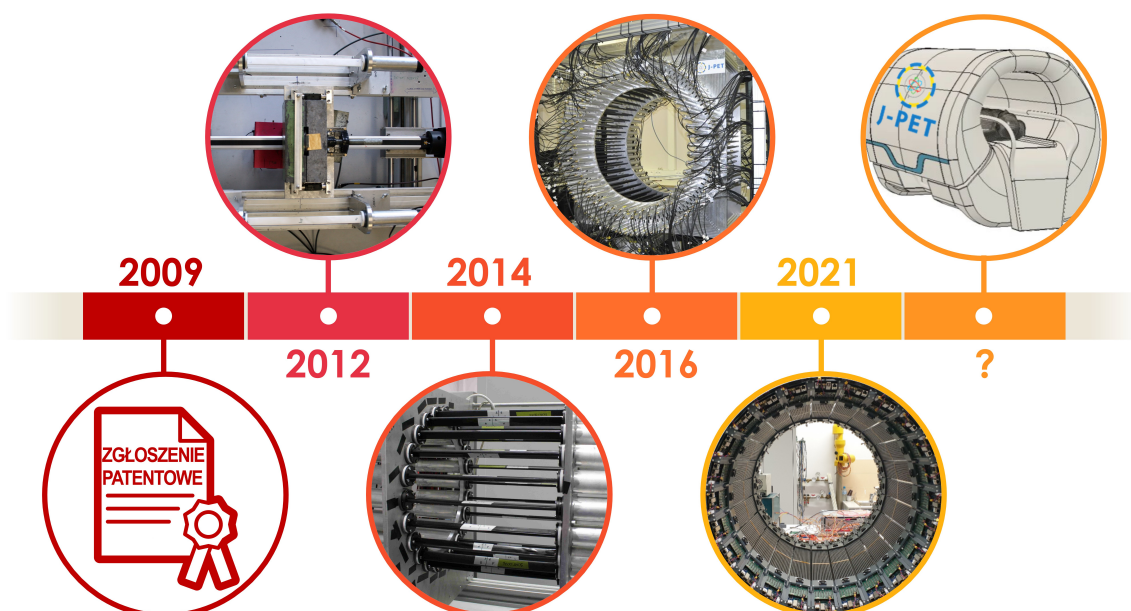


Figure 1.2: Timeline of the work on the prototype of the J-PET scanner. Courtesy of the J-PET group and Bartosz Leszczyński.

The story of the whole body J-PET detector has started from prof. Paweł Moskal idea and the first patent application in 2009 [27, 28]. First experimental setup was built out

of only two plastic scintillator strips. Light signals from scintillators was read by two photomultipliers placed at two opposite ends of each strip [1, 29–31]. This easy setup has allowed to gain experience in photomultipliers calibration, data management, image reconstruction as well as in trigger-less data acquisition systems [32–41]. Double-strip setup was the proof-of-concept for the 24-strip prototype built in 2014 [42]. In 2016, the whole body J-PET detector was built in form of cylindrical chamber formed by three concentric layers of plastic scintillators strips as one can see in Fig. 1.3 [43, 44]. Axial field-of-view (AFOV) of this scanner is equal to 50 cm and even on the level of prototype is at least 2 times bigger in comparison to commercial PET devices [3].

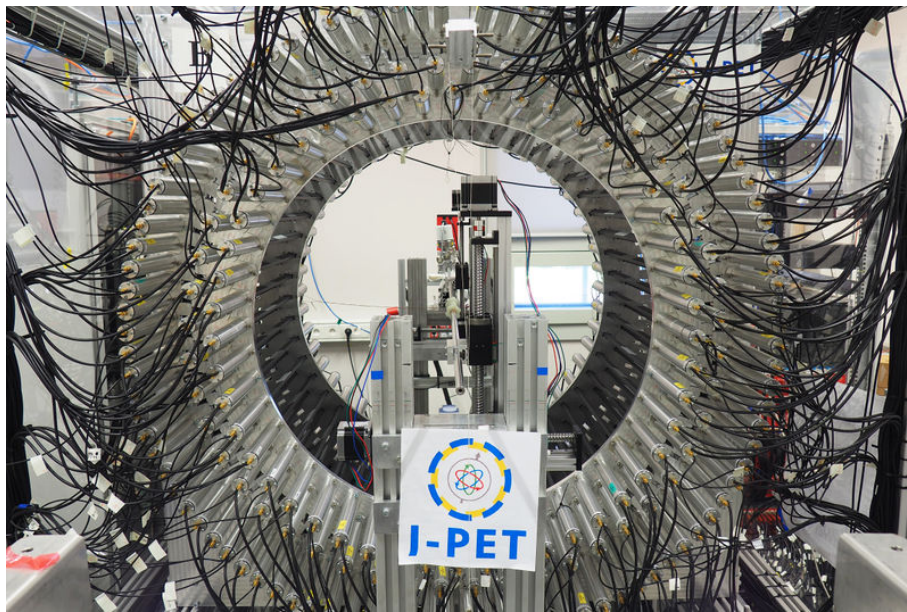


Figure 1.3: Photography of the whole body J-PET detector. Courtesy of the J-PET group.

Plastic scintillators used in the J-PET detector are cheaper alternative to inorganic scintillators used in commercial PET scanners. Cost of the same volume of scintillation material differs about 80 times [13]. Extending the axial field-of-view in commercial PET scanners requires significantly larger number of inorganic scintillators and photodetectors while in the J-PET detector only the length of plastic scintillators has to be increased [45]. The construction of the whole body J-PET scanner opens perspectives for the cost-effective total body PET device which can be combined with MRI and CT instruments [3].

The aim of this work is to estimate the performance characteristics of the J-PET detector according to the worldwide National Electrical Manufacturers Association norm for PET scanners. The standard NEMA-NU-2-2012 defines PET characteristics such

as detector sensitivity to incoming radiation expressed as true coincidence events rate, sensitivity to scattered radiation and spatial resolution.

Basics of the PET tomography are explained in details in the 2-nd Chapter. In the 3-rd Chapter all important information about NEMA standard are included. Each performance characteristic procedure is thoroughly explained. Both chapters are written based on the literature studies. In Chapter 4, a detailed description of the J-PET detector is presented. Depiction of its components, construction details, principle of operation, overview of the software architecture and analysis framework is included in this chapter. Chapter 5 is devoted to measurements performed with the J-PET detector according to the NEMA-NU-2-2012 norm, while Chapter 6 contains detailed explanation of detector calibration procedures and preselection condition applied to data collected during measurements. Chapter 7 contains details about analysis performed according to the NEMA standard to obtain J-PET detector characteristics. In Chapter 8, a detailed discussion of obtained results is included. Results are compared with performance characteristics of commercial PET scanners. Perspectives of development of the J-PET detector into total body PET scanner are described in Chapter 9. This work ends with conclusions included in Chapter 10.

Author contribution:

The author has performed the following activities which allowed completion of this thesis:

- participation in the data monitoring and data taking during experiments,
- preparation and participation in measurements needed for time, velocity and energy calibrations,
- preparation of experimental setup and measurements with the PET Scatter Phantom, the PET Sensitivity Phantom and point-like source,
- preparation of data preselection and energy calibration J-PET Framework modules,
- implementation of energy calibration of the J-PET detector,
- development of data preselection procedures,
- adaptation of the Filtered Back-Projection and Single Slice Rebinning algorithms to the experimental data,
- preparation of post-processing algorithms,
- preparation of a dedicated methods and modules in J-PET Framework for estimation of measurement duration,
- analysis of the preselected data according to the NEMA norm,
- reconstruction of images with FBP algorithm,
- estimation of sensitivity, spatial resolution and scatter fraction.

Chapter 2

General overview of Positron Emission Tomography

Positron Emission Tomography is one of the major tools of nuclear medicine for imaging of physiology of human body [46, 47]. This non-invasive method allows to create a tomographic image based on reconstruction of a spatial distribution of positron-emitting radionuclides. Positron emitted by radionuclide annihilates with an electron and then as a result pair of back-to-back 511 keV photons is produced. These photons are subsequently detected by a pair of detectors located opposite to each other in the tomograph ring. The most likely point of annihilation along line identified by this detector pair (called line-of-response, LOR) can be determined using the time-of-flight (TOF) method which is based on the difference of registration times of the two photons (Δt). The three dimensional (3D) image of annihilation points is determined after the tomographic scan using sophisticated mathematical reconstruction algorithms.

PET is widely used especially in oncology (about 99% of all examinations in Poland in 2015) as well as in cardiology and neurology [23]. Positron Emission Tomography allows for detection of cancer tumors, treatment planning and controlling of the treatment effectiveness. Moreover, PET enables studies of mental diseases and viability and perfusion of myocardium [48].

2.1 β^+ decay and interaction of 511 keV photons with matter

Proton-rich radionuclides decay by the β^+ emission (also known as *positron emission*). These unstable nuclei achieve stability by proton to neutron conversion in the process:



Radionuclide transition energy (E), due to energy conservation law, has to be equal at least 1.022 MeV (mass of electron and positron) to decay by β^+ emission. The energy beyond 1.022 MeV is shared as a kinetic energy between positron and neutrino which are ejected from the nucleus and the nucleus itself [49]. Positron loses kinetic energy due to collisions with atoms (e.g. in body tissues) until it comes to rest and being at rest it annihilates with an electron forming two 511 keV annihilation photons (see Fig. 2.1) [50]. Photons, due to momentum conservation, are emitted almost "back-to-back" (anti-parallel emissions) [51].

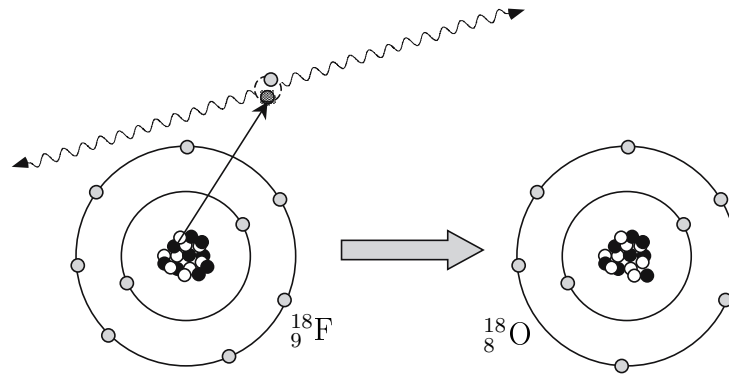


Figure 2.1: Positron, ejected from the nucleus, loses kinetic energy by interaction with atoms in the surrounding matter until it comes to rest and annihilates with electron. Two 511 keV photons are emitted in almost opposite direction. Figure adapted from [52].

Proton-rich radionuclides can also undergo transformation by electron capture (EC) process. An orbital electron, from the nearest shell, combines with proton producing neutron when energy is not sufficient for the β^+ decay ($E < 1.022$ MeV) [49, 51].



Transition energy remaining after neutrino emission can be emitted by the nucleus as X-rays or gamma quanta radiation.

High-energy photons can transfer energy to matter through three main processes:

- photoelectric effect - in this interaction mechanism photons transfer all of their energy usually to an inner shell electrons of an atom (see Fig. 2.2) causing ejection of the electron. Kinetic energy of the ejected electron (*photoelectron*) is equal to $E_\gamma - E_B$, where E_γ is the energy of incident photon while E_B is the electron binding energy in the shell. A characteristic X-ray radiation is produced when loosely

bound electron from higher energy level drops down to occupy vacancy after rejected electron. The probability of the photoelectric effect, given by Z^5/E_γ^3 , strongly depends on the atomic number of absorber (Z) and decreases with increasing energy of incoming E_γ . In human tissues this effect dominates at energies below 100 keV and for 511 keV gamma it has much lower probability than Compton scattering. Probability of photoelectric effect for 511 keV quanta is equal to 40% for BGO crystals while for LSO is equal to 32% [49, 51–56].

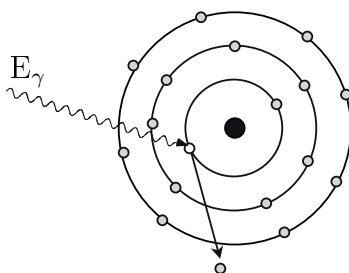


Figure 2.2: Photoelectric effect. A photon interacts and transfer all of its energy to an inner shell electron. Subsequently, electron is ejected from the atom. Figure adapted from [52].

- Compton scattering - in this predominant interaction in case of the 511 keV gamma quanta in the human body the incoming photon scatters on loosely bound electron at an outer shell (known as *valence* or *recoil* electron) of an atom transferring a part of energy to this electron and ejecting it (see Fig. 2.3). Binding energy of electron is much smaller in comparison to energy of photon and can be neglected. Ejected electron is absorbed in the within few millimeters from the interaction point, while the scattered photon can leave the medium without interaction or can undergo a photoelectric process or another Compton scattering. Due to momentum and energy conservation a relationship between energy of incoming photon (E_γ), energy of the scattered gamma (E'_γ) and scattering angle (θ_c) is connected by the following equation:

$$E'_\gamma = \frac{m_e c^2}{\frac{m_e c^2}{E_\gamma} + 1 - \cos\theta_c} \quad (2.3)$$

where m_e is electron mass and c is speed of light. Term $m_e c^2$ is equal to 511 keV. For 511 keV photons, used in PET diagnostics, this equation reduces to:

$$E'_\gamma = \frac{511 \text{ keV}}{2 - \cos\theta_c} \quad (2.4)$$

Maximum amount of energy is transferred to electron when θ_c is equal to 180° . Probability of Compton effect increases with the atomic number (Z) of the medium.

In case of body tissues, this effect dominates in energy range between 100 keV and 2 MeV [49, 51–55].

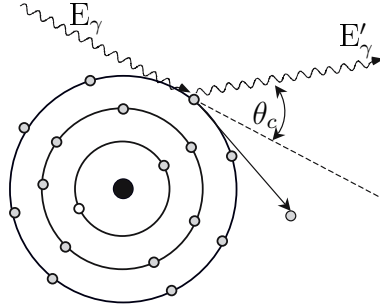


Figure 2.3: Compton scattering. Photon scatters on *valence* electron transferring a part of energy and ejecting it. Scattered photon can leave the medium or can undergo a photoelectric process or another Compton scattering. Figure adapted from [52].

- pair production - this process occurs when energy of photon is greater than 1.022 MeV (the double of the energy equivalent of the rest mass of an electron). Photon, passing in the nucleus region, can spontaneously form in the nucleus Coulomb field positron and electron as one can see in Fig. 2.4. Probability of pair production (above 1.022 MeV threshold) increases with photon energy and at 10 MeV is equal to about 60% of all possible processes. Energy left after positron and electron production is shared between these two particles as a kinetic energy. Positron has slightly bigger energy than electron due to positron acceleration and electron deceleration caused by the character of interaction of incoming particle and nucleus. When positron comes to rest, it annihilates with electron and two 511 keV annihilation photons are produced as was described earlier [49, 51–55].

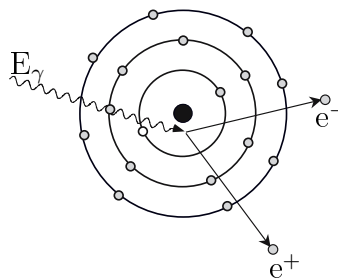


Figure 2.4: Pair production. Photon, passing in the nucleus region, can spontaneously form positron and electron. The energy is shared between the two particles as a kinetic energy. Figure adapted from [52].

The two major interaction types of 511 keV photons with matter are *photoelectric effect*

and *Compton scattering*. Due to this two effects it is possible to define linear attenuation coefficient (interaction probability per unit distance):

$$\mu \approx \mu_{Compton} + \mu_{photoelectric} \tag{2.5}$$

For the Positron Emission Tomography three media are of the most importance: body tissue, the detector material and materials used for collimation or shielding. A 511 keV annihilation photon can be detected only if it is ejected from the patient's body. The main interaction in the tissue is Compton scattering causing not only the signal attenuation but also the incorrect localization of annihilation event. Photons after Compton scattering can be rejected only if detectors have sufficiently good energy discrimination. On the other hand, detection of annihilation photons which passed through patient's body without interactions is the basic function of PET. Detection material should be enough dense to stop these photons. Moreover, for most of the applications the ratio between probabilities of Compton scattering and the photoelectric effect should be low for materials used to detect the gamma quanta. This provides clear identification of the signal events. On the other hand, multiple interactions in detector related to Compton effect cause that it is impossible to locate place of interaction of 511 keV photon with detection material [53]. The linear attenuation coefficients for different types of tissues and detection materials can be found separately for the two effects in Tab. 2.1.

Table 2.1: Values of linear attenuation coefficient for different materials. The half-value thickness is material thickness required to attenuate 50% of the incoming photons. Table adapted from [53].

Material	$\mu_{Compton}$ (cm^{-1})	$\mu_{photoelectric}$ (cm^{-1})	μ (cm^{-1})	Half-value thickness (cm)
Soft tissue	~0.096	~0.00002	~0.096	7.2
Bone	~0.169	~0.001	~0.17	4.1
Bismuth germanate	0.51	0.40	0.96	0.76
Lead	0.76	0.89	1.78	0.42
Tungsten	1.31	1.09	2.59	0.29

2.2 Detection of the 511 keV photons

One of the oldest methods of detection of gamma radiation is scintillation mechanism. Typical detector, used currently in most of the PET scanners, consist of scintillation

material and photon detector. 511 keV photons interact with medium of scintillator and deposit energy. After energy deposition scintillation material produces visible light which is detected by photon detectors and converted into an electric current.

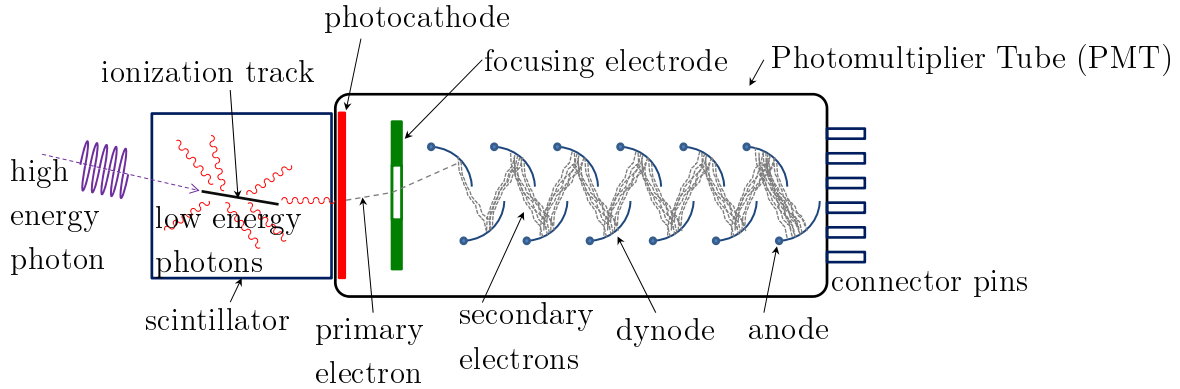


Figure 2.5: Schematic view of PET detector consisting of scintillator and photomultiplier tube. High-energy photons deposit energy in scintillator medium. Energy deposition results in light production which is detected by a photomultiplier and converted into an electrical current. Figure adapted from [57].

The most important properties of detectors used in the PET tomography are the high efficiency for 511 keV photons detection and energy resolution. To obtain good signal-to-noise ratio a lot of photon pairs have to be detected. Moreover, measurement of energy of incoming photons can be used for rejection of the 511 keV photons scattered in the patient body [53].

2.2.1 Scintillators

Scintillator is a type of transparent material which emits isotropically visible light after energy deposition by high energy photon. Amount of emitted light is proportional to deposited energy. There are four crucial features for application of scintillators in the PET tomography:

- stopping power - is a mean distance travelled by incoming photon inside the scintillator until it deposits all of its energy. Stopping power depends on the scintillator density and effective atomic number (Z_{eff}). For dense scintillators only a few centimeters are needed to effectively stop a large fraction of incoming high energy photons.
- energy resolution - determines the efficiency of rejection of photons which scattered through Compton effect in the patient's body before being detected and depend on

material light output as well as on intrinsic scintillator energy resolution. The intrinsic energy resolution is affected by non-uniform light production due to inhomogeneities in the material structure.

- light output - high light output results in well-defined pulse which improves timing and energy resolution.
- decay time - short decay time allows for individual processing of each pulse when the counting rate is high and for reduction of random coincidences in the PET system. Scintillators with short decay time can reduce dead time and are better choice in application of the time-of-flight method [49, 51–53, 55].

Scintillating materials used for detection of incoming radiation in nuclear medicine can be divided into two main categories: inorganic and organic scintillators. The most important difference between them is scintillation mechanism. Inorganic scintillators can be in the form of crystalline, ceramic, glass and gaseous. Organic scintillators can be produced in form of crystalline, plastic and liquid. In this thesis only crystal inorganic and plastic organic scintillators are discussed.

Inorganic scintillator crystals, most commonly used in PET, are an insulators with gap between valence and conduction bands. Ionizing radiation produces electron-hole pair while passing through the scintillator. Electron can jump to conduction band and become free to move around if the energy transferred to molecule by incident radiation is sufficiently high. The hole also becomes free. On the other hand, electron can be partially bound to the hole if the energy passed to the molecule is not high enough. However, usually the bounding is not strong and a small amount of additional energy transferred to the electron can shift it to the conduction band.

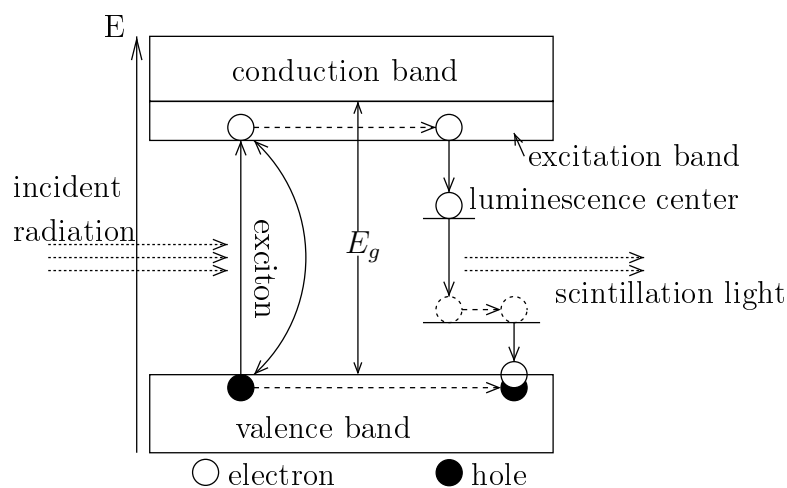


Figure 2.6: Schematic representation of the scintillation mechanism in inorganic scintillators. Figure adapted from [58].

Bound state of electron and hole is called *exciton* which travels in the scintillator until it gets trapped by an impurity or a defect in the crystal structure. Emission of light occurs when the defect constitutes a luminous center and electron falls to the lower level as one can see in Fig. 2.6. Additional state in the forbidden band can be also created by dopant added to the scintillator. In this case, scintillation light is emitted when electron falls into the lower luminescence level from dopant level where it was trapped [58].

Comparison between commonly used scintillators one can find in Tab. 2.2.

Table 2.2: Properties of commonly used scintillators in PET for gamma quanta with the energy of 511 keV. Table adapted from [53].

Scintillator	Density (g/cc)	Light output (photons per 511 keV)	Decay time (ns)	Index of refraction	Linear attenuation at 511 keV (cm^{-1})	Ratio between photoelectric and Compton
Sodium Iodide (NaI(Tl))	3.67	19400	230	1.85	0.34	0.22
Bismuth Germanate (BGO)	7.13	4200	300	2.15	0.96	0.78
Lutetium Oxyorthosilicate (LSO:Ce)	7.40	~13000	~47	1.82	0.88	0.52
Gadolinium Oxyorthosilicate (GSO:Ce)	6.71	~4600	~56	1.85	0.70	0.35

NaI(Tl) is widely used as a gamma camera and in SPECT systems, because it is easy to produce and has low production cost. *NaI(Tl)* has also high light output. On the other hand, it has the lowest density as well as the lowest stopping power in comparison to other presented crystals. It was used in earlier PET systems, but currently *BGO* and *LSO* occupy the scintillator market due to their better properties.

BGO, besides worst decay time and smaller light output, has excellent stopping power and therefore has high sensitivity for 511 keV photons detection. Energy resolution, due to light output, is typically equal to about 20%. Unfortunately, dead time limits count rate detected by PET system.

Cerium-doped *LSO* has short decay time, high light output and stopping power which is the ideal combination of advantages for PET purposes. In spite these properties, the overall energy resolution is worst than *NaI(Tl)* due to structure inhomogeneities. Moreover, *LSO* contains natural radioisotope ^{172}Lu which has half-life equal to 3.8×10^8 years and decays by emission of β^- rays. Energy of emitted photons is in the order

of 88-400 keV and is lower than 511 keV so low-energy application of *LSO* is limited but does not affect application in PET systems.

Cerium-doped *GSO* is also a good choice for PET system applications. In spite of lower light output and stopping power in comparison to *LSO*, it has better energy resolution, uniform light output and high temperature stability. On the other hand, *GSO* crystals are fragile and need extra care [49, 52, 55, 58]

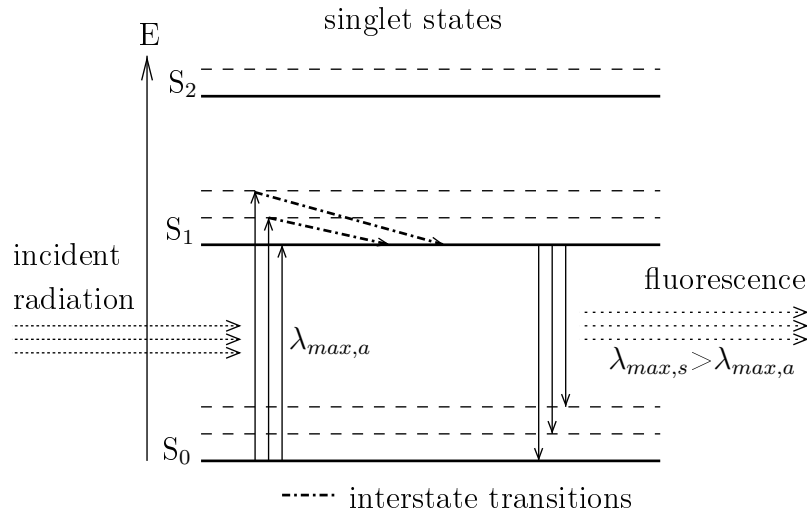


Figure 2.7: Scintillation mechanism in organic scintillators with process of light emission known as fluorescence. Subscripts *a* and *s* refer to absorption and scintillation processes, respectively. Difference between emission and absorption wavelength results from Stoke's shift. Figure adapted from [58].

Scintillation mechanism in organic scintillators is based on electron transition between different states. Electron is transitioned from ground level S_0 to one of the vibrational S_1 levels due to energy transfer from incident radiation to the atoms (see Fig. 2.7). Instability induced in the system forces electron to fast radiationless transition from the vibrational S_1 level to ground S_1 level. Subsequently, electron falls to one of the vibrational S_0 levels or S_0 ground level in time interval of the order of few nanosecond. The electron excess energy is emitted as photons from ultraviolet or visible part of electromagnetic spectrum in process known as fluorescence.

Another possible ways of generation of the scintillation light is the transition through vibrational levels of triplet T_1 (see Fig. 2.8). Electrons from S_1 ground level can go to one of the more stable T_1 levels, where they are trapped for some period of time, and then to the S_0 levels. Light is emitted in process known as phosphorescence with delay bigger than 100 ms for standard organic scintillator [58].

The most popular form of organic scintillators is plastic scintillator used in many applications. The basics of formation process are simple, but in practice production

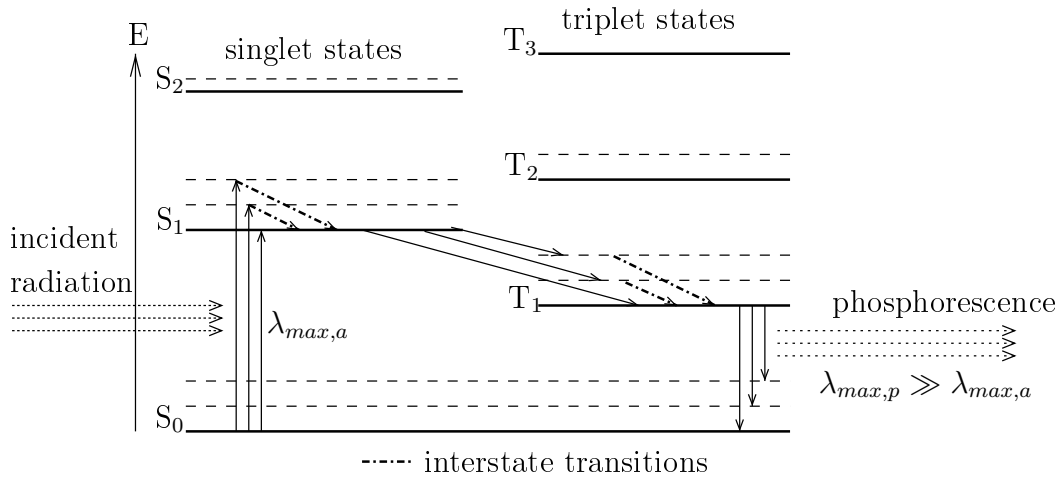


Figure 2.8: Scintillation mechanism in organic scintillators with process of light emission known as phosphorescence. Subscripts a refers to absorption while p to phosphorescence photons. The wavelength of phosphorescence emission is much larger than wavelength of absorption. Figure adapted from [58].

is an intensive and time consuming process. To produce plastic scintillator all components have to be highly purified. The base material is a liquid of one of the monomers such as polystyrene or polyvinyltoluene. In the next step, scintillation additives are mixed homogeneously with the base. Additives can be divided into primary fluor and secondary fluor (called as wavelength shifter). Light from base is absorbed by primary fluor and emitted through fluorescence to wavelength shifter to produce photons in visible range (see Fig. 2.9).

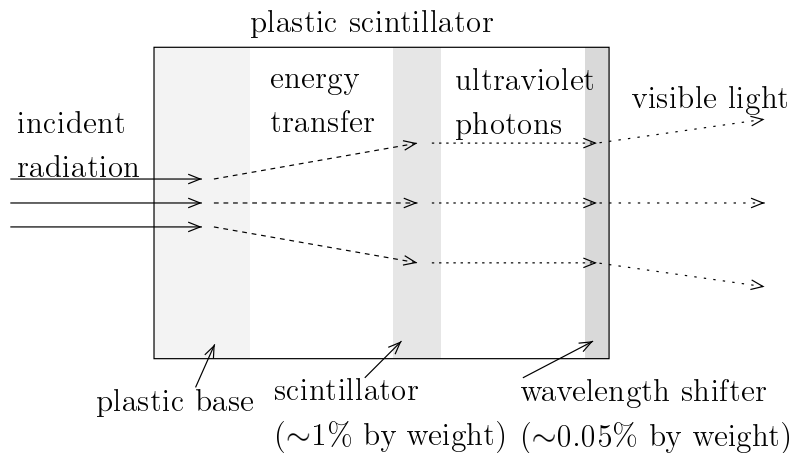


Figure 2.9: Plastic scintillator working mechanism. Figure adapted from [58].

The main advantages of plastic scintillators are chemical stability, high optical homogeneity and the ease of forming them in any desired shape. Physical properties vary

between different manufacturers and different models of scintillators. Comparison between two manufacturers for similar scintillators can be found in Tab. 2.3.

Table 2.3: Properties of plastic scintillators produced by Saint-Gobain Crystals and Eljen Technology. BC-404 and BC-420 are equivalent of the EJ-204 and EJ-230 scintillators, respectively. Data taken from [59, 60].

Scintillator	Light output (% Anthracene)	Decay time (ns)	Density (g/cm ³)	Light attenuation length (cm)
BC 404	68	1.8	1.032	140
BC 420	64	1.5	1.032	140
EJ 204	68	1.8	1.023	160
EJ 230	64	1.5	1.023	120

2.2.2 Photodetectors

Photomultiplier Tubes (PMT) are the most commonly used photodetectors in Positron Emission Tomography due to their properties such as stability, excellent signal-to-noise ratio and high gain (in the order of $10^6 - 10^7$) [49]. A single PMT is built out of a photocathode, a focusing electrode, dynodes and an anode, as one can see in Fig. 2.5.

An incoming photon hits the emissive material (photocathode) at the inner surface of the entrance window. Photons can easily eject electrons in the photoelectric effect. Electrons are emitted with probability in the range of 15%-25% depending on the photocathode quantum efficiency for a given wavelength. Each electron is accelerated by high potential difference to the positively charged electrode (dynode) and produces about 4 secondary electrons from dynode surface [53, 61]. Secondary electrons are also accelerated by potential difference to the next dynode and the multiplication process is repeated, such that a photoelectron avalanche is created. Each primary electron can be multiplied with a gain in the order of 10^6 at the last dynode (anode) [52, 53].

The efficiency of incident light energy conversion into electrons varies with light wavelength as was mentioned above. Quantum efficiency can be defined as a number of photoelectrons emitted from the photocathode divided by the total number of incident photons and usually is expressed in percents. Quantum efficiency depends on the radiant sensitivity and light wavelength, as one can see in Fig. 2.10, and can be expressed by the following relationship:

$$QE = \frac{h \cdot c}{\lambda \cdot e} = \frac{S \cdot 1240}{\lambda} \cdot 100[\%] \quad (2.6)$$

where: h - Planck's constant, c - speed of light in vacuum, e - electron charge, S - radiant sensitivity defined as photoelectric current divided by incident radiant power for a given wavelength (A/W), λ - incident light wavelength (nm) [62].

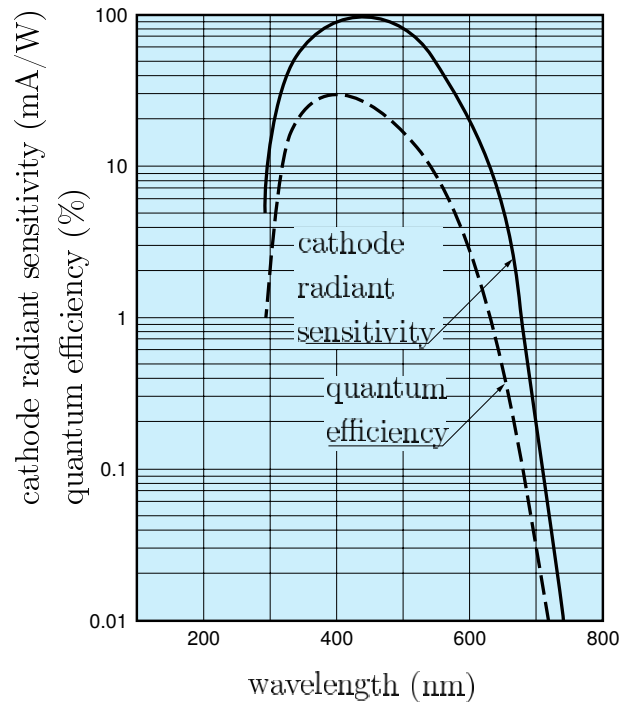


Figure 2.10: Example of photocathode spectral response. Figure adapted from [62].

Photomultipliers have typically 9 to 12 dynodes. Usually applied voltage is equal to about 1000 V.

2.3 Detector and scanner design

In early PET scanners each crystal was glued to individual photomultiplier tube. Single detectors were arranged in a one or more rings. The spatial resolution was limited by size of the crystal. Nowadays most of the used PET scanners are based on *block detectors* proposed in mid-1980s [55].

The block detector is built from scintillator block connected with four PMTs. Single crystal (typically $4 \times 4 \text{ cm}^2$ area and 3 cm thick) is segmented into array of 6×8 , 7×8 or 8×8 elements wrapped using reflective material as one can see in Fig. 2.11. To allow for light sharing between photomultipliers the cut depths vary between neighboring pixels. The deepest cuts are located at the scintillator block edge. Due to uneven cutting light from interaction of photon close to scintillator edge will be detected only by the closest photomultiplier while light from photon interaction in the middle of scintillator block will

be detected by all photomultipliers. Cuts provide an unique light distribution between photomultipliers (see Fig. 2.12) [49, 51, 53].

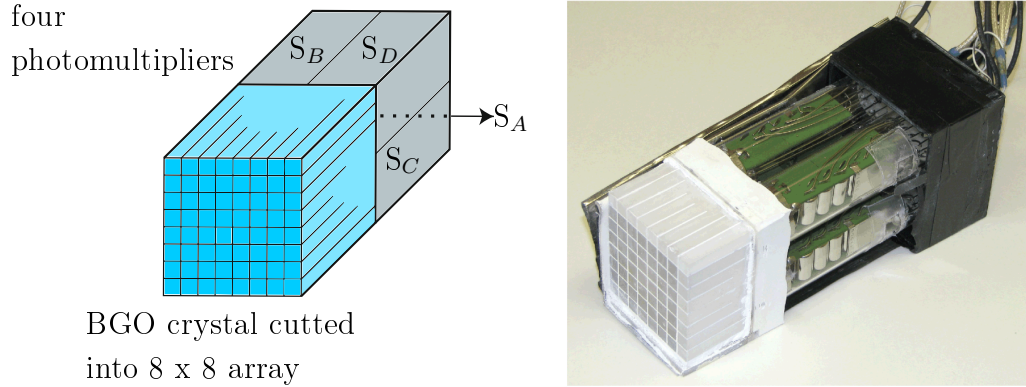


Figure 2.11: (left) Scheme of typical block detector. Figure adapted from [49]. (right) Block detector used in the Siemens/CTI ECAT 953B. Photography adapted from [63].

An X and Y coordinate of place of interaction of photon in the scintillator can be calculated from a simple equations:

$$X = \frac{S_A + S_B - S_C - S_D}{S_A + S_B + S_C + S_D} \quad (2.7)$$

and

$$Y = \frac{S_A + S_C - S_B - S_D}{S_A + S_B + S_C + S_D} \quad (2.8)$$

where S_A , S_B , S_C and S_D is signal strength from a corresponding photomultiplier. An exemplary two dimensional flood-field image obtained as a result of 8 x 8 elements block detector uniformly irradiated with annihilation photons one can see in Fig. 2.13 [51, 53]. The detector response for uniform irradiation is linear. In case of 8 x 8 elements block detector each photomultiplier can read 16 elements. This approach is cost-effective due to high price of PMTs.

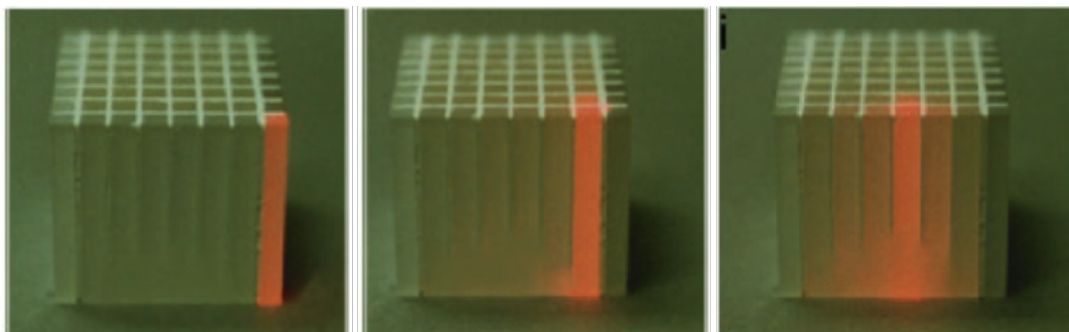


Figure 2.12: Light distribution in a block detector. Photography adapted from [55].

To cover good solid angle thousands of block detector elements have to be used. Moreover, size of a single element determines spatial resolution of the PET scanner [53].

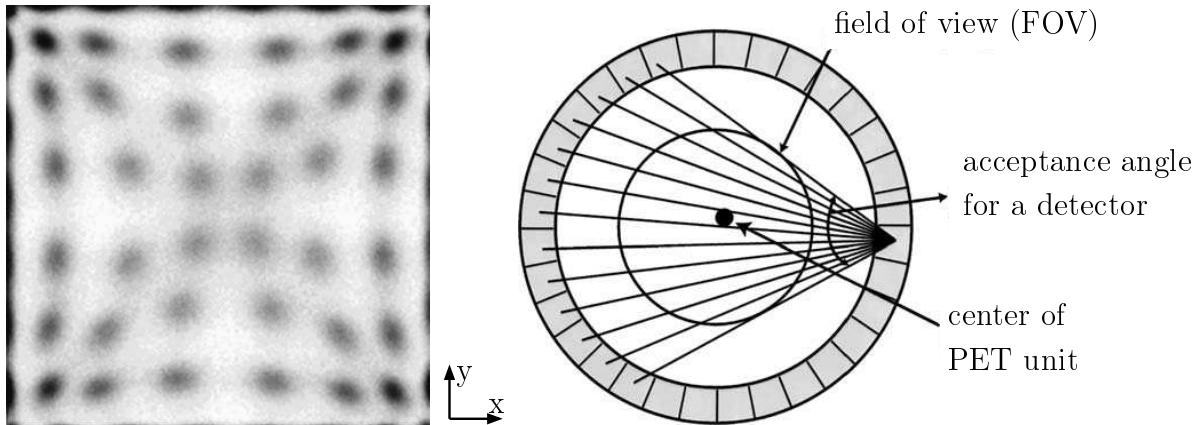


Figure 2.13: (left) Flood histogram of signals of the gamma quanta registered by the block detector. The x and y coordinates are calculated according to Eqs. 2.7 and 2.8. Figure adapted from [53]. (right) The transverse field of view. Figure adapted from [49].

Conventional PET scanner is built out from large number of block detectors arranged in a ring (see Fig. 2.14). Typically ring diameter is equal to 80-90 cm, while the scanner bore is 55-60 cm [51]. Transverse field of view is determined by detector acceptance angle (see Fig. 2.13). Axial field of view is usually equal to 20 cm, so during scan in a single bed position 85-90% of patient body is outside field of view (FOV) and not examined. Due to the isotropic annihilation radiation emission only 3-5% of true coincidence events can be registered [64].

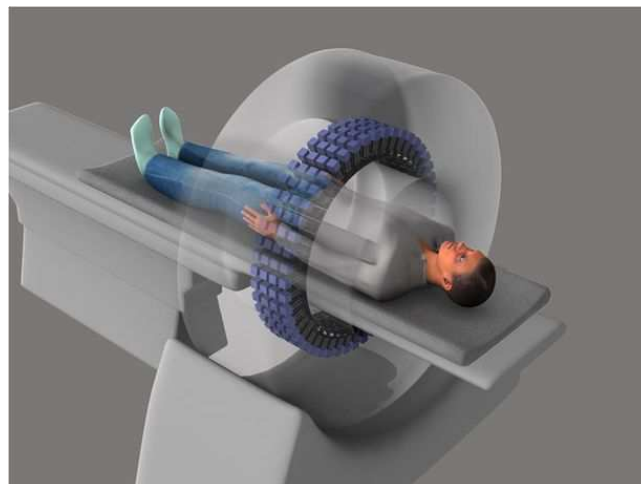


Figure 2.14: Conventional PET scanner. Four rings of block detectors are visible. Figure adapted from [64].

2.4 Coincidence detection and types of events

PET scanner detects two back-to-back photons originating from an annihilation of electron and positron in coincidence mode with predefined time window (e.g. 5.5 ns) as one can see in Fig. 2.15. Line connecting the two detectors which registered gamma quanta (*LOR*, *line-of-response*) must cross FOV [49]. Photons energy deposition in the specific energy window around photopeak (e.g. 435 - 600 keV) is used in the event selection as well [53,65].

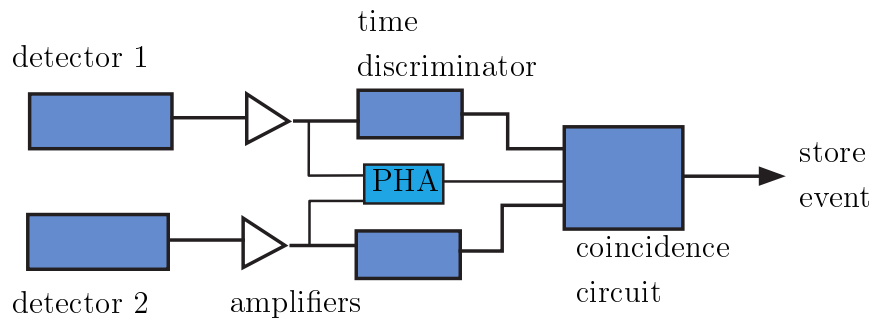


Figure 2.15: Scheme of a time and energy discriminators for PET systems. Abbreviation PHA means pulse-height analyzer. Signal height is related to energy deposited by photon. Figure adapted from [66].

Coincidence events include four different types of events: true, random, scattered and multiple. In true coincidence annihilation photons escape the patient's body without interactions and are recorded by pair of two opposite detectors. The scattered coincidences consist of one or both of the photons interacting with the body and the place of annihilation is misreconstructed due to wrongly designated LOR. In random coincidence two photons originating from two different annihilations are detected as one can see in Fig. 2.16. In multiple coincidence more than two photons are recorded [67].

Single photon detection is the major part of registered events (even up to 90% or more). Second photon coming from the same annihilation may not interact with detector or may not deposit sufficient energy (belonging to energy window). These events are not accepted but they can have contribution in random and multiple coincidences. Random and scattered coincidences produce unwanted background and reduce image contrast [53]. The ratio of random to true coincidences decreases with time window shortening.

Scattered events with energy deposited in detector significantly different from energy deposition for 511 keV photons can be rejected by energy discrimination.

Different corrections are applied to data from PET scan to improve image quality. One of these corrections will be discussed in Sec. 2.5.

The last stage of coincidence detection is the data storage in a form of sinogram. In the first step of data acquisition, each 511 keV photons detection is stored in a 2-D

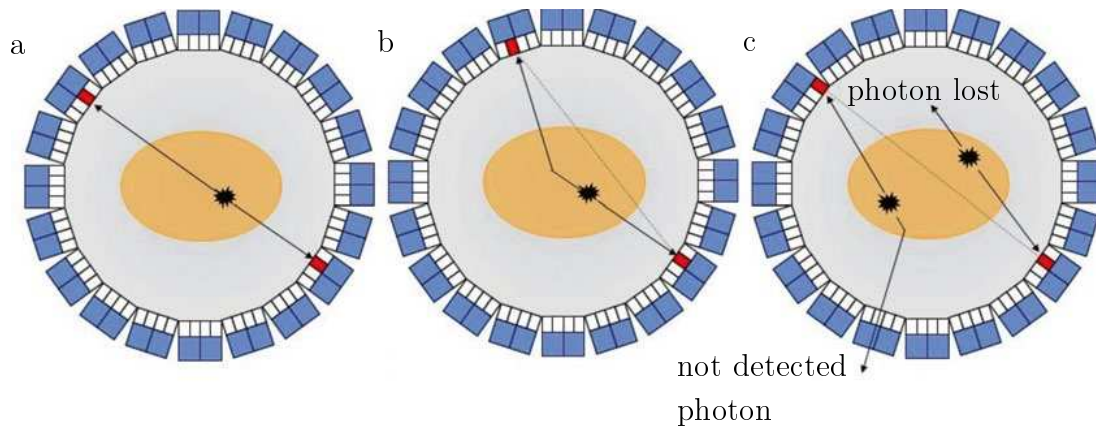


Figure 2.16: True (a), scattered (b) and random (c) coincidences types. Figure adapted from [67].

matrix, where each matrix element corresponds to respective detectors pair along a LOR. Matrix rows represent the activity projection at a specified angle ϕ . Matrix columns represent the radial offset (r) from the scanner center (see Fig. 2.17). The relationship between matrix elements and place of annihilation in x and y coordinates is given by the following formula:

$$r = x \cos \phi + y \sin \phi \quad (2.9)$$

Due to the fact that annihilations located in a single point x, y leave a sinusoidal trace in the matrix, this 2-D matrix is known as a sinogram ($s(r, \phi)$) [53].

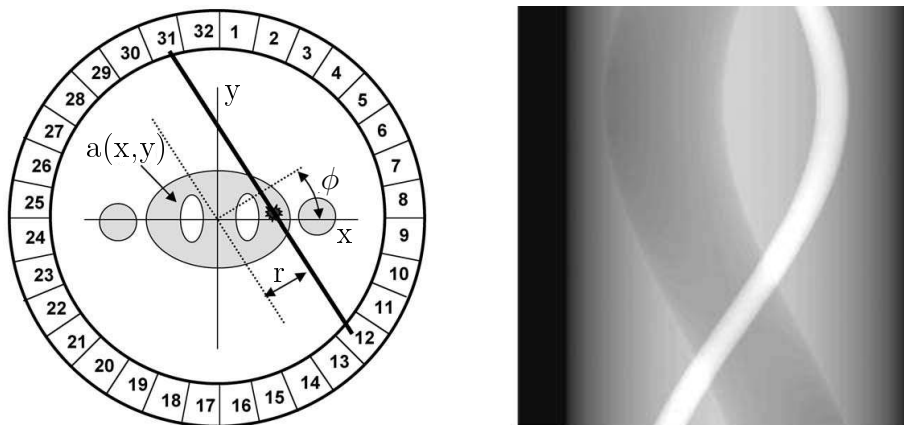


Figure 2.17: (left) Example of a PET scanner build out from 32 detectors with shown method of determination of r and ϕ . (right) Sinogram of simulated cylindrical object with two regions of different concentration of radioactivity. Figures adapted from [53].

2.5 Time-of-flight method

Two back-to-back photons can be registered by detectors with slightly different times. This difference in arrival time can be used to estimate the most likely annihilation point along a LOR (see Fig. 2.18) as follows:

$$D = \frac{c\Delta t}{2} \quad (2.10)$$

where D is a distance between midpoint of the LOR and most likely point of annihilation, Δt is photons arrival time difference and c denotes the speed of light. Δt equal to zero means annihilation in the LOR middle point. Moreover, Δt changes only about 67 ps per 1 cm of distance difference D due to speed of light in air equal to about $30 \frac{cm}{ns}$. Place of annihilation is blurred due to limited detectors time resolution. Time resolution of ~ 375 -600 ps corresponds to ~ 5.6 -9 cm uncertainty on the reconstructed annihilation point position [55, 68]. Localization uncertainty at 600 ps is 3 times smaller than average patient diameter equal to 27 cm [69].

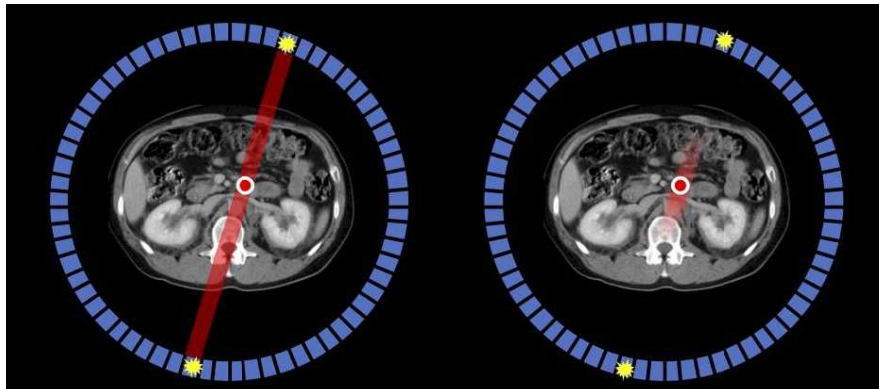


Figure 2.18: Estimation of annihilation point along a LOR without TOF information (left) and with TOF information (right). Figure adapted from [64].

Information about time-of-flight (TOF) can improve image quality due to reduction of random and scattered events contribution. On the other hand, TOF method cannot be used for direct image reconstruction due to too low time resolution of the presently used detectors [52, 55, 68]. Gain of using TOF increases with time resolution improvement but also with increasing of patient diameter and leads to higher image contrast as one can see in Fig 2.19 [70].

Time-of-flight method was introduced commercially by Philips Medical System in a fully 3D TOF PET/CT scanner in June 2006. The GEMINI TF was based on lutetium-yttrium oxyorthosilicate (LYSO) scintillators and photomultipliers. System time resolution was equal to 585 ps while spatial resolution near to scanner center was measured

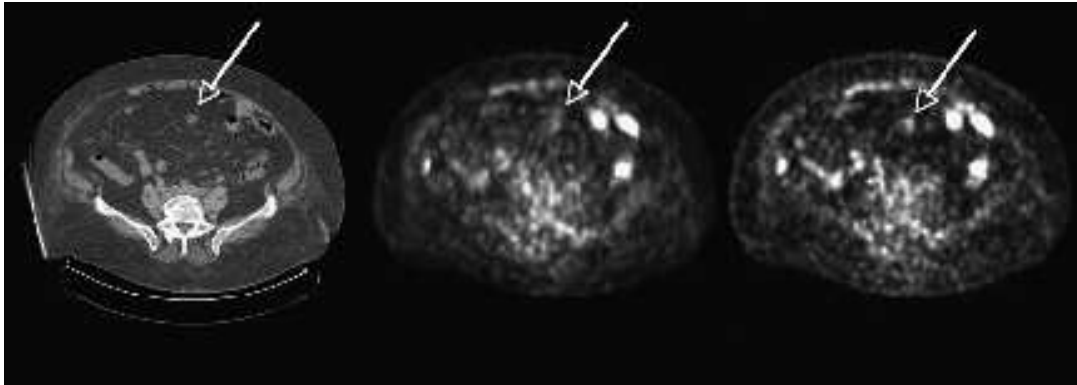


Figure 2.19: Transverse section of case of colon cancer diagnosed for patient with BMI equal to 46.5. (left) CT scan with low dose, (middle) non-TOF and (right) TOF MLEM. A dot well visible in CT scan pointed at by an arrow has better contrast in the image with a TOF method in a contrary to the non-TOF result. Figure adapted from [70].

to be 4.8 mm [71]. Currently GE Healthcare Discovery MI (based on LBS crystals and SiPMs) obtains time resolution equal to 385 ps [72] while Siemens Biograph Vision (based on LSO and SiPMs) obtains 249 ps [73]. Vereos PET/CT, announced in Chicago by Philips on December 1, 2013, is based on LYSO scintillator and digital SiPM photodetectors and achieves timing resolution equal to 310 ps FWHM and TOF localization accuracy equal to 4.6 cm [74, 75].

2.6 Radiopharmaceuticals

Positron Emission Tomography uses positron-emitting radionuclides to imagine biological processes. Radionuclide is attached to a compound with useful properties from the nuclear medicine point of view. The compound has to be safe and nontoxic as well its production has to be cheap and easy. The type of compound is selected based on physiologic processes taking place in an organ [76]. This combination of radionuclide and compound is called a radiopharmaceutical.

For clinical application radionuclide half-life should be in the range of minutes to hours. Too short half-life is disadvantageous from the point of view of process of radiopharmaceutical preparation and patient examination. On the other hand, too long half-life can result in high radiation dose for patient and hospital staff. Another important property of radionuclide is its ease of incorporation into biomolecules without significant change of their biochemical character. Example of few most commonly used radionuclides are listed in Tab. 2.4.

One of the methods of compounds labeling is direct substitution of the molecule stable

atom with a radioactive one. Radiopharmaceutical created from an isotope of one of the easily available in nature elements such as e.g. carbon or hydrogen will be metabolised in the same way as the original. Another approach of pharmaceuticals labeling is creation of analog by its modification which allows for usage of rare radioisotopes such as fluorine or iodine [51].

Table 2.4: Physical properties of some of the most commonly used radionuclides for PET imaging. Table adapted from [51, 77, 78].

Radionuclide	Decay Mode	Principal Photon Emission	Half-life
^{11}C	β^+ (99.75%)	511 keV	20.3 min
^{13}N	β^+ (99.82%)	511 keV	10.0 min
^{15}O	β^+ (99.89%)	511 keV	2.07 min
^{18}F	β^+ (96.86%)	511 keV	110 min
^{123}I	de-excitation (83.25%)	159 keV	13.0 hr

Radionuclide ^{11}C can be used to imagine the DNA synthesis. ^{13}N and ^{15}O are used for observation of blood flow. ^{123}I is absorbed in gastrointestinal tract and taken up by thyroid which allows for imaging of thyroid diseases.

The most widely used and the most important radionuclide is ^{18}F due to its high half-life. A combination of ^{18}F and 2-Deoxy-D-glucose (FDG) is the only radiopharmaceutical used in daily routine for cancer imaging. Tumors have accelerated glucose metabolism and accumulate much more amount of FDG in contrary to healthy tissue. Moreover, positron emitted by ^{18}F has low energy (0.64 MeV) and short range in tissue (max 2.4 mm) which makes FDG an ideal radiopharmaceutical [79]. Typically, the amount of injected dose of FDG is equal to 2.0-5.0 MBq/kg for PET scanner with BGO crystals [80].

2.7 New trends in PET technology

Performance of PET scanners have changed significantly over last decades beginning from single-ring detectors to full 3-dimensional scanners. Progress in electronics technology also has a big impact in this field. Despite many improvements, present PET tomographs have still few limitations such as low signal-to-noise ratio crucial to image quality, low spatial resolution determined mainly by distance traveled by positron in tissue before annihilation, long scan time in the range of 10-20 minutes and device cost in the order of several million PLN [68].

Nowadays, the standard photodetector used in PET scanners is vacuum photomultiplier (PMT), but in modern devices they are replaced by silicon photomultipliers (SiPMs). SiPM is build from an array of micro avalanche photodiodes (APDs) operated in Geiger

mode [68,81] as one can see in Fig. 2.20. SiPM can work in strong magnetic field. Compact size helps eliminate light sharing and improves spatial resolution. Output from all cells in SiPM is proportional to energy deposited in a scintillator. Silicon photomultipliers are sensitive to temperature variation and preferable operating temperature should be low. Temperature sensitivity was improved in digital SiPM (dSiPM) which immediately converts detected photons to digital signals [55,68,81,82].

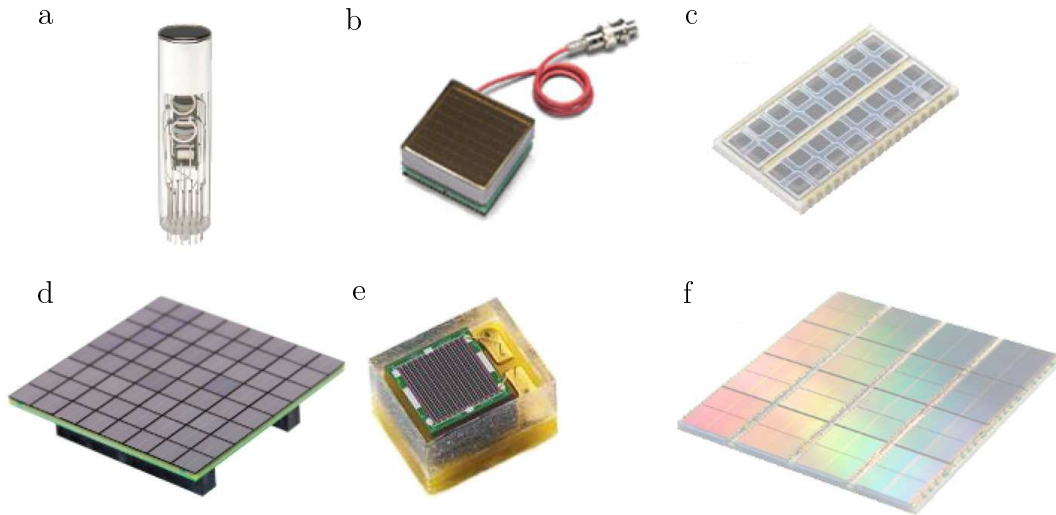


Figure 2.20: Different types of photodetectors: (a) PMT, (b) flat-panel position-sensitive PMT, (c) avalanche photodiode array, (d) SiPM, (e) SiPM detector, (f) dSiPM. Figure adapted from [82].

SiPMs have excellent photon detection efficiency (PDE) greater than 40% in contrary to about 25% for PMTs which makes them an ideal candidate for TOF applications. Moreover, SiPMs have very fast timing response and their compact size allows for tightly packing and eliminating gaps between photodetectors as it is in case of using of PMTs [68].

Scintillator technology for PET has not been developing so fast as modern electronics. It was shown recently that codoping LSO:Ce³⁺ with Ca²⁺ can improved timing resolution by reducing decay time from 42 ns to \sim 32 ns [83]. Similar characteristics to LSO:Ce:Ca (0.4%) such as e.g. stopping power and comparable light output was obtained by Stanford group with LGSO:Ce crystal. LGSO has \sim 30% faster decay time in comparison to LYSO [68,84]. Another approach is usage of halide scintillators such as CeBr₃ or LaBr₃. They are characterized by two to three times higher light output than LYSO and ultrafast timing resolution (up to 75-80 ps in experiments with fast SiPMs). Their biggest flaw is lower stopping power in comparison to LYSO. Moreover, halide scintillators are hygroscopic and can be used only for experimental purposes [68].

Scintillators manufacturers still have to find solution that will reconcile good timing performance, cost of material and simple production methods.

2.8 Total-body PET (EXPLORER)

Small axial field of view, the main limitation of current PET systems, leads to fact that full-body scan is constructed from series of several single scans [85]. On the other hand, overlapping bed positions have created the possibility of finding cancer tumors and metastasis [86]. Series of body scans were obvious in the past but today researchers are focused on total-body PET scanner. Simulations have shown that ~ 40 times more events will be detected for the same activity with this new solution. Moreover, signal-to-noise ratio could be increased by a factor of ~ 6.6 which would lead to better image quality. Another advantage of the total-body PET is the possibility of decreasing the time of examination or effective radiation dose with current achievable signal-to-noise ratio (SNR) [84].

The multi-institutional consortium led by University of California, University of Pennsylvania and Berkeley Lab has completed work on the first total-body PET scanner. Total-body imager uEXPLORER is a part of the EXPLORER project. uEXPLORER is build out from 8 detector rings. Each ring is formed by 24 detector modules. One module is created from 5 (transaxial) and 14 (axial) blocks. 7 (transaxial) times 6 (axial) LYSO crystals create one block. Dimensions of a single crystal are as follows: $2.76 \times 2.76 \times 18.1 \text{ mm}^3$. Each block is read-out by 4 SiPMs. Axial field of view is equal to 194 cm. Transaxial FOV is equal to 68.8 cm while the scanner diameter is equal to 76 cm (see Fig. 2.21). Even up to 5 rings can be axially in coincidence. Coincidence time window is in the range of 4.5-6.9 ns. Manufacturers claim that the energy resolution of the uEXPLORER is equal to 11.7% for 511 keV gamma quanta and its timing resolution is equal to 430 ps [64, 65, 68, 85, 87].



Figure 2.21: Photos of uEXPLORER adapted from [87].

The main advantages of this solution are faster and better imaging and possibility

of decreasing the dose absorbed by the patient during the PET scan (up to 40-fold reduction). The main clinical applications will be low-dose and ultra-fast scanning of pediatric patients, opportunity to find even small lesions and imaging of total-body tumor perfusion. Fast scan will reduce respiratory motion contribution and will allow for achieving higher resolution [87,88]. First human images one can find on Fig. 2.22.

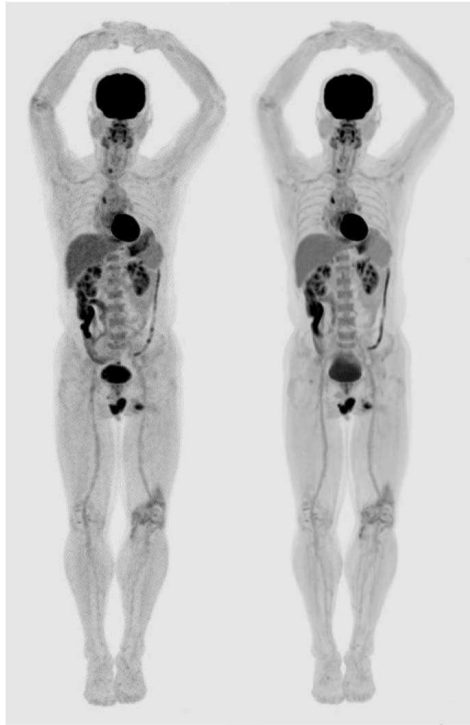


Figure 2.22: (left) 1 minute scan of 61-yo male (81 minutes post injection) and (right) 20 minutes scan (82 minutes post injection). Patient weight was equal to 65 kg while height was equal to 164 cm. Figures adapted from [88].

Chapter 3

NEMA norms

Protocols for the determination of the performance of PET scanners has been initially unified in the United States of America by the Society of Nuclear Medicine and continued by the National Electrical Manufacturers Association (NEMA). The first official standard was published in 1994 as NU 2-1994. The European Union has also started working on performance tests procedures in the same period of time and established the International Electrotechnical Commission (IEC) standard. Standards unification was necessary due to differences in detectors and scanner configurations between different manufacturers. This unification guarantees similar performance level between tomographs. Standards are constantly updated by the NEMA as well as by the IEC. International Standard IEC is valid in Europe, while NEMA is the American norm, but the majority of articles in this field refer to NEMA procedure as relevant for PET scanners inspection and for comparison between different producers [89].

For all the standardized procedures, the scanner accessible diameter has to be larger than 260 millimeters. Scanner operating mode for each measurement should be specified. Parameters of the reconstruction algorithm should be fixed. The recommended source for all tests is ^{18}F , but if manufacturer employs different measurement methods then traceability of the used methods in relation to the official tests should be shown [89].

NEMA norm defines parameters such as spatial resolution, sensitivity as well as includes instruction how to obtain value of scatter fraction, count losses and random coincidences. In the following subsections each of these parameters and procedures are explained in details.

3.1 Spatial resolution

Tomograph ability to distinguish two emitting points from each other after image reconstruction is referred as the spatial resolution. Image reconstruction of point source

measured in air should be done without smoothing and apodization. Spatial resolution is the best-case comparison between different PET manufacturers, but does not reflect the quality of the true imaging of patient [89,90].

To obtain scanner spatial resolution the width of point spread functions (PSF) of a reconstructed image should be calculated in two directions (e.g. radially and tangentially). Moreover, axial resolution also should be specified. Suggested radionuclide is ^{18}F with an activity sufficiently low to meet one of the two requirements: the dead time is smaller than 5% or the rate of random coincidences is smaller than 5% of the total events rate.

The inside diameter of point source in a form of capillary with small amount of activity should be smaller than 1 mm and the outside diameter should be less than 2 mm while the axial extent of radioactive part of capillary should be smaller than 1 mm. Sources should be placed in six fixed positions parallel to the tomograph long axis:

- at the center of the axial field-of-view (FOV) and at the three-eighths of the axial FOV calculated from the FOV center,
- at 1 cm, 10 cm and 20 cm in the transverse direction.

If the FOV of a scanner does not cover 20 cm position then the manufacturer can omitted this source location.

The transaxial positioning accuracy should be equal to ± 2 mm for sources placed with 1 cm offset while for sources placed with 10 cm or 20 cm offset the accuracy should be equal to ± 5 mm. The axial positioning accuracy is constant for all sources and is equal to ± 2 mm. Collected number of counts should be equal to at least one hundred thousand for each response function. Image reconstructions should be done with filtered backprojection [91,92].

Full width at half-maximum (FWHM) and full width at tenth-maximum (FWTM) of point-spread function (PSF) in all three dimensions should be determined from the point source response function. The standard deviation (σ) of a Gaussian function fitted to a profile is related to FWHM by the relationship:

$$FWHM = \sigma\sqrt{8\ln 2} \quad (3.1)$$

FWHM and FWTM in all three directions should be averaged over axial positions for 1, 10 and 20 cm offset [52,89].

Example of spatial resolution measurements for three GE Discovery MI DR PET/CT systems was presented in [93]. Measurements were performed with ^{18}F point sources with the axial length smaller than 1 mm. Larger lengths were discarded. Sources were created by droplets absorbed at the end of hematocrit capillary tubes sealed by clay. Sources were positioned along y-axis at 1, 10 and 20 cm from the center. Two 60 s acquisitions

were performed for axial FOV centre and one-eighth of the axial FOV. For each acquisition more than 500 kcount was collected.

Similar method was presented in [94]. Inner diameter of glass capillary tube was equal to 0.8 mm while the axial source length was smaller than 1 mm. Activity of source was measured as 1.4 MBq at the beginning of the spatial resolution measurement. No filters and corrections were used.

3.2 Scatter fraction, count losses and random event rate measurement

The main aim of this procedure is to determine the relative system sensitivity to scattered radiation and effects of system dead time as well as estimation of random events rate for different radioactivity levels. There are two methods of sensitivity determination according to NEMA proposed in NU 2-2012 standard:

- measurement of random coincidences by delaying event window or calculation based on event rate from a single detector.
- alternative method for scanners without possibility of random coincidences rate measurement. In this method only three final acquisitions are taken into account. Details are explained later in the text.

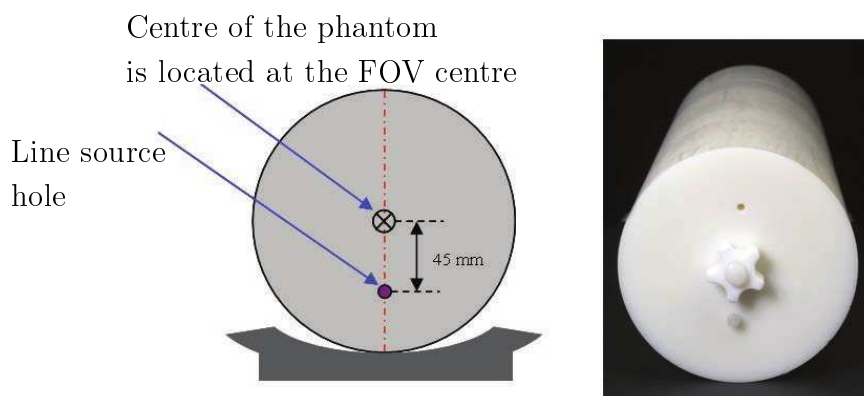


Figure 3.1: Positioning of the PET Scatter Phantom on the bed. Figures adapted from [95].

To perform this procedure a dedicated cylindrical test phantom is needed. Solid PET Scatter Phantom built from polyethylene has outside diameter equal to 203 ± 3 mm and length equal to 700 mm. Cylinder has a drilled hole with diameter equal to 6.4 ± 0.2 mm located with an offset equal to 4.5 cm relative to the phantom central axis as one can see

in Fig. 3.1. Plastic tube made from clear polyethylene with length equal to 80 cm is an insert for the PET Scatter Phantom. Inside diameter of the insert is equal to 3.2 ± 2 mm while the outside diameter is equal to 4.8 ± 3 mm. The central part of the insert with length equal to 700 ± 20 mm should be uniformly filled with a water solution containing ^{18}F isotope with a well defined activity (e.g. 70 mCi for 2D scan, 40 mCi for 3D scan) and placed in the hole. The corrected initial activity (A_{cal}) should be calculated from equation:

$$A_{cal} = A_{cal,meas} \frac{700 \text{ mm}}{L_{meas}} \quad (3.2)$$

where: $A_{cal,meas}$ is the activity measured by dose calibrator and L_{meas} is the length of filled region measured after filling.

To start measurements test phantom has to be placed in the scanner field-of-view on the patient bed and the activity region of the line source has to be centered with respect to the phantom which should be centered in transverse and axial FOV with an accuracy of 5 mm. Regular measurements should be done with intervals frequent than half of the radionuclide half-life until true events losses will be less than 1%. Each acquisition time should be smaller than one quarter of radionuclide half-life. Number of measured prompt counts should be larger than 500 000. Sinograms for prompt and random events should be generated for all acquisitions of slice i for entire axial FOV without corrections applied.

In the first method data analysis consists of few steps to be processed for each sinogram i of acquisition j . In the first step all pixels which are located farther than 12 cm from the center of scanner transaxial FOV should be set to zero as one can see in Fig 3.2.

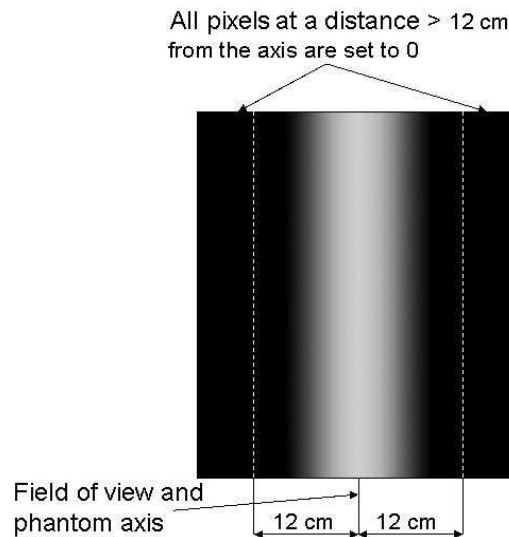


Figure 3.2: Example of sinogram with the ± 12 cm range marked. Figure adapted from [96].

In the next step, the value of maximum pixel should be determined for each projection angle ϕ , e.g. for each sinogram row. Later, each projection should be shifted in a way that the maximum pixel is aligned with sinogram central pixel. Sum projection is produced by summing aligned sinogram over projection angle, e.g. by summing up all rows of aligned sinogram. C_{Lij} and C_{Rij} at a distance ± 20 mm from the center of unshifted sinogram determines a range at the projection sum profile (see Fig. 3.3). To obtain number of random and scattered counts ($C_{r+s,i,j}$), average of C_{Lij} and C_{Rij} should be multiplied by number of pixels (including fractional values) between the edges of ± 20 mm range and added to the integral of counts from pixels outside this range. Total number of counts ($C_{TOT,i,j}$) can be calculated from the sum of all pixels in the sum projection. Additionally, the average activity for each acquisition should be calculated.

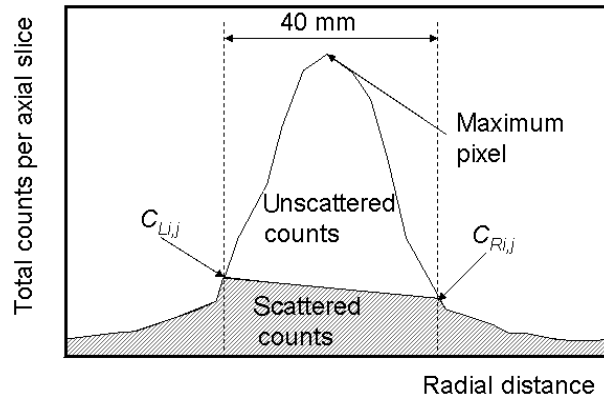


Figure 3.3: Projection sum profile with the ± 20 mm range marked. Figure adapted from [96].

System scatter fraction for acquisition j can be calculated from equation:

$$SF_j = \frac{\sum_i C_{r+s,i,j} - \sum_i C_{r,i,j}}{\sum_i C_{TOT,i,j} - \sum_i C_{r,i,j}} \quad (3.3)$$

It is possible to obtain another system parameters, based on measurement of count rates, such as:

- total event rate ($R_{TOT,j}$)

$$R_{TOT,j} = \frac{1}{T_{acq,j}} \sum_i C_{TOT,i,j} \quad (3.4)$$

- true event rate ($R_{t,j}$)

$$R_{t,j} = \frac{1}{T_{acq,j}} \sum_i (C_{TOT,i,j} - C_{r+s,i,j}) \quad (3.5)$$

- random event rate ($R_{r,j}$)

$$R_{r,j} = \frac{1}{T_{acq,j}} \sum_i C_{r,i,j} \quad (3.6)$$

- scatter event rate ($R_{s,j}$)

$$R_{s,j} = \frac{1}{T_{acq,j}} \sum_i (C_{r+s,i,j} - C_{r,i,j}) \quad (3.7)$$

where $T_{acq,j}$ is time of the acquisition of measurement j . Based on this parameters it is possible to calculate the noise equivalent count rate (NEC) for each measurement j from the equation:

$$R_{NEC,i,j} = \frac{R_{t,i,j}^2}{R_{TOT,i,j} + kR_{r,i,j}} \quad (3.8)$$

where $k=0$ for scanners without direct random coincidences subtraction and $k=1$ for scanners with subtraction. Peak of NEC values and corresponding concentration of the radioactive tracer is a guide for determination of the optimal radioactivity used in clinical routine with patients.

For systems without possibility of random coincidences measurement the three last acquisitions j' below 1% of the true events rate should be used to determine the system scatter fraction:

$$SF = \frac{\sum_i \sum_j C_{r+s,i,j'}}{\sum_i \sum_j C_{TOT,i,j'}} \quad (3.9)$$

where: $C_{r+s,i,j'}$ has a negligible number of random events and $C_{TOT,i,j'}$ includes only true and scatter events. The total event rate and true event rate equation remain the same, but there is a difference for:

- random event rate ($R_{r,j}$)

$$R_{r,j} = R_{TOT,j} - \frac{R_{t,j}}{1 - SF} \quad (3.10)$$

- scatter event rate ($R_{s,j}$)

$$R_{s,j} = \frac{SF}{1 - SF} R_{t,j} \quad (3.11)$$

And subsequently the NEC equation has exactly the same form:

$$R_{NEC,j} = \frac{R_{t,j}^2}{R_{TOT,j} + kR_{r,j}} \quad (3.12)$$

To report results one has to describe configuration of phantom and patient bed as well as method which was used for alignment of sinograms projection. One has to plot these five

quantities ($R_{TOT,j}$, $R_{t,j}$, $R_{r,j}$, $R_{s,j}$, $R_{NEC,j}$) as a function of average concentration of the effective activity of the radiotracer $a_{ave,j}$ and report peaks visible in the plots for true count rate ($R_{t,peak}$) and NEC ($R_{NEC,peak}$) ratio. The radiotracer concentration at which $R_{t,peak}$ and $R_{NEC,peak}$ is reached should also be reported. The average radioactivity concentration can be calculated from the following formula:

$$a_{ave} = \frac{A_{ave}}{V} \quad (3.13)$$

and:

$$A_{ave} = A_{cal} \frac{T_{1/2}}{T_{acq} \ln 2} \exp\left(\frac{T_{cal} - T}{T_{1/2}} \ln 2\right) \left(1 - \exp\left(\frac{-T_{acq}}{T_{1/2}} \ln 2\right)\right) \quad (3.14)$$

where V is the PET Scatter Phantom total volume (22 000 cm³), A_{cal} is the source activity corrected for the length, $T_{1/2}$ is radionuclide half-life, T_{acq} is the time of acquisition, T_{cal} is phantom radioactivity calibration time and T is time of measurement start.

For systems with possibility of random events estimation SF_j as a function of $a_{ave,j}$ should be determined. For systems without such estimation only the value of SF should be reported.

Example of measurement with PET Scatter Phantom was presented in details in article [94]. Activity of ¹⁸F solutions filled the tube was equal to 1049 MBq at the beginning of the tests. Acquisition was performed for about 14 hours.

About 851 MBq of ¹⁸F-FDG was used in experiments with silicon photomultipliers based TOF PET/CT presented in [97]. Source activity was high enough to obtain count rates beyond expected NECR peak. Measurements were done for different radioactivity levels.

3.3 Sensitivity

Scanner sensitivity is related to the detected count rate for a given source activity and is expressed by measured true coincidences rate. Sensitivity measurement method is based on the fact mentioned before that positrons have to thermalize and travel some distance before annihilation and creation of a pair of gamma quanta, thus some amount of the absorber has to surround the source. Increase of the absorber thickness allows for extrapolation of the coincidence rate to the value corresponding to absence of the absorber [96].

During tests a dedicated phantom is required. Sensitivity phantom consists of five aluminum tubes with length equal to 700 mm (see Fig. 3.4). Inside and outside diameter of each sleeve was shown in Tab. 3.1. The most inner (sixth) tube made from a polyethylene should be uniformly filled with a water mixed with a radioactive tracer. Radioactivity has to be measured with dose calibrator for a known period of time. The corrected initial activity should be calculated according to equation 3.2. The suggested radionuclide

is ^{18}F with an activity sufficiently low to fulfill condition that random coincidences rate is smaller than 5% or percent dead time losses are smaller than 5% [89,96].

Table 3.1: Sensitivity phantom details. Table adapted from [89].

Tube	Inside diameter (mm)	Outside diameter (mm)	Length L (mm)
1	3.9	6.4	700
2	7.0	9.5	700
3	10.2	12.7	700
4	13.4	15.9	700
5	16.6	19.1	700

Positioned in the transaxial FOV centre phantom has to be supported at each end and the measurements should start with the smallest aluminum tube with the source in the polyethylene tube inside. During next acquisition the thickness should be increased with the next tube and the procedure is repeated until all sleeves have been used. Each measurement should be saved separately. 10 000 of true events per slice should be collected. Measurements should be also performed for 10 cm radial offset from the transaxial FOV center.

Sensitivity measurements should be performed during acceptance tests and at any time when the detectors appear to be malfunctioning. For the image slice for which line-of-response crosses over the detector axis the single slice should be rebinned in order to assign counts for oblique LOR. Starting measurement time (T_j), the acquisition time ($T_{j,acq}$) as well as the number of counts should be noted. The rate ($R_{i,j}$) for j -th sleeve can be calculated by dividing i -th slice counts by duration. The total count rate (R_j) corrected for the radioactive decay can be calculated from the formula:

$$R_{CORR,j} = \frac{(T_{j,acq} \ln 2) \exp\left(\frac{T_j - T_{cal}}{T_{1/2}} \ln 2\right)}{T_{1/2} (1 - \exp\left(-\frac{T_{j,acq}}{T_{1/2}} \ln 2\right))} R_j \quad (3.15)$$

where T_{cal} is calibration radioactivity measurement time, $T_{1/2}$ is radionuclide half-life. To obtain count rate without attenuation ($R_{CORR,0}$), data should be fitted with the following equation:

$$R_{CORR,j} = R_{CORR,0} \exp(-\mu_M 2X_j) \quad (3.16)$$

where X_j is the accumulated thickness of the tubes wall, while μ_M stands for the sleeve linear attenuation coefficient.

Finally, detector sensitivity (in counts/sec/kBq) can be obtained from the following formula:

$$S_{tot} = \frac{R_{CORR,0}}{A_{cal}} \quad (3.17)$$

Axial sensitivity profile can be determined by plotting the sensitivity for each slice from measurement with the smallest tube at the central position [89,96].



Figure 3.4: Sensitivity phantom with different tubes visible (left) and polyethylene tube (right).

Activity of ^{18}F used during sensitivity measurements and presented in article [93] was equal to 4 ± 0.5 MBq. This small radioactivity allowed to fulfill the condition that contribution of random events had to be below 5%. In case of 5 MBq of solution of ^{18}F used in tests shown in article [94] acquisition time was equal to 300 s for each of the five measurements.

Chapter 4

J-PET scanner

The Jagiellonian Positron Emission Tomography (J-PET) scanner constructed at the Jagiellonian University is under continuous development as mentioned in Ch 1. The previous reasearch step consisted of studies on single and dual strip systems and construction and commisioning of small barrel prototype [1,98–100]. In contrary to commercial scanners, J-PET was built out of three layers of axially arranged organic scintillators which forms a cylindrical chamber as one can see in Fig. 4.1. Small light attenuation length of those scintillators allowed to get axial field-of-view equal to 50 cm. Moreover, their good timing properties and lower price, in comparison to crystals, opened perspectives for the construction of cost-effective total-body PET scanners in future. Furthermore, readout placed outside the detection chamber will allow for easy extension of the axial field-of-view (AFOV) and constructing of the PET/MR hybrid [3].

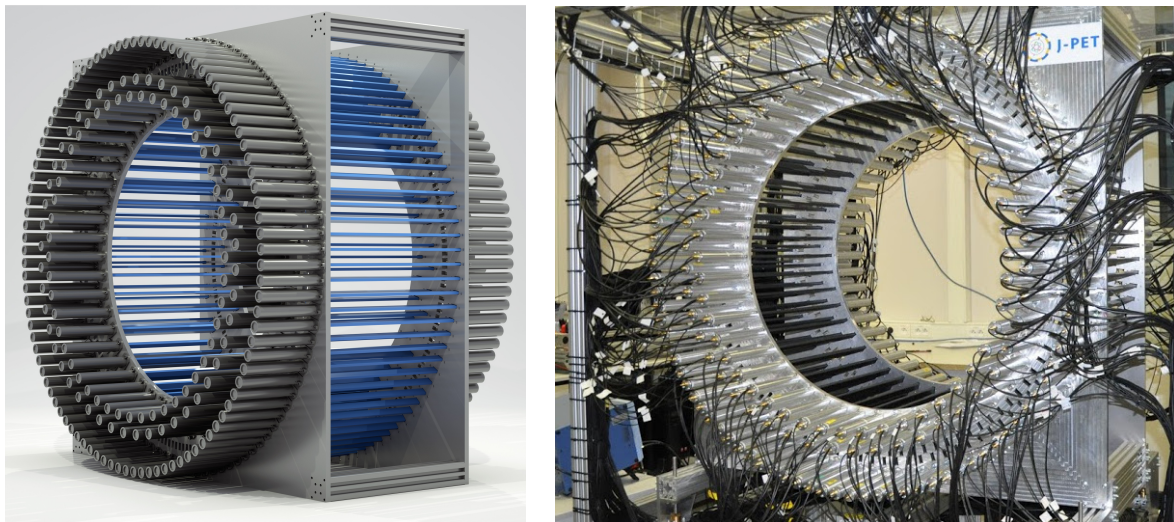


Figure 4.1: (left) Schematic view of the J-PET scanner. (right) J-PET prototype [3]. Courtesy of the J-PET group.

In this chapter general concept, geometry and construction details of this new PET scanner will be explained.

4.1 General concept of the J-PET detector

J-PET scanner is optimized for detection of back-to-back gamma quanta from electron-positron annihilations. Photons interact with scintillator material predominantly via Compton scattering (see section 2.1). Light produced in each scintillator by incoming photons is detected and converted to electrical signals by photomultipliers placed at opposite ends of each scintillation strip as one can see in the left panel of Fig. 4.2.

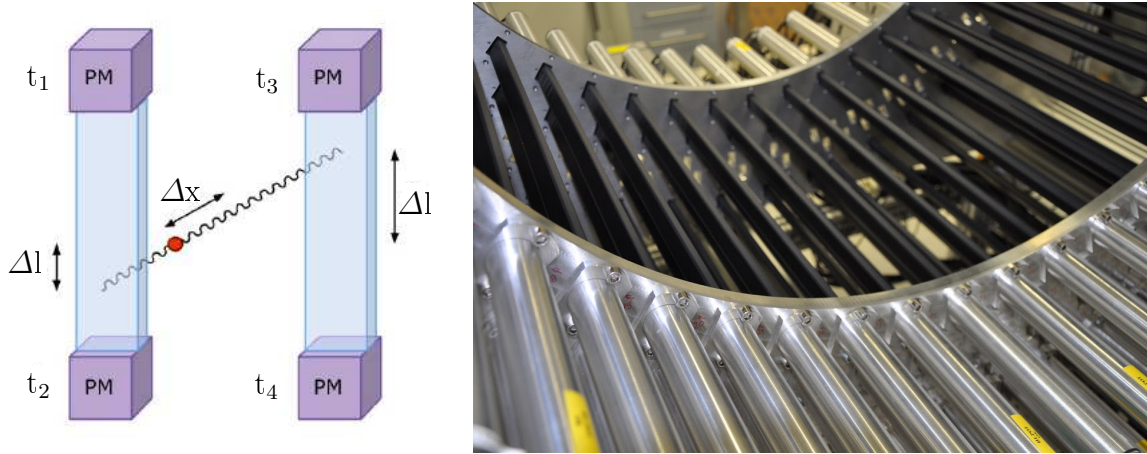


Figure 4.2: (left) Two detection modules setup. Single detection module is build from organic scintillator and two photomultipliers (PM). Figure adapted from [3]. (right) Scintillators are wrapped with lightproof material (black) and connected to photomultipliers (silver tubes). Courtesy of the J-PET group.

A point of photon interaction with scintillator can be easily calculated from the following equation:

$$\Delta l = \frac{(t_1 - t_2) \cdot V}{2} \quad (4.1)$$

where Δl stands for distance between point of interaction and scintillator center, t_1 and t_2 denote light signal arrival time at each end of scintillator and V stands for an effective light velocity inside the scintillator. In the next step, annihilation position along LOR can be obtained from the following equations:

$$\Delta t = \frac{t_1 + t_2}{2} - \frac{t_3 + t_4}{2} \quad (4.2)$$

$$\Delta x = \Delta t \cdot \frac{c}{2} \quad (4.3)$$

where Δx means distance between annihilation point and the LOR midpoint and c is the speed of light.

Due to the type of used scintillators (see section 2.2.1), the J-PET scanner uses time information instead of energy deposition. Very good time properties of EJ-230, e.g. fast signal rise time equal to 0.5 ns as well as decay time equal to 1.8 ns, allow for achieving very good time resolution in the order of 220 ps (σ) [3]. Signal obtained from photomultiplier is sampled in the voltage domain at four thresholds by FPGA (Field-Programmable Gate Array) units as one can see in Fig. 4.3 [101].

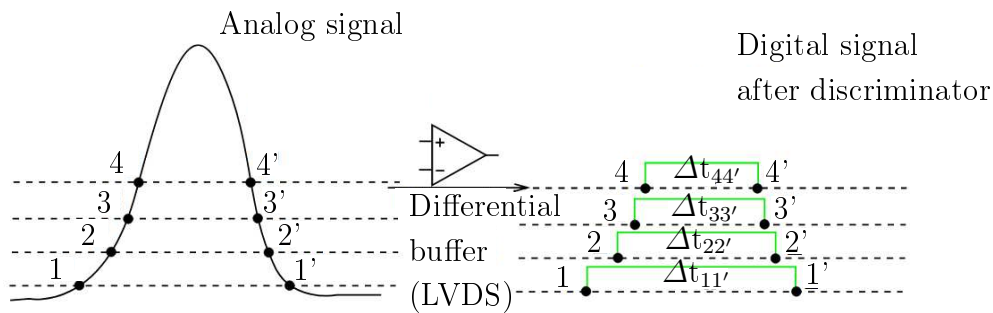


Figure 4.3: Analog signal is probed at four thresholds at rising and falling edge. Figure adapted from [101]

Analysis of data obtained from the J-PET detector is done by the J-PET Framework, which is open-source software developed in C++ language and based on the ROOT package. This platform enables for data preselection and calibration procedures as well as for user-level analysis and reconstruction [102].

4.2 J-PET design

The use of plastic scintillators is an innovative concept. For many years it seemed impossible to build a PET scanner from organic scintillators due to lower probability of gamma quantum interaction with scintillation material in comparison to crystals. The main aim of the J-PET group was to show that it is possible to build such a scanner.

J-PET tomograph (see right panel of Fig. 4.1) is constructed from 192 plastic detection modules divided into three layers with radius equal to 42.5 cm, 46.75 cm and 57.5 cm subsequently. Each detection module consists of 50 cm long and 7 x 19 mm² intersection size EJ-230 scintillator and two R9800 Hamamatsu photomultipliers. First and

second layer is formed from 48 scintillators while the most outer layer is formed from 96 scintillators as one can see in Fig. 4.4.

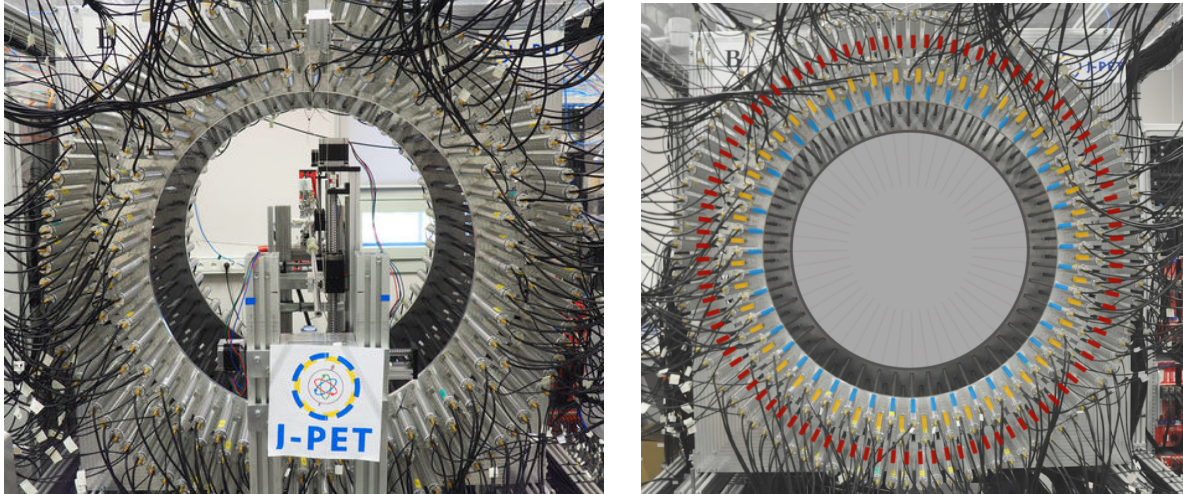


Figure 4.4: (left) Front view of the J-PET detector. (right) First and second layer is formed from 48 scintillators (blue and yellow), while third layer is formed from 96 scintillators (red) [103]. Courtesy of the J-PET group.

The first step in the J-PET detector construction process was to choose the optimal scintillation material. Studies of different polymer scintillators produced commercially were done by members of the J-PET group. The main considered features were connected with time properties and light propagation. The main criteria taken into account were: light output, rise and decay time and bulk light attenuation length. Based on the obtained results, EJ-230 produced by Scionix was chosen as the best candidate due to its ultra-fast timing and low light self-absorption.

EJ-230 is the best choice for detectors with dimension larger than 10 cm. Its light attenuation length is equal to 120 cm. As it was mentioned in Tab. 2.3, decay time of the EJ-230 scintillator is equal to 1.5 ns while its light output amounts to 64 % Anthracene and, as it was mentioned earlier in this chapter, rise time is equal to 0.5 ns. This scintillator can work in temperature range from -20°C up to 60°C and it is stable with silicone greases used as optical connector between scintillator and photomultiplier.

Based on the emission spectrum of EJ-230 and results from scintillation light response tests of different photomultipliers, the J-PET group chose the R9800 photomultiplier produced by Hamamatsu as the best candidate for further purposes [104]. Comparison between scintillator emission spectrum and photomultiplier spectral response one can find in Fig. 4.5.

The R9800 photomultiplier has the effective diameter of photocathode equal to 22 mm which is suitable for scintillator size. Moreover, R9800 is characterised by fast time

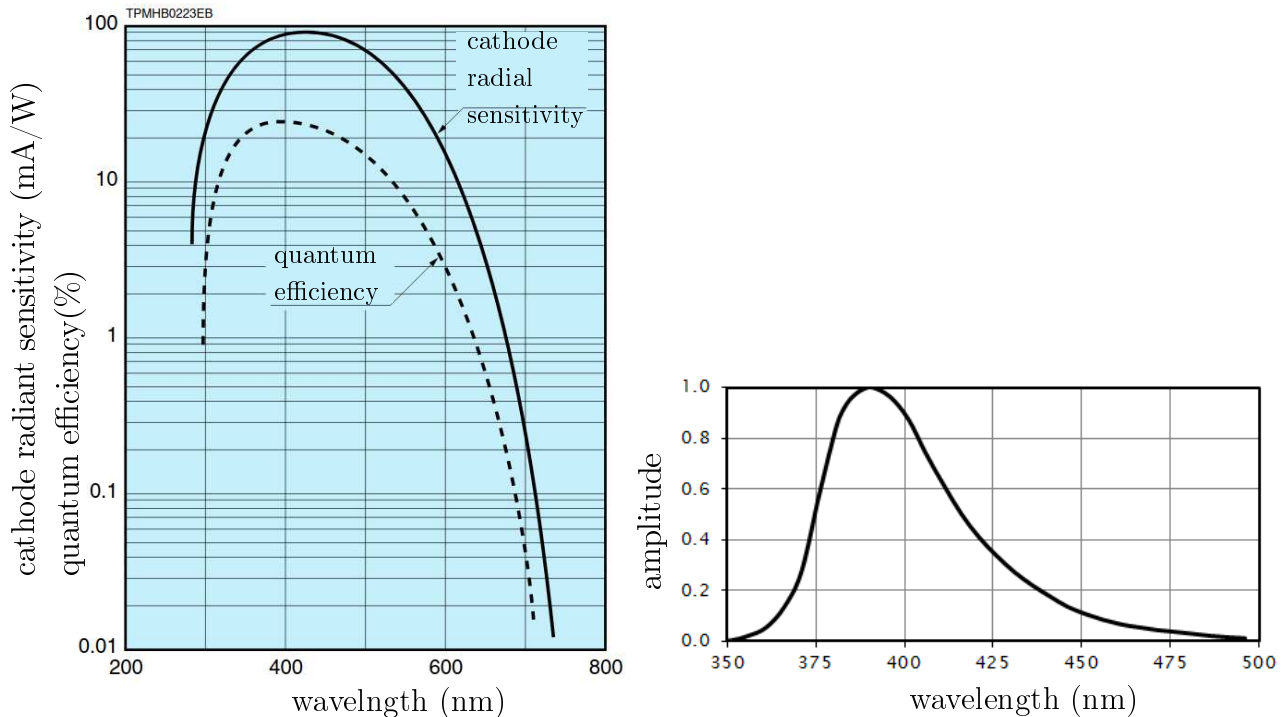


Figure 4.5: (left) Spectral response of the R9800 photomultiplier. Figure adapted from [105]. (right) EJ-230 emission spectrum. EJ-230 is an equivalent of BC-420 produced by Saint Gobain. Figure adapted from [59].

response. Rise time and transit time is equal to 1 ns and 11 ns, respectively. This photomultiplier can operate in temperatures from -30°C up to 50°C .

4.3 Data acquisition system

Due to the number of photomultipliers assembled in the J-PET detector there is 384 analog channels to be read in trigger-less mode by dedicated data acquisition system (DAQ). The main component of this system is Trigger Read-out Board (TRB), which contains 4 peripheral FPGAs and one central FPGA as one can see in Fig. 4.6. Each peripheral FPGA supports 48-channel Time-to-Digital Converter (TDC). Central FPGA unit is used to data transmission management [38, 106–108].

Each signal is splitted into four parts which are sampled independently in voltage domain as one can see in Fig. 4.3 by Multi-Voltage Threshold front-end based on FPGA unit. Signal threshold levels can be easily changed by user. Signal starting time as well as signal width are precisely measured. Due to the number of photomultipliers and signal sampling method 1536 TDC channels were required [106].

One master TRB module is responsible for synchronization as well as for controlling

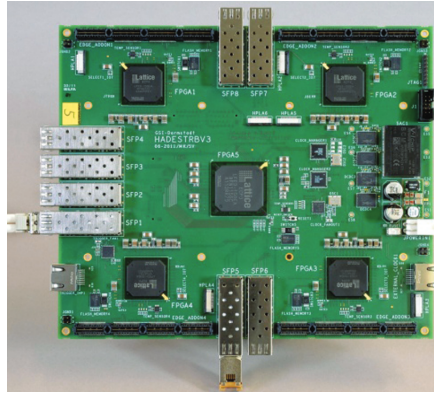


Figure 4.6: TRB unit with 4 peripheral FPGAs and one central chip. Figure adapted from [38].

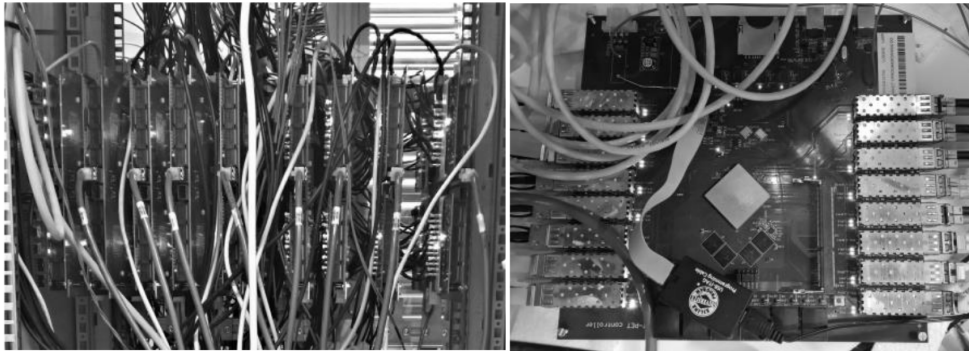


Figure 4.7: (left) A dedicated crate containing 1 master TRB and 8 TRB boards. (right) J-PET controller board. The 8 inputs on the left receive signals from 8 slave TRB boards while 8 outputs transmits data to the computer. Figures adapted from [106].

of the 8 TRB boards. Each slave board streams continuously collected data by 1 Gigabit Ethernet connection to the J-PET Controller, which processes and sends data to a computer (see Fig. 4.7). The main advantage of this system is continuous and real-time stream of data while the main disadvantage is a big size of the collected data.

4.4 J-PET Framework

Due to the J-PET detector geometry it was necessary to create extended or completely new data processing algorithms in comparison to standard PET devices. As it was mentioned earlier, the J-PET Framework, written in object-oriented C++ language, is based on the ROOT and the BOOST libraries. From the software point of view, J-PET Framework is divided into blocks which convert raw data to higher-level data structures in partial tasks as one can see in Fig. 4.8. This approach allows for relatively easy data analysis

even for users with low programming experience [32, 102, 109].

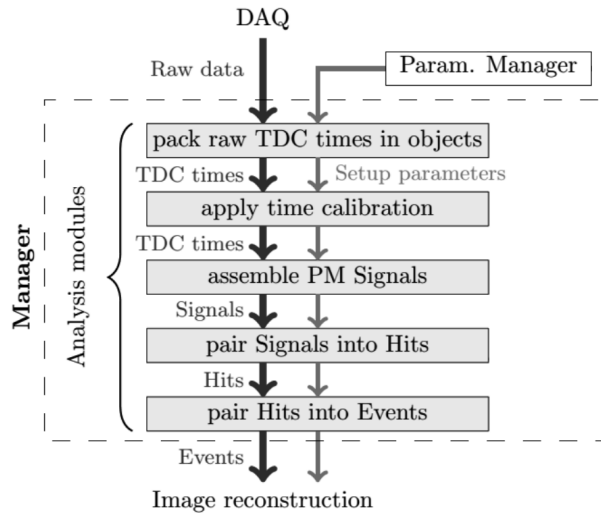


Figure 4.8: J-PET Framework structure. Hit corresponds to a single detected photon interaction while event denotes e.g. two hits coincidence. Abbreviation PM stands for photomultiplier. Figure adapted from [109].

Modules can be activated or deactivated by the user. Chosen modules are registered by the JPetManager. It allows for easy incorporation of new tasks, e.g. energy calibration or additional selection criteria, and easy data synchronization between them via the JPetWriter and the JPetReader. Output file from each step of analysis is separately saved to specific ROOT file. User has to specify also additional information such as input file, experimental setup description or custom options [32, 102, 109].

In the initial steps of analysis, each raw file from the J-PET DAQ is unpacked into ROOT file by a dedicated Unpacker software. As it was shown in Fig. 4.8, first analysis module transform this file to the structure used by the J-PET Framework. In the next step, photomultiplier signal is completed from times at specified thresholds and its properties are calculated. Signals from opposite photomultipliers are matched into hits. They contain information e.g. about arrival time, the position of interaction and time difference between two signals.

Experimental setup properties such as geometry, scintillators ID and dimensions as well as TRB channels are loaded from dedicated JSON file. In separate JSON file user can load custom settings including e.g. detector calibration filenames, time window used during signals matching and time window used during hits matching into events. Event definition is based on the user's choice. It can contain one, two or more hits in specific time window [102].

Chapter 5

Measurements performed with the J-PET scanner

Measurements were performed according to the instructions included in the NEMA norms. Conditions in the laboratory such as temperature and humidity were constantly monitored via dedicated control station presented in Fig. 5.1 and Fig. 5.2.

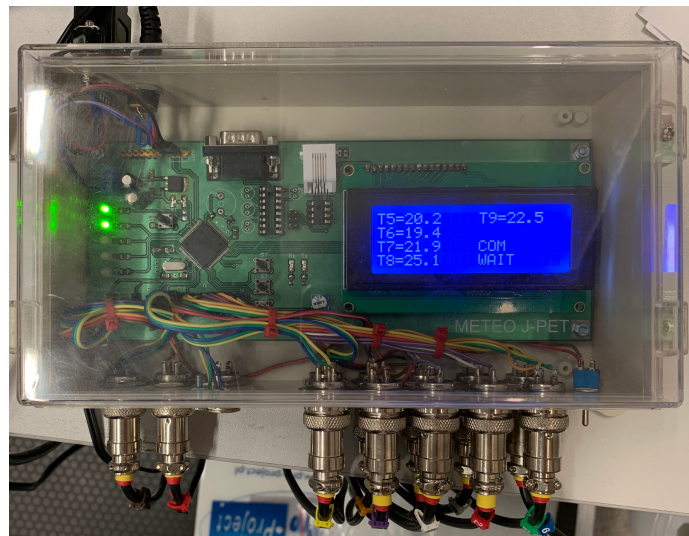


Figure 5.1: Temperature and humidity control station. Temperature sensors read-out is visible.

5.1 Radioactive sources

Two different types of radioactive sources were used: sodium point-like source and germanium line source. Germanium (^{68}Ge) was enclosed in a polyethylene tube (see Fig. 5.3).

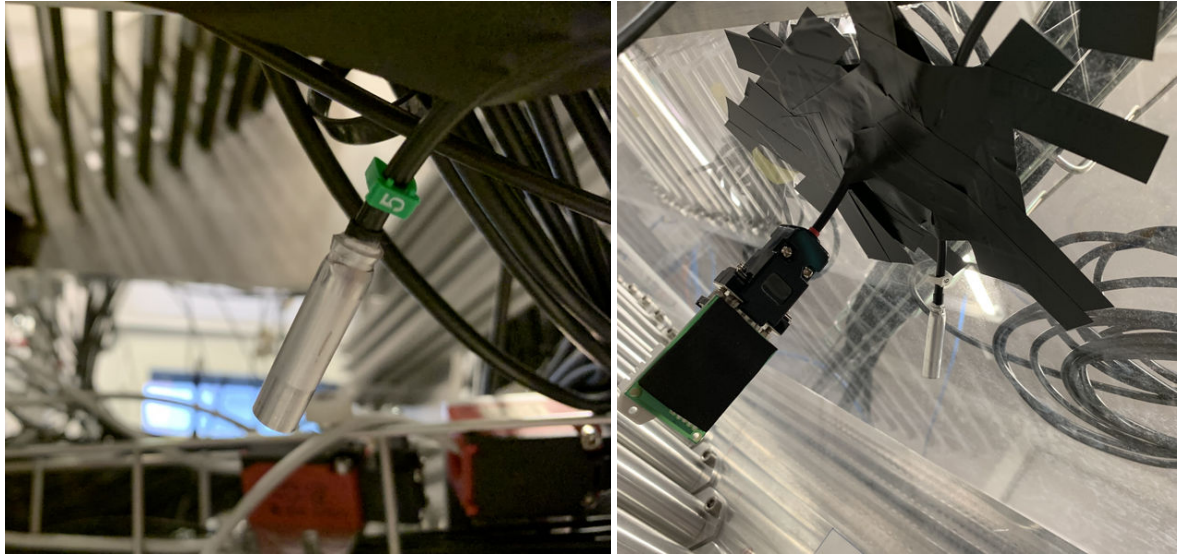


Figure 5.2: Temperature (left) and humidity (right) sensors. Temperature sensor in the photography is placed under the detector while humidity sensor is placed above the detector.

Its radiopurity was higher than 99%. Active length was equal to 500 mm while the outside diameter was equal to 2.54 mm fitting to the outside holes dimension of the PET Sensitivity Phantom and the PET Scatter Phantom. Its activity measured at the calibration day (13 December 2018) was equal to 24 MBq. The activity during measurements was in the range of 8715 kBq to 8050 kBq.



Figure 5.3: Germanium line source.

Due to big half-life equal to approximately 271 days, ^{68}Ge became competitive as a calibration source for daily quality control in PET scanners [110]. Gallium-68 (^{68}Ga), the daughter isotope of the Germanium-68 decay, has half-life equal to only 67.71 minutes and decays mostly through β^+ decay to stable ^{68}Zn as one can see in Fig 5.4. A disadvantage of this source with respect to ^{18}F is, however, the lower positron yield and higher positron range in the tissue due to higher mean energy, as one can see in Fig. 5.5 [111]. In case of ^{18}F , its half-life and efficient transportation between hospitals and radiopharma-

centuals production centers made it the best candidate for the clinical routine. However, the increase in ^{68}Ga use is visible in recent years [112].

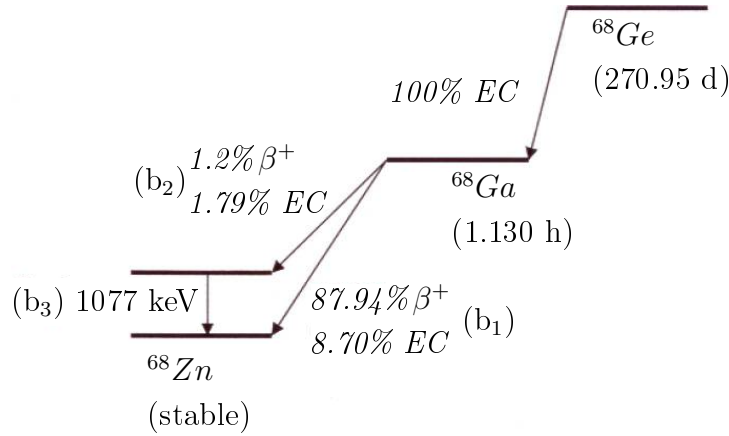


Figure 5.4: Decay scheme of ^{68}Ge . Figure adapted from [113].

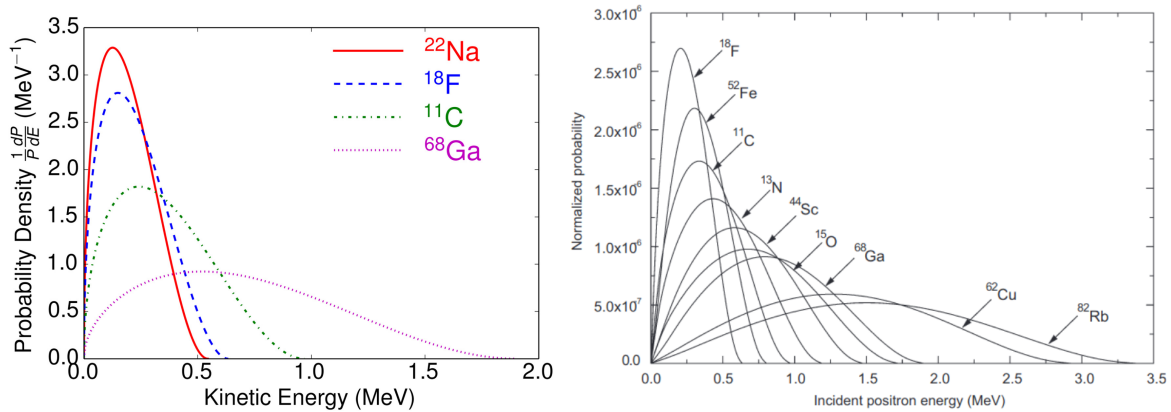


Figure 5.5: Energy distributions of positrons emitted from different radioisotopes. In case of ^{68}Ga , the maximum emission energy is equal to 1.899 MeV, while the mean energy is equal to 0.89 MeV. In comparison, the maximum emission energy for positrons from ^{18}F decay is equal to 0.634 MeV, while the mean energy is equal to 0.25 MeV. Figures adapted from [114, 115].

The other source used in the measurements was an ^{22}Na isotope in the shape of stainless steel cylinder with outside diameter equal to 4.72 mm and height equal to 5.72 mm (as one can see in Fig. 5.6). The diameter and height of active part inside capsule was respectively equal to 3.18 mm and to 1 mm. The source activity during measurements was in the range of 3903 kBq to 3816 kBq. This source was used only during spatial resolution measurements. Due to the long half-life (2.602 years) and decay type this source is valuable positron emitter as one can see in the right panel of Fig. 5.6. Positron

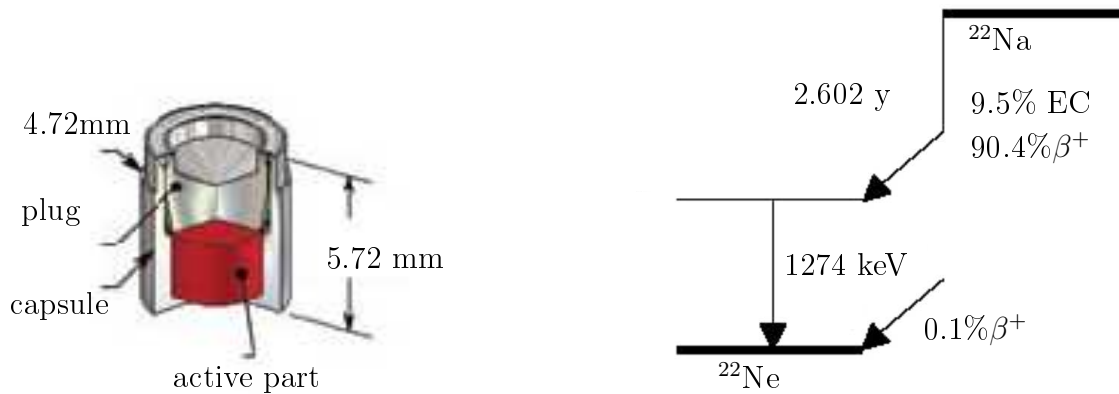


Figure 5.6: (left) Scheme of sodium source used during measurements. (right) ^{22}Na decays mostly through β^+ decay to the 1274 keV level of ^{22}Ne . Figures adapted from [116,117].

energy emission spectrum for ^{22}Na is only slightly different from the one of ^{18}F as one can see in Fig. 5.5, which makes ^{22}Na a good candidate to replace ^{18}F during measurements. Moreover, ^{22}Na is widely used by scientist to obtain spatial resolution of PET systems [118,119].

5.2 Measurements with the PET Scatter Phantom

The PET Scatter Phantom was described in details in Sec. 3.2. Before measurements phantom was assembled and prepared by drawing two crossed lines on both opposite edges as one can see in Fig. 5.8. According to these lines the phantom positioning along x - and y -axis was much easier. The phantom was positioned with its long axis overlapping with the z -axis of the J-PET scanner.

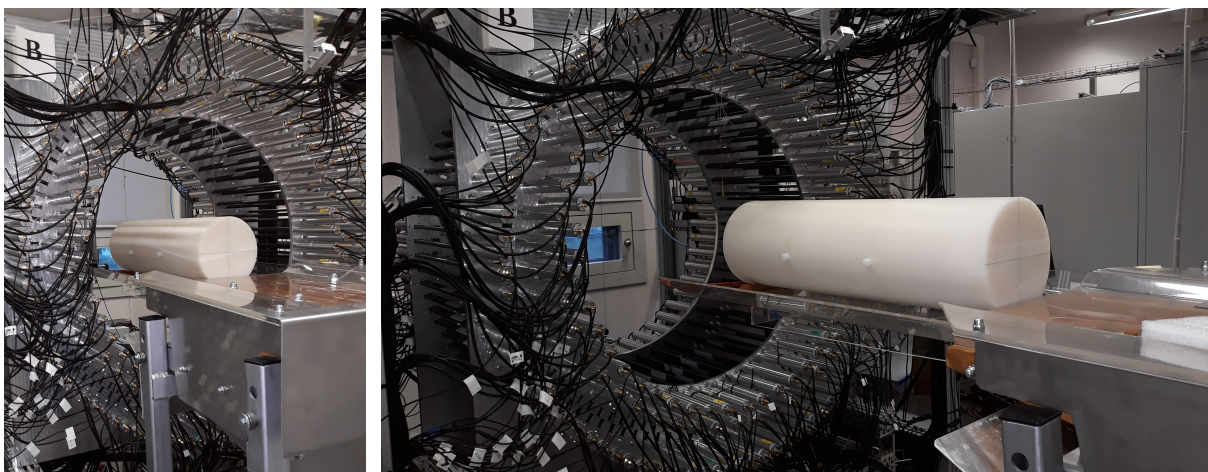


Figure 5.7: PET Scatter Phantom placed on a dedicated bed.

Phantom was placed on a dedicated bed as one can see in Fig. 5.7. A special thread construction exactly along y -axis was prepared from one side of the detector. In this case, thread was mounted on two opposite photomultipliers and tightened. To designate the x -axis another thread was mounted on the top photomultiplier from the first layer. Ballast was attached to the second end of this thread. These two crossed threads set the $(0,0)$ position in x and y coordinates (see Fig. 5.9). Phantom was moved as close as possible to threads.

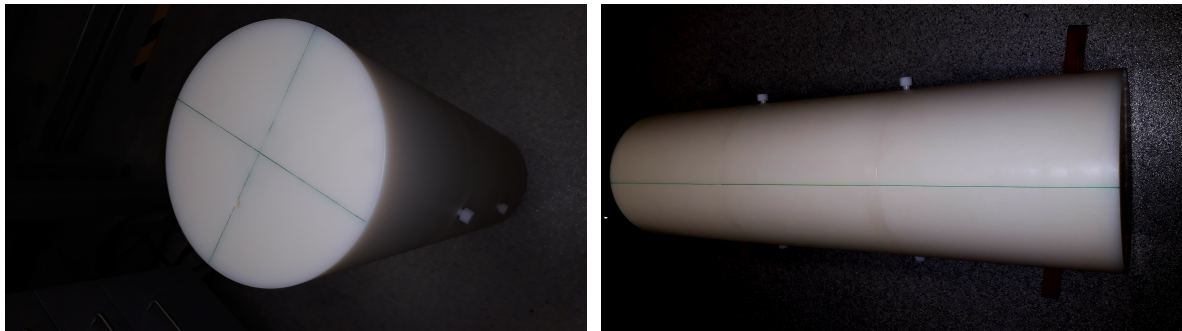


Figure 5.8: (left) PET Scatter Phantom with two crossed lines drawn on its surface. (right) Line connected two opposite edges of the phantom.

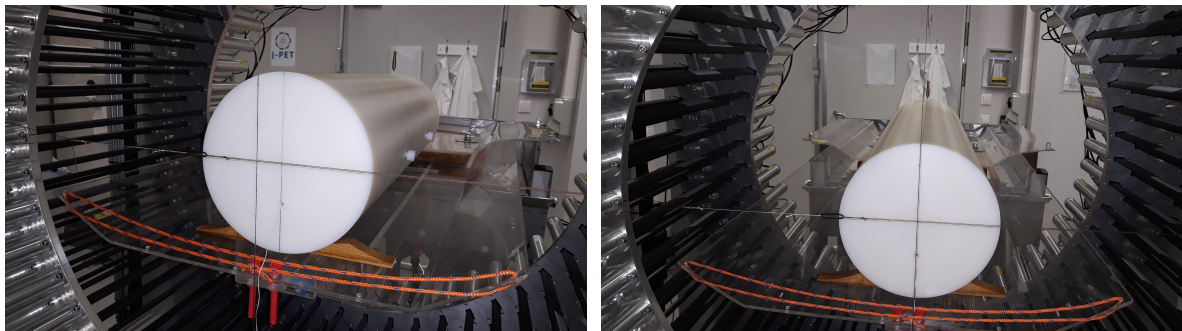


Figure 5.9: (left) Tightened thread along y -axis is visible. Photo was made from perspective to show the construction. (right) Two crossed threads set the center along x and y -axis. Lines on phantom edge covered these threads positions.

After centering phantom along x - and y -axis it was also positioned along z -axis. Due to the fact that the length of the PET Scatter Phantom is equal to 70 cm the germanium source was placed inside the phantom in a way that it covered the active part of the detector.

Before a long measurement a test was performed for 1 hour to produce control histograms such as position along x - and y -axis and along y - and z -axis. After confirmation of the correct positioning the measurement was performed for 19 hours.

5.3 Point-spread function measurements (with point-like source)

Dedicated plexi panel was prepared for these measurements due to the bed dimensions which did not allow for source placement at a position of 20 cm along the y -axis. Thickness of the panel was equal to $6.3 \text{ mm} \pm 0.1 \text{ mm}$ and it was measured by caliper. This shelf was supported by 3 aluminum laboratory lifts which were moved outside the panel as much as possible to avoid additional scatterings (see Fig. 5.11). Positions according to the NEMA norm were marked together with the $(0,0,0)$ position as one can see in Fig. 5.10.

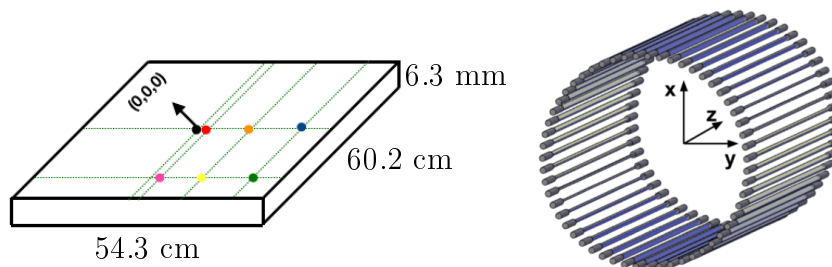


Figure 5.10: (right) Scheme of source positions marked on plexi: red: $(0,1,0)$, orange: $(0,10,0)$, blue: $(0,20,0)$, pink: $(0,1,-18.75)$, yellow: $(0,10,-18.75)$, green: $(0,20,-18.75)$. Figure is not to scale. (left) Axis orientation in the J-PET detector.

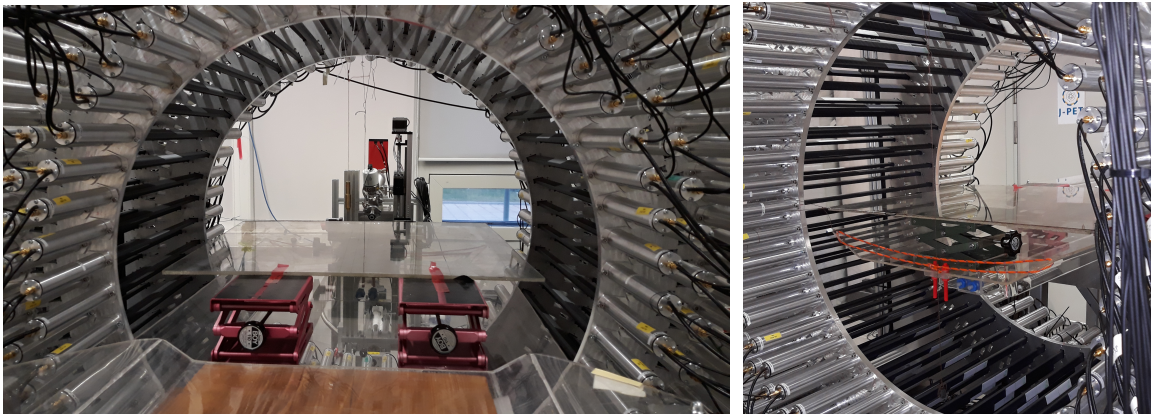


Figure 5.11: A dedicated plexi panel supported by 3 laboratory lifts (two pink and one green).

A short, 10 minutes test measurement was done for this additional position to confirm the correctness of source and plexi panel position. Then, an extra 1 hour measurement was also performed. For each position a test measurement for 1 minute was done. After checking the control histograms a 3 h long measurement was performed for each source position.

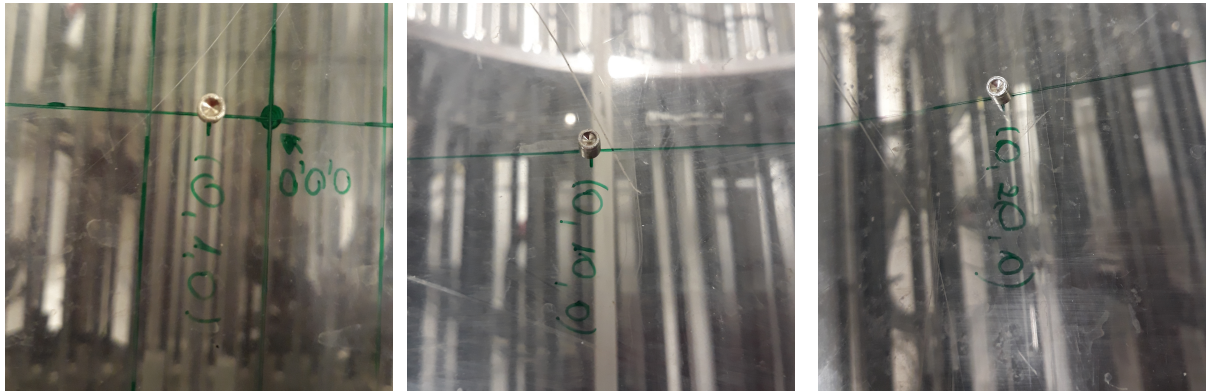


Figure 5.12: Sodium source placed in positions: $(0,1,0)$, $(0,10,0)$, $(0,20,0)$.

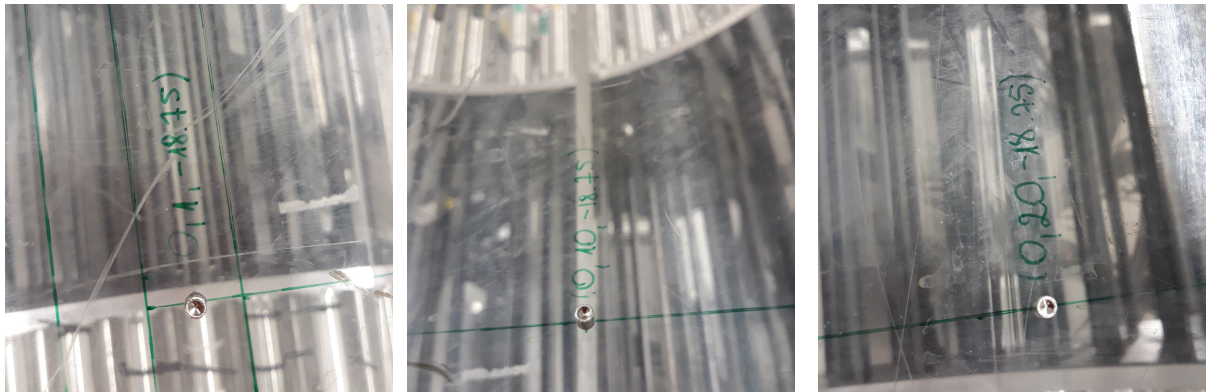
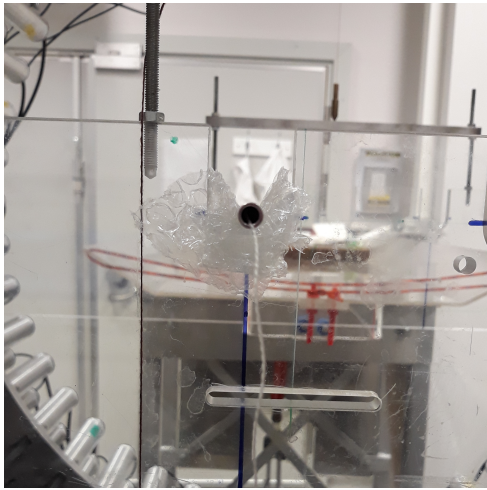


Figure 5.13: Sodium source placed in positions: $(0,1,-18.75)$, $(0,10,-18.75)$, $(0,20,-18.75)$.

5.4 Measurements using the PET Sensitivity Phantom

The PET Sensitivity Phantom was described in detail in Sec. 7.1. The innermost tube was not used during the experiment. Instead, a germanium source was used. Dedicated plexi panels were prepared to support the phantom inside the detector as one can see in Fig. 5.14. Due to phantom length and to avoid any additional artifacts in analysis, panels were mounted on the outer side of the detector (outside detector FOV). For each position and for each tube a test measurement was performed for 1 minute to confirm the correct positioning. The measurement was continued for at least 6 hours for each tube. PET Sensitivity Phantom was measured in position $(0,0)$ and $(0,10)$ [cm] in x and y coordinates. The source active part was covering the active part of scintillators.



(a) One sleeve.



(b) Five sleeves.

Figure 5.14: Photo documentation of sensitivity phantom positioning in position 10 cm from the center in y coordinate for two cases. The thickness of each sleeve is equal to 3.5 mm. First sleeve outside diameter is equal to 6.4 mm while outside diameter of the fifth sleeve is equal to 19.1 mm.

Chapter 6

Data preselection and detector calibration procedures

The time calibration is an important part of the PET operation routine. Timing resolution characterizes system ability to estimate the arrival time difference of gamma quanta measured in the coincidence and additionally provides the estimation of annihilation position [96]. Synchronization of all the components is usually done with long lived radioactive isotopes like ^{22}Na . Due to the J-PET detector geometry and construction a dedicated detector calibrations were required. Time and velocity calibrations are described in the next section.

Data post-processing techniques are similar between different manufacturers, but there is no official public document [120]. Due to basic information found in literature a dedicated data preselection conditions were developed and are presented in this chapter.

6.1 Time and velocity calibration

A novel method for time calibration of TOF-PET detectors was developed by members of the J-PET group [121] and it is based on the fact that some radioisotopes after β^+ decay and positron emission, e.g. ^{22}Na , can transform into nucleus in excited state and subsequently deexcite with photon emission. Created photon can be distinguished from annihilation photons based on its energy.

To perform this calibration procedure, ^{22}Na source has to be placed in the center of the J-PET detector. It simplifies calculations of photon emission time. To obtain this parameter a time of photon registration in a given module and the distance between this module and source are used. It also has to be mentioned that only such events are taken into account which contain one photon originating from nucleus deexcitation and one annihilation photon. For this kind of events the distribution of time difference

between annihilation and deexcitation is calculated and the mean value of this distribution defines the time offsets between different detectors pairs. Difference between time offsets (miscalibration measure) can be used as a correction parameter for a given module pair. Detector is calibrated when the values of all miscalibration measures are negligible.

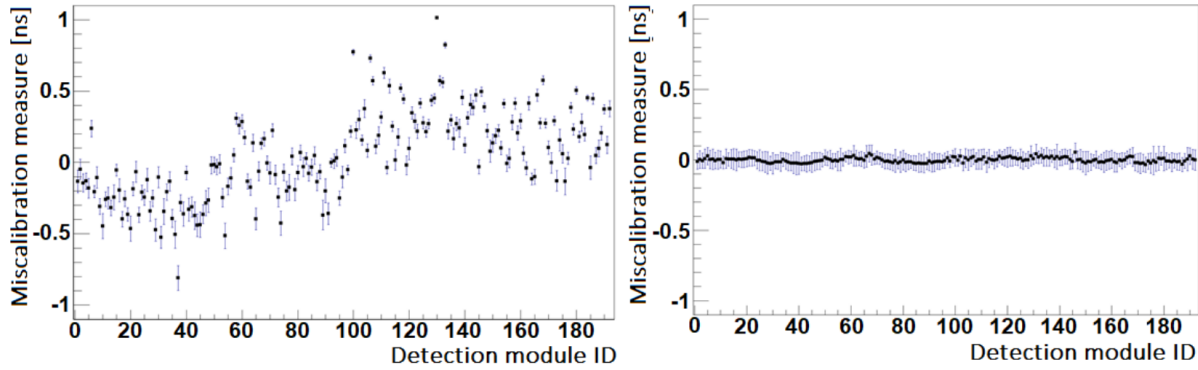


Figure 6.1: Miscalibration measure before (left) and after (right) calibration procedure. Figure adapted from [121].

Due to the J-PET design and scintillator type place of interaction of gamma quantum is calculated from formula 4.1. Effective velocity of light inside the scintillator depends on its refractive index, cross section, etc., and moreover, it influences the difference between times registered by two opposite photomultipliers. The average value of light velocity inside EJ-230 was calculated from measurements using a collimated radioactive source and is equal to about $12 \frac{\text{cm}}{\text{ns}}$ [104]. Due to slight fluctuations between parameters characterizing each detector it was necessary to determine effective light velocity for each scintillator separately. In this calibration it was assumed that the straight line, parallel to the z -axis of a scintillator, is the shortest distance between the place of interaction and photomultiplier. The main advantage of this calibration is the possibility of time calibration at the same time.

Effective length (active part) of a scintillator is indispensable in calculations of effective light velocity as one can see in the following equation (based on formula 4.1):

$$l_{eff} = \frac{t_{rightEdge} - t_{leftEdge}}{2} \cdot V_{eff} \quad (6.1)$$

where: $t_{rightEdge}$ and $t_{leftEdge}$ are times registered at both ends of a detection module, l_{eff} and V_{eff} stand for effective length and velocity. In the J-PET, the scintillator length is equal to 50 cm and this value was taken as a reference parameter in the further analysis. Tested Effective Length Constants were in range from 46 to 52 cm with 1 cm step. Two calibration constants sets were created: one set for Effective Length Constant equal to the reference 50 cm and second one was created for a arbitrary taken value from

Effective Lengths Constants. It was found that there is a quadratic-like dependence between effective lengths and mean difference between calibration constants sets with extreme equal to ~ 50 cm. The exact value of effective length of scintillator from fit and times of signal registration on both ends were used to obtain the effective light velocity for each module separately.

6.2 Data selection criteria

First data selection criterion is the condition that events with exactly two hits in coincidence time window are taken into further analysis. Events with one, three or more hits are rejected. Size of coincidence time window is related to the detector dimensions. This window should contain all possible situations, where annihilation take place inside the J-PET detector and exactly two gamma are registered in coincidence mode by two opposite detection modules. In the most extreme case, where annihilation occurred close to a scintillator from first layer and mounting plate, one gamma quantum can be detected by a scintillator nearest to the annihilation point and second one can be detected by scintillator from third layer and in position close to opposite mounting plate as one can see in Fig. 6.2.

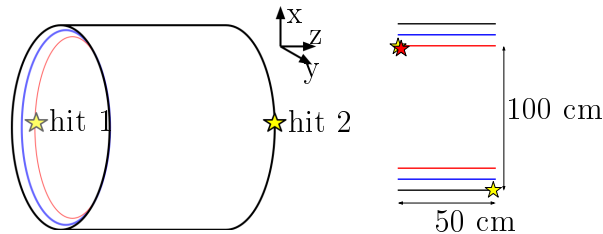


Figure 6.2: (left) Schematic representation of two hits detected by two scintillators from first (red) and third (black) layer respectively. Points of interactions are denoted as yellow stars. (right) Distance between scintillator's center from first and third layer is equal to 100 cm.

Distance connecting annihilation point and opposite hit, calculated using the Pythagorean theorem, is equal to ~ 112 cm. Taking into account speed of light, gamma quantum needs less than 4 ns to travel distance from the annihilation point to scintillator from third layer in opposite part of the detection setup. Coincidence time window equal to 4 ns is overestimated but includes all possible cases for two hits events.

Effect of this selection criterion on data from measurement with ^{22}Na point source placed in the detector center is shown in Fig. 6.4 and Fig. 6.5. To obtain this type of histograms a middle point of LOR is calculated based on the equation:

$$LOR_{middle} = \frac{t_A + t_B}{2}, \quad (6.2)$$

where t_A and t_B stand for times of hits interaction with detection modules. The shift from LOR middle point to the annihilation point is calculated based on equation 4.3 for each axis separately and these values are loaded into histograms of annihilation point position. Visible background partially comes from not rejected scatterings.

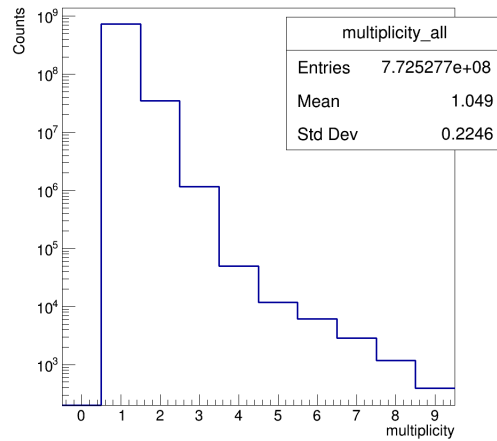


Figure 6.3: Number of hits in event in a given time window in logarithmic scale . In this case two hits events represent only $\sim 4.6\%$ of total number of hits in the 4 ns time window.

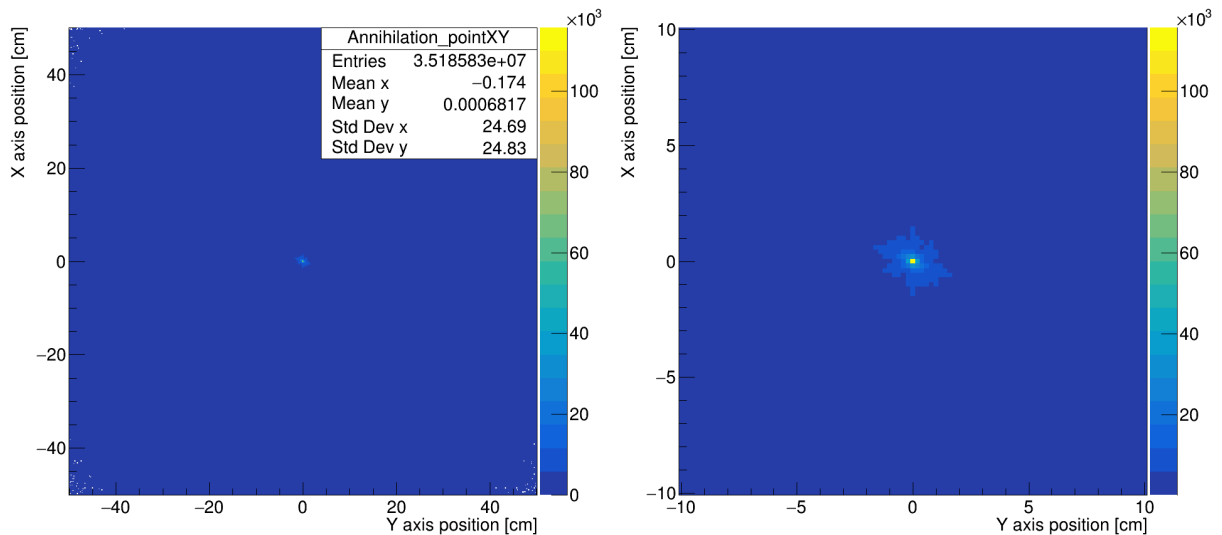


Figure 6.4: (left) Control histogram of annihilation point after two hits selection criterion. Histograms drawn for xy plane. (right) Control histogram shown within the range of $(-10,10)$ cm.

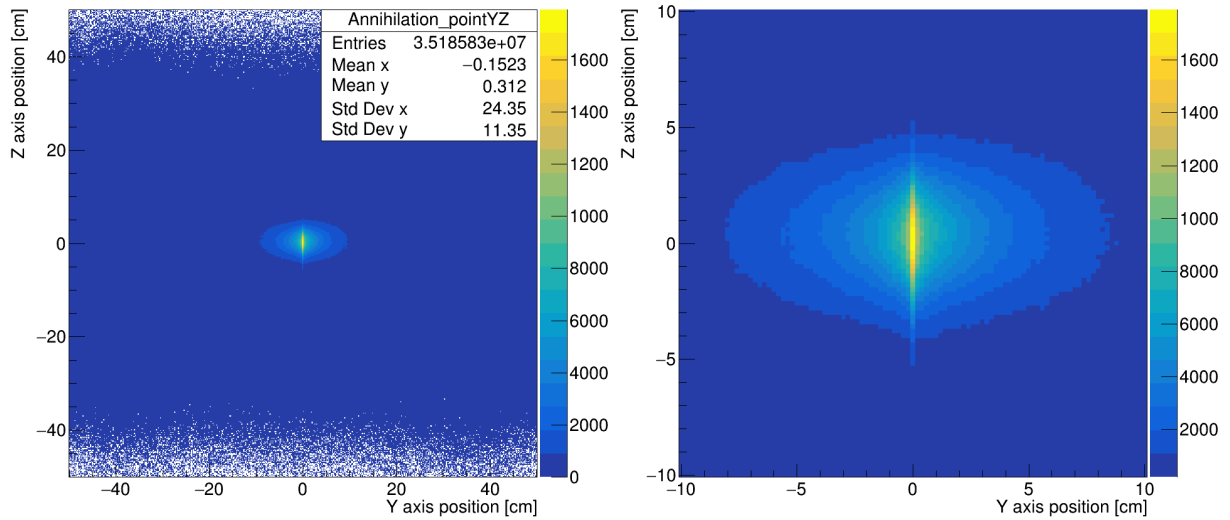


Figure 6.5: (left) Control histogram of annihilation point after two hits selection criterion. Histograms drawn for yz plane. (right) Control histogram shown within the range of $(-10,10)$ cm.

The next selection criterion constitutes series of geometric cuts. The first of them assumes that z coordinate of annihilation position as well as the possible points of interaction of gamma quantum with scintillator should be in range ± 23 cm. This condition comes from design of the J-PET detector. Scintillators are connected with photomultipliers placed on the outer side of mounting plates, so it was necessary to pass the scintillators through dedicated holes as one can see in Fig. 6.6.



Figure 6.6: View of mounting plate with visible holes and photomultiplier tubes (left photo) as well as with scintillators (right photo). Courtesy of M. Glapska-Moskal and the J-PET group.

Distance between inner edges of mounting plates and at the same time the real length of each scintillator taken into further analysis is equal to 46.3 cm. Thus, it was necessary

to narrow the range of possible annihilation position and interaction position with scintillator along the z -axis. This is schematically showed in Fig. 6.7. This selection criterion allows also for avoiding of some gamma scatterings on aluminum mounting plates.

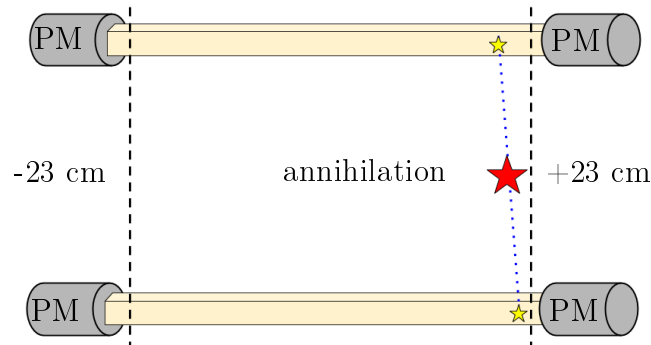


Figure 6.7: Schematic representation of the pair of detection modules of the J-PET tomograph which registered gamma quanta from an annihilation (red star). Only the points of interaction (yellow stars) with the reconstructed z position in the range $(-23, 23)$ cm are accepted.

In commercial PET scanners bore size changes between different manufacturers, but the real field-of-view can be smaller, e.g. in the Celesteion PureVision Edition PET/CT the bore size is equal to 88 cm while transaxial field-of-view is equal to 70 cm [122]. Smaller transaxial FOV equal to 55 cm is characterizing the Discovery LS Advance NXi scanner [123]. In the case of the J-PET detector a cylindrical volume with diameter equal to 50 cm was selected for analysis as one can see in Fig. 6.8.

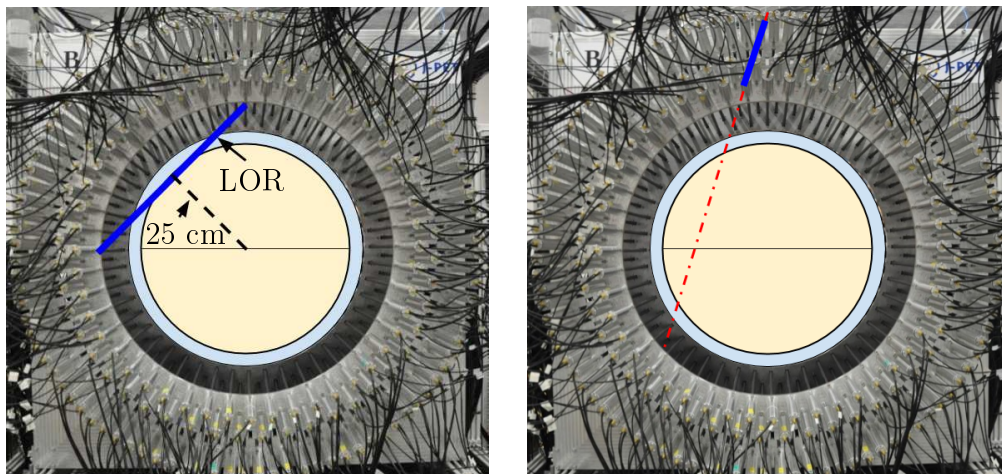


Figure 6.8: (left) Example of a well reconstructed event. Yellow circle - cylinder with radius equal to 25 cm. Figure not to scale. (right) Example of a badly reconstructed event.

The distance between line-of-response and the cylinder center has to be smaller than 25 cm in x and y coordinates. Only lines which crossed the cylinder are taken into account. This method is not perfect due to situation visible in the right panel of Fig. 6.8. In case of scattering between two scintillators located close to each other a false line crossed the cylindrical area was reconstructed and it is taken into further analysis. Result of this effect is visible in Fig. 6.9. Visible structures appear on histogram for xy plane. This effect comes from the fact that there is no additional data reconstruction algorithm used [42, 124]. There is no system matrix applied and therefore system sensitivity is not taken into account. On the other hand, the amount of survived events has decreased from 80.9% to 38.7% of total number of two hits events. Background was significantly reduced.

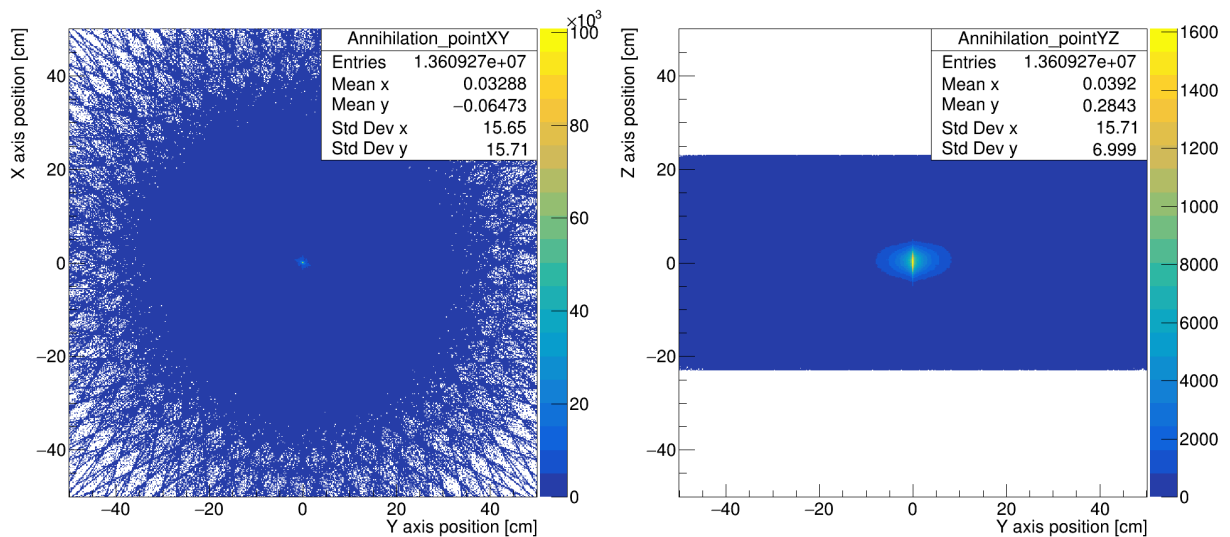


Figure 6.9: Control histograms of annihilation points after selection condition related to distance between LOR and detector center. Only $\sim 38.7\%$ of total number of two hits events survive this data cut.

To avoid scenario presented in the right panel of Fig. 6.8, another geometrical cut was applied to the data. It is related to the angular position of the scintillators on the xy plane. It was assumed that only events for which the relative angle between the two detection modules fired is greater than 20 degrees were accepted for further analysis. As one can see in Fig. 6.10 after all previous cuts there are still some scatterings occurring inside detector (peaks below 20°). By putting the above condition all these cases are rejected. It is worth noting that this angle cannot be too large to not discard annihilations that occurred close to scintillators, e.g. in measurements for spatial resolution in position $(0, 1, -18.75)$ [cm].

Results from simulations with the PET Scatter Phantom published in [125] showed that all the cases of true coincidences lie in a region well-defined by hits times and angle differences. Simulations were performed assuming the detector consisting of a single layer

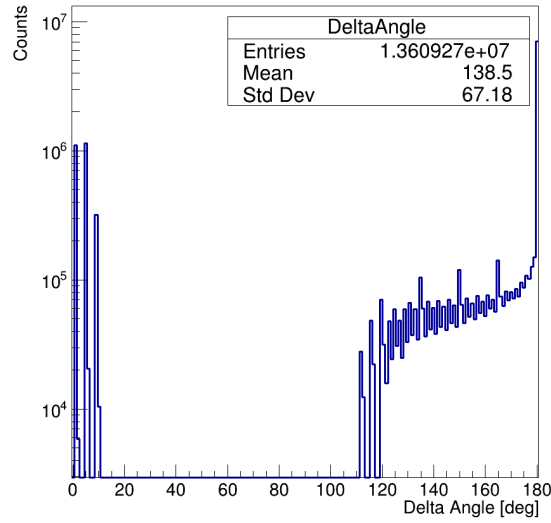


Figure 6.10: Angles difference between two scintillators registering gamma quanta in logarithmic scale. Scatterings between strips closed to each other are visible below 20° .

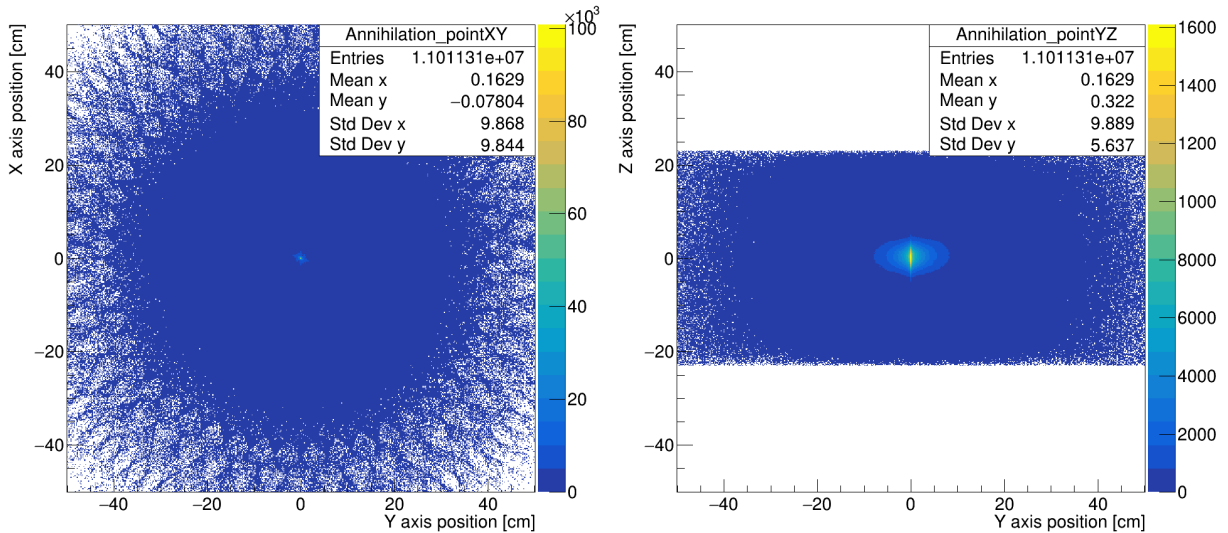


Figure 6.11: Control histograms of annihilation points after selection condition related to the angle difference between two modules which registered hits. Around 31.3% of total number of two hits events survive this data cut.

with diameter equal to 85 cm. Outcome of these simulations allowed to find additional data selection criterion. To define a signal region the angle difference between two gamma quanta should fulfill the following inequality:

$$\Delta_{angle} > (180 - 80 \cdot \sqrt{\frac{1 - \Delta_{time}^2}{ellipse_{parameter}^2}}) \quad (6.3)$$

The $ellipse_{parameter}$ is equal to 2.2, while Δ_{angle} and Δ_{time} stand for the angle and time difference, respectively. Application of this criterion allowed for elimination of some part of background and wrongly reconstructed events, as presented in Fig. 6.12 and Fig. 6.13.

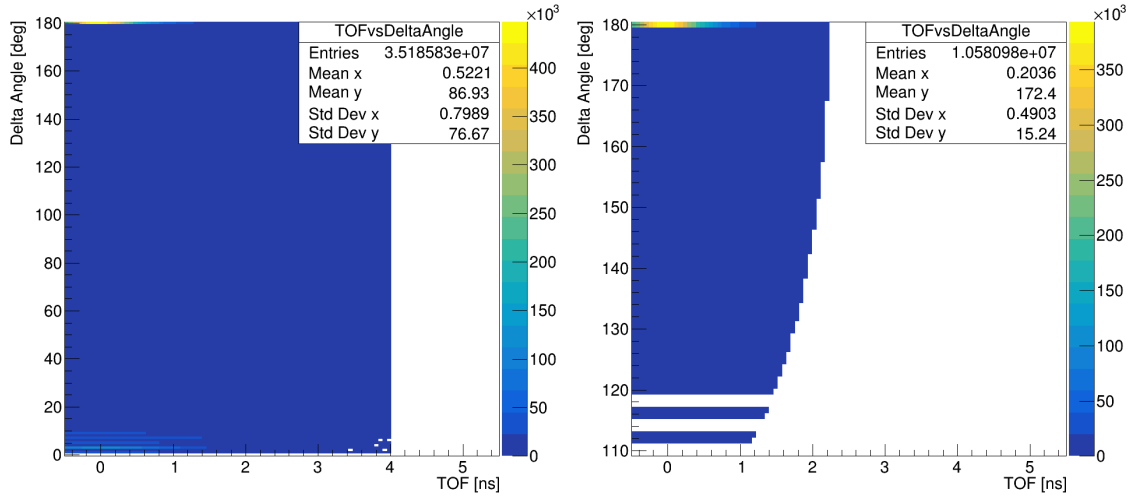


Figure 6.12: Control histograms of hits registration time difference (TOF) versus hits angle difference after two hits in event condition (right) and after criterion mentioned in equation 6.3. Almost only back-to-back events survived this selection cut.

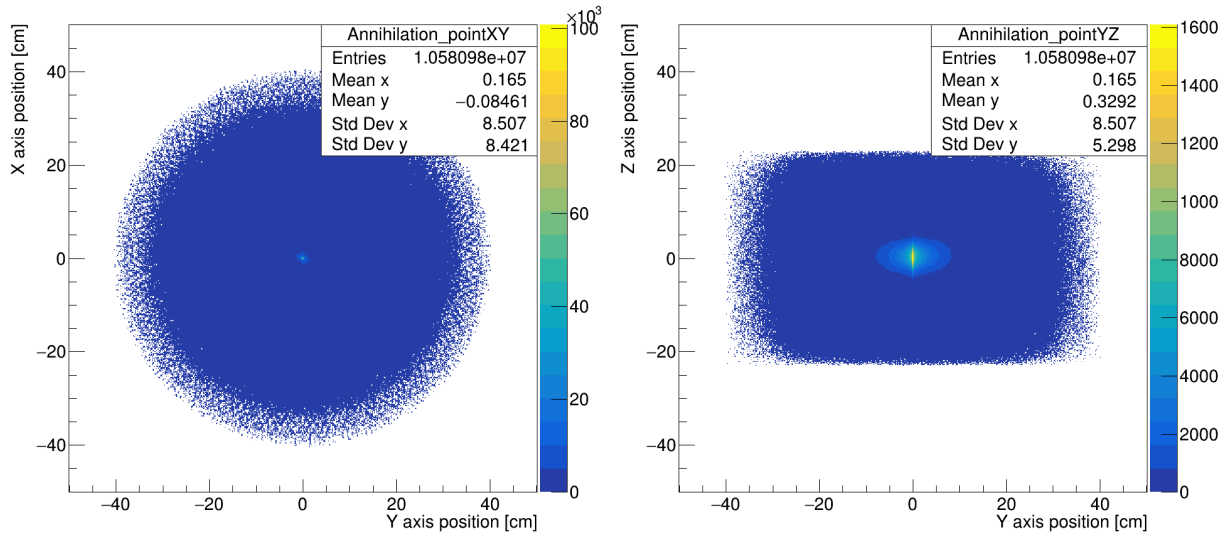


Figure 6.13: Control histograms of annihilation points after selection condition based on the relation of hits time and angle differences. Less than 30.1% of total number of two hits events survive this data cut.

6.3 Energy calibration

All photomultipliers provided by Hamamatsu and mounted in the J-PET prototype are the same type, but gain calculated as:

$$gain = \frac{\text{anode luminous sensitivity}}{\text{cathode luminous sensitivity}} \quad (6.4)$$

varies among them from $1.24 \cdot 10^6$ to even $1.89 \cdot 10^6$ based on documentation provided by the manufacturer during order. Due to these divergent values it was necessary to obtain effective uniformity of the gain between different photomultipliers.

Method of the unification of the photomultipliers gains is based on the relation between energy deposition in a scintillator and the time-over-threshold (TOT) measurement [126]. Photon energy loss, due to interaction via Compton scattering inside the scintillator, can be determined by measurement of a signal width at a given threshold, but this dependence is not linear and can be described by the following relation:

$$TOT = A_0 - A_1 \cdot A_2^{E_{dep}}, \quad (6.5)$$

where A_0 is equal to 42.96 ns, while A_1 and A_2 are equal to 53.43 ns and 0.997 keV^{-1} , respectively [126]. E_{dep} stands for energy deposition.

To perform this calibration procedure data from measurement with the PET Sensitivity Phantom with 5 sleeves in position (0,0) cm was chosen. The main advantage of this type of measurement is the fact that all the scintillators along their entire length are sensitive to incoming photons at the same time. Before the measurement the mean free path in air and aluminum of a positron emitted by the ^{68}Ge source was estimated based on the equation:

$$r = 0.412 \cdot E^{(1.27 - 0.0954 \cdot \ln E)} \quad (6.6)$$

$$X = \frac{r}{\rho} \quad (6.7)$$

where: r - the positron range [g/cm^2], E - positron energy [MeV], X - positron mean free path [cm] and ρ - material density [127]. Calculations were done for two environments: air ($\rho = 0.0013 \text{ [g}/\text{cm}^3]$) and aluminum ($\rho = 2.702 \text{ [g}/\text{cm}^3]$). Results one can find in Tab. 6.1.

Thickness of each aluminum tube in the PET Sensitivity Phantom is equal to 2.5 mm. Based on results presented in Tab. 6.1 it seems that only two aluminum tubes would have been sufficient to stop positrons close to emission point. Moreover, attenuation of gamma particles in aluminum can be easily calculated from the equation:

$$I = I_0 \cdot e^{-\mu_m \cdot t_d} \quad (6.8)$$

Table 6.1: Positron mean free path calculated for air and aluminum.

Maximum positron energy [MeV]	Average positron energy [MeV]	Maximum range [cm]		Average range [cm]	
		Air	Aluminum	Air	Aluminum
1.899	0.89	688.08	0.33	273	0.13

where: I and I_0 means attenuated and unattenuated beam intensities, while μ_m and t_d stands respectively for mass attenuation coefficient (cm^2/g) and absorber density thickness (g/cm^2) [128]. Value of the mass attenuation coefficient for 511-keV gamma particles is equal to $0.0840 \text{ cm}^2/\text{g}$ [129]. As one can see, based on results in Tab. 6.2, attenuation for five sleeves is $\sim 7\%$ larger than for two sleeves and thus, it was assumed that in this kind of analysis there is no significant difference between 2 and 5 sleeves.

Table 6.2: Attenuation of 511-keV gamma quanta in aluminum for different number of sleeves of the PET Sensitivity Phantom. For uncovered source it was assumed that $I/I_0=1$.

Number of sleeves	Total thickness [mm]	I/I_0
1	1.25	0.97
2	2.5	0.94
3	3.75	0.92
4	5	0.89
5	6.25	0.87

Data from measurement with 5 sleeves, which was performed for 6 hours continuously, were preselected according to all steps described in Sec. 6.2. At the level of events with two hits registered in the 4 ns time window, a TOT value for each hit was calculated as:

$$TOT = \Sigma_{PMT=A,B} \Sigma_{Thr_{1-4}} TOT_{PMT,Thr} \quad (6.9)$$

where $TOT_{PMT,Thr}$ means sum of the TOT values measured on all the four thresholds at both ends of a given scintillator denoted in Eq. 6.9 as A and B side, respectively. Schematic representation explaining the sampling method can be found in Fig. 6.14. In the next step each TOT value for each hit was converted to the energy deposition based on Eq. 6.5 as:

$$E_{dep} = \frac{\log(A_0 - TOT) - \log A_1}{\log A_2} \quad (6.10)$$

Histogram of TOT and energy deposition for an exemplary scintillator after selection criterion for two hits in event can be found in Fig. 6.15. Summary histogram of all

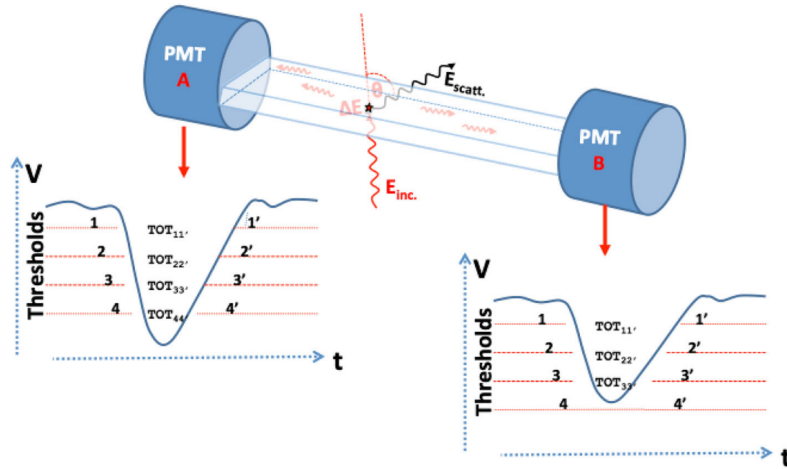


Figure 6.14: Signals from both sides of a scintillator are sampled at four thresholds for leading and trailing edge in voltage domain. E_{inc} and $E_{scatt.}$ stand respectively for energy of incoming and scattered photon. Figure adapted from [126].

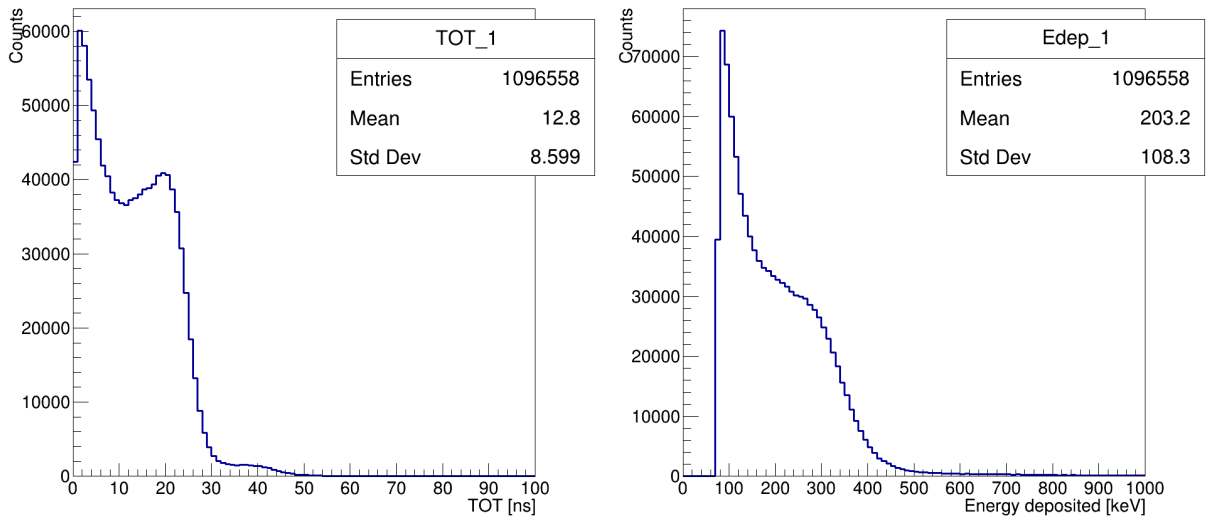


Figure 6.15: Histogram of TOT (left) and energy deposition (right) for the scintillator with ID=1 from the innermost layer. Histograms drawn after two hits in event selection criterion. Bin width on TOT histogram is equal to 1 ns, while bin width on energy histogram is equal to 10 keV.

the TOT values and energy depositions for all scintillators are presented in Fig. 6.16. This procedure of TOT \rightarrow energy deposition conversion for each hit was repeated for all the selection criteria to remove unnecessary background and wrongly reconstructed events. One can find the same histograms as in Fig. 6.15 after all the selection criteria in Fig. 6.17. Bin width on TOT histogram is equal to 1 ns, while bin width on energy

histogram is equal to 10 keV.

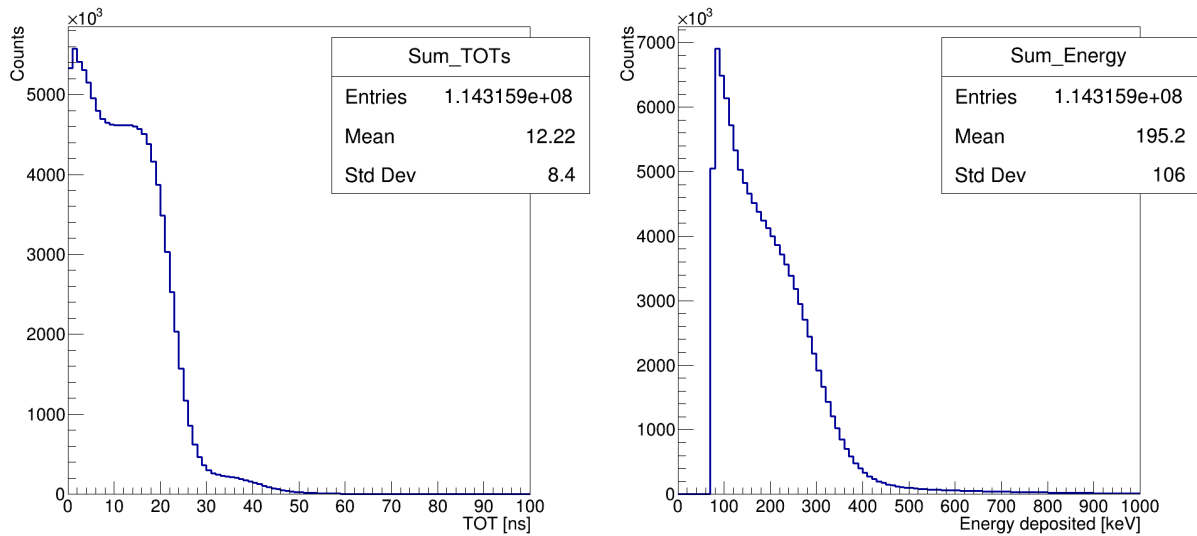


Figure 6.16: Summary histograms of TOT values (left) and energy depositions (right) for all scintillators. Histograms drawn after two hits in event selection criterion.

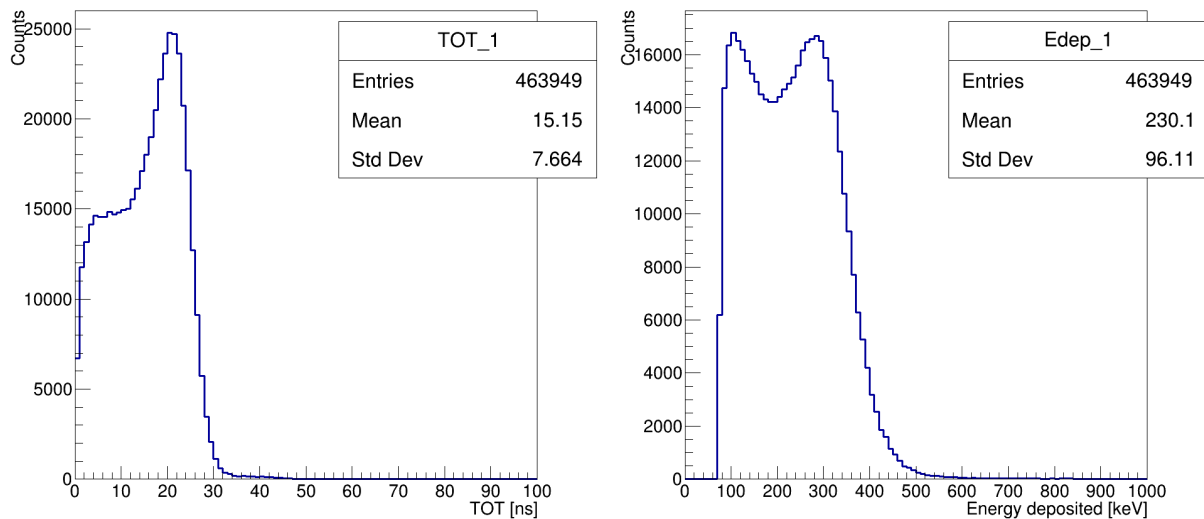


Figure 6.17: Histogram of TOT (left) and energy deposition (right) for scintillator with ID=1 from the innermost layer. Histograms drawn after all selection criteria described in Sec. 6.2.

Histograms of energy depositions were analyzed for all scintillators of the J-PET detector. In the next step, a Compton edge estimation was performed. To do this procedure, each histogram was recomputed and smoothed with the moving average (MA). Average

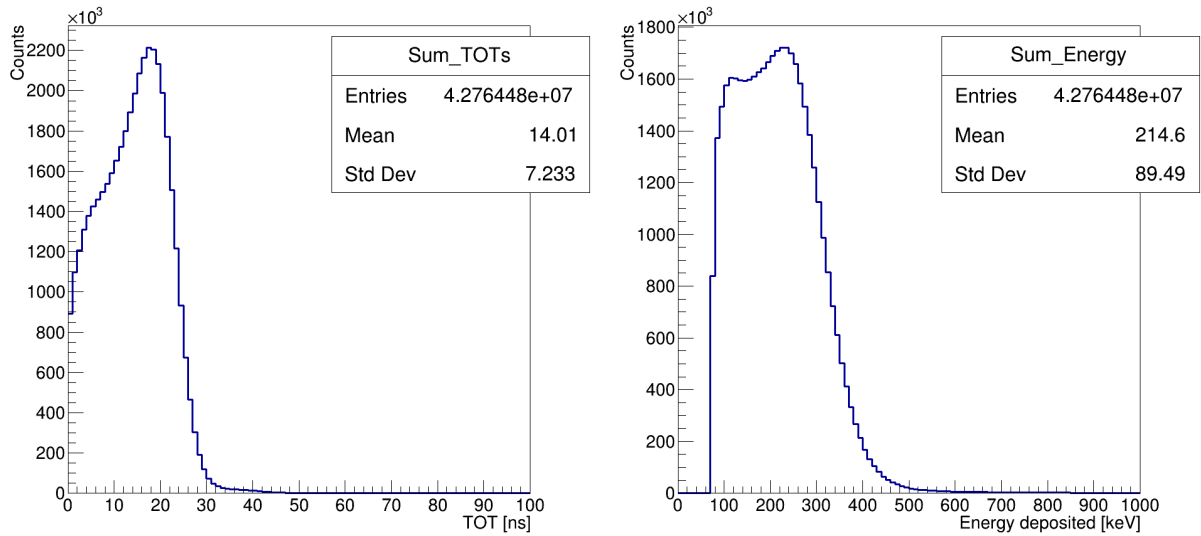


Figure 6.18: Summary histograms of TOT values (left) and energy depositions (right) for all scintillators. Histograms drawn after all selection criteria described in Sec. 6.2.

count value of i -th bin was calculated using formula:

$$\overline{counts}_i = \frac{1}{3} \sum_{j=i-2}^i counts_j \quad (6.11)$$

This approach was repeated bin by bin starting from the third bin. Simple moving mean allows for histogram smoothing which is important in the case of small statistic. Uncertainty of moving average was calculated from the error propagation law.

Next, a first derivative of the TOT/energy distribution was calculated for each smoothed histogram. Results for an exemplary histogram are presented in Fig. 6.19. Minimum of the first derivative is the histogram inflection point. A parabola in the range of 10% around the minimum was fitted which enabled estimation of the Compton edge value.

To equalize the response of all the detection modules, Compton edge value for all the scintillators should be rescaled to the value of 340 keV, which is the maximum energy deposition in scintillator via Compton scattering for not scattered in patient body gamma quanta with 511 keV energy. Therefore, Compton edge values obtained calculating the first derivative were divided by 340 keV and those results were taken as the rescale factors for all histograms. In the next step, those correction coefficients were applied to the data. TOT of each hit was converted to the energy deposition divided by the corresponding rescale factor. Histograms of corrected energy depositions can be found in Fig. 6.21. Position of the Compton edge for all scintillators are shown in Fig. 6.22.

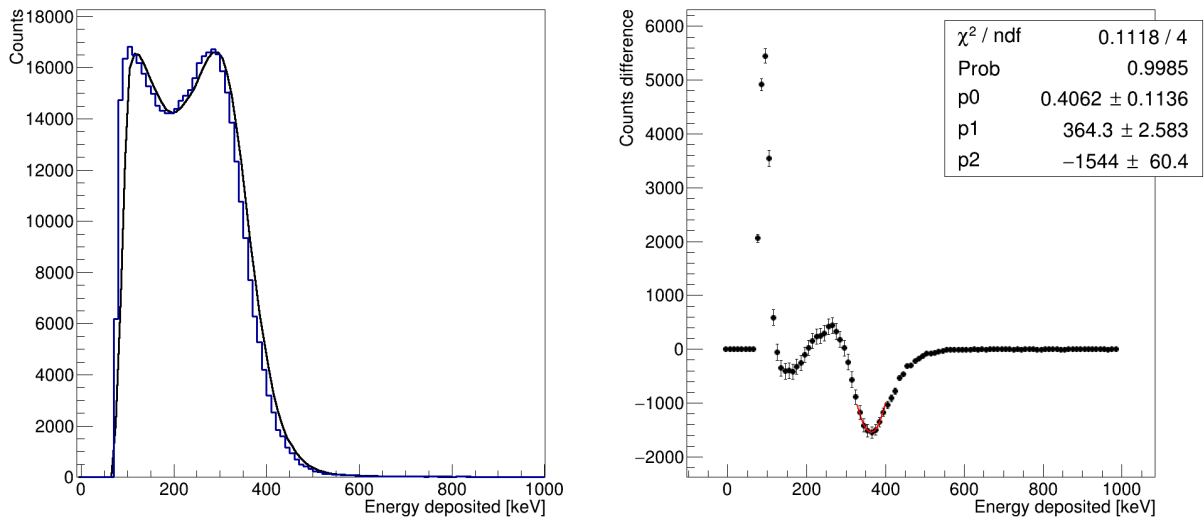


Figure 6.19: (left) Histogram of energy deposition for scintillator with ID=1 (first one from the innermost layer). Blue line - original histogram, black line - histogram smoothed with simple moving average. (right) First derivative of the smoothed histogram. Error bars were calculated as sum of uncertainties of two consecutive points from smoothed histogram.

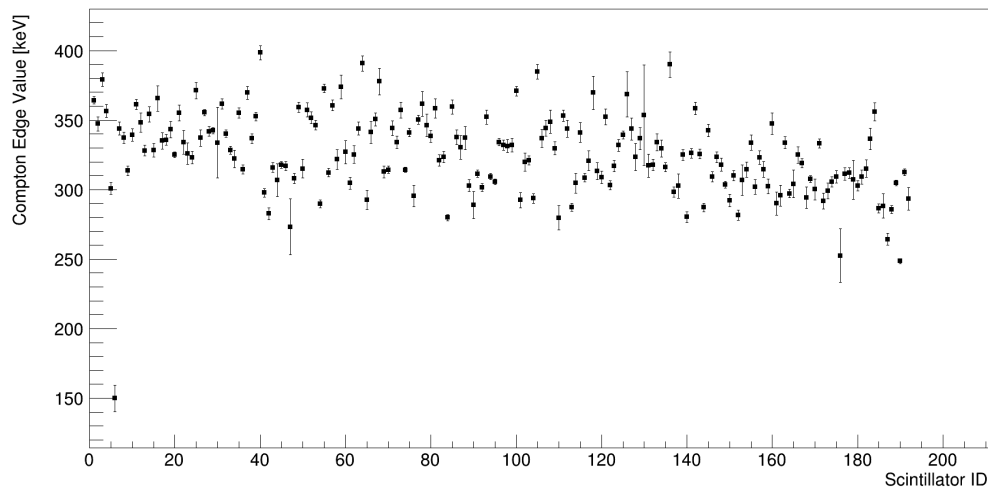


Figure 6.20: Value of Compton edge for all scintillators of the J-PET detector. Value close to 150 keV was obtained for scintillator with ID=6 and comes from badly working channel on an electronic board.

In the next stage of the data analysis a check if there exists any dependence between energy deposition and position of interaction of gamma quanta along scintillators was

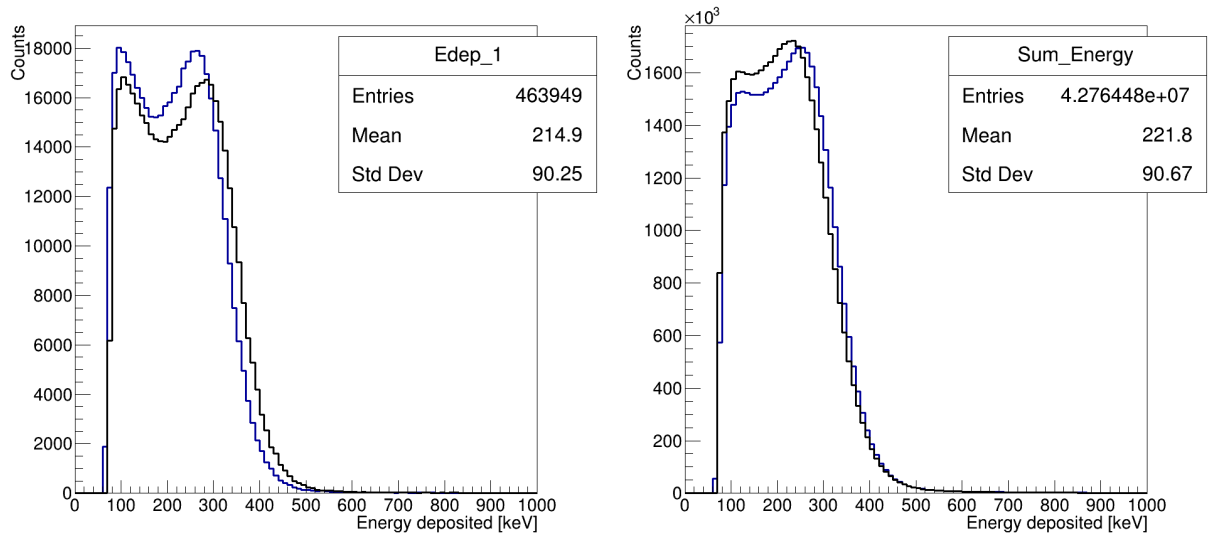


Figure 6.21: (left) Histogram of energy deposition for scintillator with ID=1. (right) Summary histogram of energy depositions for all the scintillators. Black line - histogram before correction, blue line - histogram after correction.

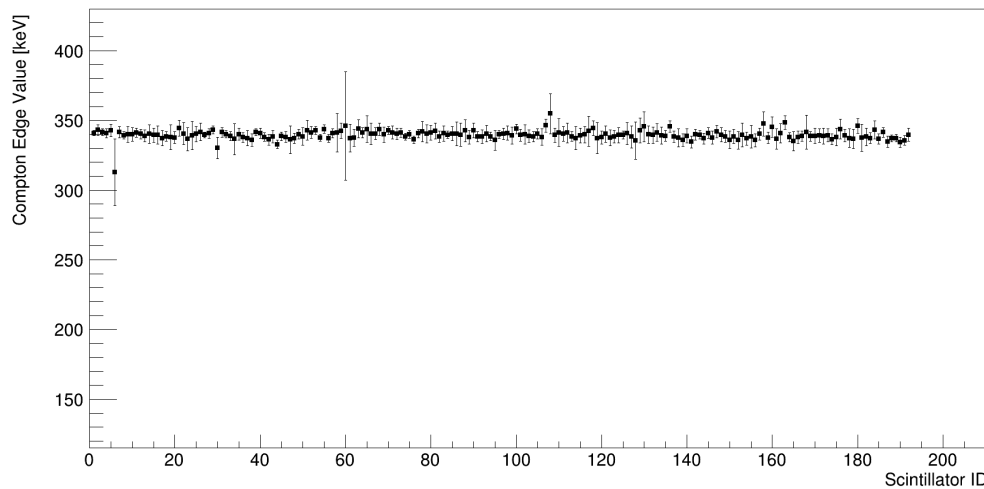


Figure 6.22: Value of Compton egde for all scintillators of the J-PET detector after correction.

performed. To check this possibility each scintillator was divided to 17 areas in the range of $\langle -20, +20 \rangle$ [cm] (17 points every 2.5 cm) as presented in Fig. 6.23. For each interaction point from the list a dedicated histogram was created.

Due to the small statistic for a given position in a single scintillator we have considered for each position a joint distribution of the energy depositions due to similar performance

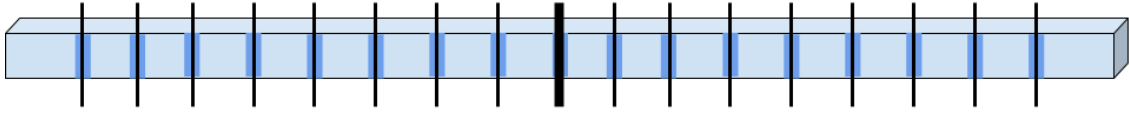


Figure 6.23: Scintillator divided into 17 areas. Width of each area is equal to 1 cm (marked with dark blue color).

between detection modules as one can see from Fig. 6.22. Exemplary histogram of energy depositions for one position of interaction and derivative of smoothed histogram with moving average is shown in Fig. 6.24. Final histogram of Compton edge position for all points of interaction along scintillators can be found in Fig. 6.25. There is a visible dependence of the energy deposition on the position of interaction of gamma quanta along the z -axis of a scintillator. Value of the Compton edge is slightly different for the irradiated positions in the center of the scintillator and on the edges. In the next step, a quadratic function was fitted to dependence of the energy deposition and the position of interaction of gamma quanta:

$$y = p_0(z - p_1)^2 + p_2 \quad (6.12)$$

where y and z stand for Compton edge position and the reconstructed hit position along the z -axis, respectively. p_0 , p_1 and p_2 are parabolas parameters. Fit was done in the range of $\langle -23, 23 \rangle$ [cm] and its result is visible in Fig. 6.25.

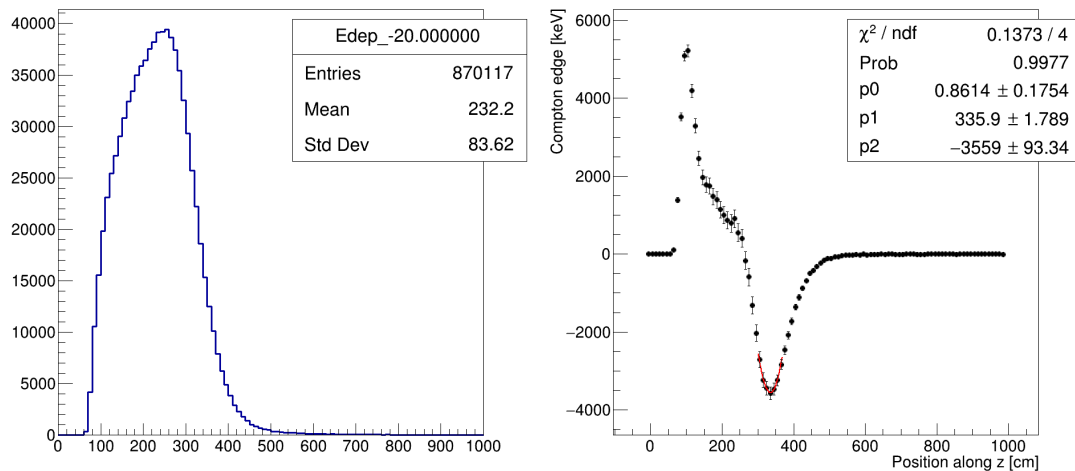


Figure 6.24: Histogram of all energy depositions for position -20 cm and its first derivative. In this case, minimum of the first derivative can be precisely described by a parabola which allows for precise determination of the minimum.

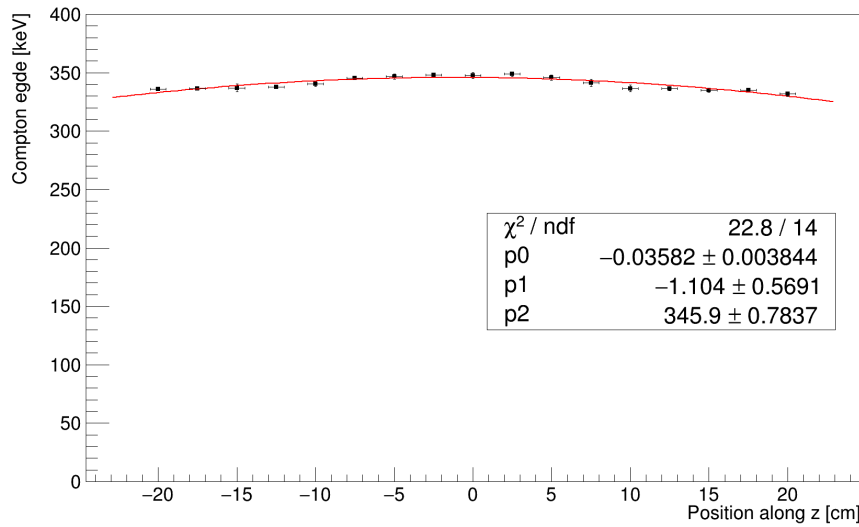


Figure 6.25: Values of Compton edges determined for all the scintillators at 17 points of interaction along z -axis. Quadratic function is fitted and its results are shown in statistic box.

In the last stage of the analysis all the corrections determined with measurements described in Ch. 5 were applied. For the further analysis a dedicated module was prepared in J-PET Framework. For each hit a TOT value is calculated and converted to energy deposition which is then divided by the rescale factor adequate for a given scintillator ID. In the last step, the dependence between energy deposition and position of interaction along scintillator is applied as:

$$p_z = p_0(z_{pos} - p_1)^2 + p_2 \quad (6.13)$$

where equation for p_z comes from fit of quadratic function (see Fig. 6.25) and $p_0 = -0.036 \pm 0.004$, $p_1 = -1.1 \pm 0.6$ and $p_3 = 345.9 \pm 0.8$. Abbreviation z_{pos} stands for place of interaction of gamma quanta along the z -axis of the detector. The finally corrected energy deposition E' is given by equation:

$$E' = \frac{E_{cal}}{p_z} \cdot 340 \quad (6.14)$$

where E_{cal} is energy deposition divided by rescale factor from previous step.

Data selection criterion applied after pairing signals into hits and after energy deposition calculations is the condition that energy deposition of each hit used to further analysis should be larger than 200 keV and smaller than 350 keV. Lower limit allows for reduction of contribution from detector-scattered coincidences. Gamma quanta cannot de-

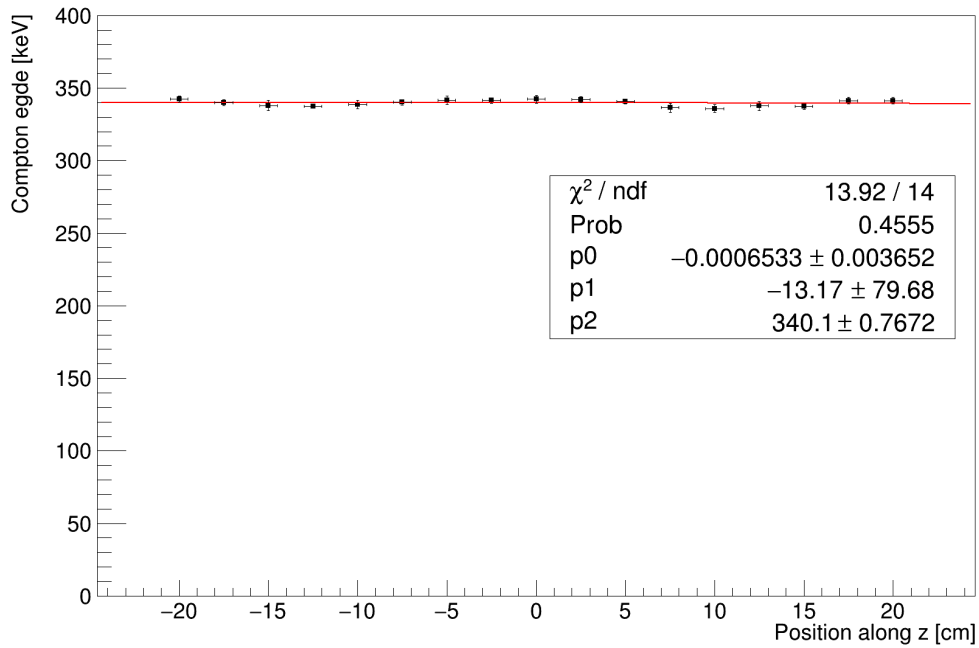


Figure 6.26: Value of Compton edges for all scintillators for 17 points after correction for place of interaction along z-axis.

posit more than 184 keV during second scattering [130,131]. Moreover, ratio between true and scattered coincidences increases by a factor of ~ 16 when the lower energy threshold is set to 200 keV [130]. Upper limit on the energy threshold allows for reduction of contribution from high-energetic gamma quanta, e.g. from the de-excitation of ^{22}Ne or from decay of the excited ^{68}Ga emitting 1077 keV line.

Energy thresholds described above are used in the further analysis as first data selection criterion on the level of hits to remove background and to decrease data size. Data selection criteria described in Sec. 6.2 are applied on level of events.

Chapter 7

NEMA characteristics studies

In this part of the thesis results of the measurements described in Ch. 5 are presented. Each step of the analysis is explained in detail. Before the final analysis performed according to the NEMA NU2-2012 norm calibration procedures and preselection conditions were applied to the data (see Ch. 6).

7.1 Sensitivity

In the Positron Emission Tomography different types of coincidence events such as true, random, scattered or multiple can take place. In the sensitivity estimation procedure only true events are desired. Applied preselection methods allowed to remove unnecessary background as much as possible.

The NEMA norm states that at least one of the two following conditions has to be fulfilled during sensitivity measurement:

- the percent of dead time losses are less than 5%,
- the random coincidence rate is less than 5% of total event rate.

^{18}F is the suggested radionuclide for sensitivity measurement, but in case of J-PET a ^{68}Ge source was used. Due to different detector geometry, different scintillation material and different type of source it was necessary to check these conditions with different assumptions in comparison to the commercial PET scanners:

- in order to determine the dead time losses an expected number of counts per scintillator (N_{scint}) has to be estimated from the following formula:

$$N_{scint} = \frac{\Omega}{4H} \cdot N_{emitted} \cdot \epsilon \quad (7.1)$$

where Ω stands for solid angle, $N_{emitted}$ means number of emitted particles by radioactive source and ϵ is the mean efficiency of plastic scintillators for detection of 511-keV gamma quanta estimated for all J-PET detection modules [132]. The solid angle Ω can be easily calculated from the following equation:

$$\Omega = 4\arctan\left(\frac{\alpha\beta}{2d\sqrt{4d^2 + \alpha^2 + \beta^2}}\right) \quad (7.2)$$

where α and β stands for scintillator dimensions while d denotes the distance between source and scintillator surface as one can see in Fig. 7.1

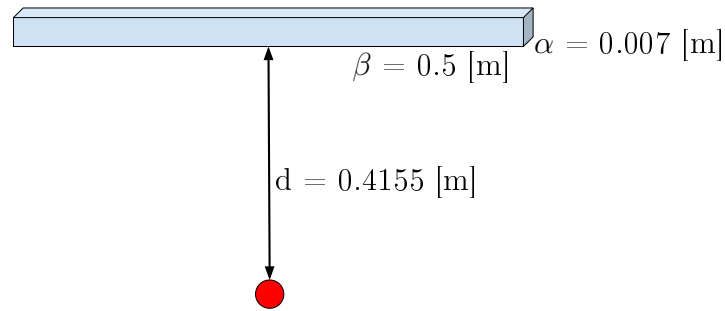


Figure 7.1: Schematic view of a relative position of the J-PET module and radioactive source used in the sensitivity measurements. It was assumed that the activity is concentrated in a point source placed in the detector center. Figure not to scale.

Taking into account activity of the radioactive source used in the measurements equal to 8.3 MBq and the geometry of the J-PET detector from Eqs. 7.1 and 7.2 we obtain the following values of Ω and N_{scint} :

$$\Omega = 0.0174 \quad (7.3)$$

$$N_{scint} = \frac{0.0174}{4H} \cdot 8.3 \cdot 1E6 \cdot 20\% = 2298.5 \frac{1}{s} \quad (7.4)$$

The relation between the real counts rate (N_{scint}) and the measured one (M) including system dead time (d) is given by the formula [133]:

$$M = N_{scint}e^{-N_{scint}d} \quad (7.5)$$

Dead time of the FPGA readout combined with fast signals from scintillators in J-PET is in the order of 20 ns [134]. Thus, losses in counts per scintillator due to system dead time are smaller than 1% in case of the J-PET detector:

$$\frac{M}{N_{scint}} = 0.99995 \quad (7.6)$$

- in order to determine the random coincidence rate one can use the following formula:

$$n_{random} = 2n_1n_2\tau \quad (7.7)$$

where n_1 and n_2 stands for average frequencies of two rectangular pulses statistically distributed according to the Poisson's statistics. In case of source placed along detector z -axis these frequencies are the same and one can use value of N_{scint} as n_1 and n_2 instead of M from previous point, because difference between N_{scint} and M is negligible. This formula contains also assumption that impulses duration τ are exactly the same [135] and in this case one can use the time window size from data preselection equal to 4 ns as τ . The pulse width in case of EJ-230 according to the specification is equal to 1.3 ns [59]. Taking into account values of the parameters in Eq. 7.7 mentioned above we obtain the random coincidences rate equal to:

$$n_{random} = 0.042 \frac{1}{s} \quad (7.8)$$

Thus, the random coincidences rate is less than 1% of the total event rate in case of the source activity of 8.3 MBq.

According to the NEMA norm, in the first step the corrected initial activity of the real source length should be calculated from Eq. 3.2. As it was mentioned earlier, a ^{68}Ge radioactive isotope in a form of line source was used in measurement with the PET Sensitivity Phantom. Active length of this source is equal to 50 cm.

Activity of the source was not measured by dose calibrator just before measurement, but was determined based on the ^{68}Ge half-life and value of initial activity measured on 13th December 2018 by manufacturer (see Sec. 5.1). Due to ^{68}Ge long half-life the activity change during measurements was below 0.9kBq/h and this value correspond to less than 0.01% of activity change per day. Based on this result there is no need to measure source activity before measurements in contrary to measurements with ^{18}F which decay fast (half-life equal to 109.8 minutes). Measurements with the PET Sensitivity Phantom were performed from 30.01.2020 to 02.02.2020 and in this period of time the activity of the used source changed from 8344 kBq to 8259 kBq. Activity change below 100 kBq is almost negligible, but average activity during measurement in a given phantom position can be easily determined. Below one can find value of A_{cal} in positions (0,0) and (0,10) [cm] averaged for all 5 sleeves:

$$A_{cal,(0,0)} = 8333 * \frac{700}{500} = 11666.2 \text{ [kBq]} \quad (7.9)$$

$$A_{cal,(0,10)} = 8291 * \frac{700}{500} = 11607.4 \text{ [kBq]} \quad (7.10)$$

As one can see the calibrated activity of ^{68}Ge is increased due to source length by factor $\frac{7}{5}$ and this value will be lowering significantly the system sensitivity. NEMA norm predicts the source length change at the level of ± 20 mm, but there was no possibility to use source with length equal ~ 700 mm. In case of measurement with the J-PET detector position of the PET Sensitivity Phantom did not change during the whole procedure. Moreover, the active part of scintillators was all the time covered by active part of the source. During measurements with commercial PET scanners with smaller FOV, in comparison to the J-PET, scanning procedure is performed part by part and phantom is moving along detectors. Based on facts mentioned above activity equal to 8333 kBq and 8291 kBq should be used for measurements analysis for position (0,0) and (0,10) [cm], respectively.

In the next step, the corrected total count rate should be calculated for each sleeve based on Eq. 3.15:

$$R_{CORR,j} = \frac{(T_{j,acq} \ln 2) \exp\left(\frac{T_j - T_{cal}}{T_{1/2}} \ln 2\right)}{T_{1/2} (1 - \exp\left(-\frac{T_{j,acq}}{T_{1/2}} \ln 2\right))} R_j \quad (7.11)$$

where $T_{j,acq}$ stands for acquisition duration of j-th measurement, T_j is the measurement starting time while T_{cal} is the time of radioactivity calibration measurement. In order to check $R_{CORR,j}$ with long-lived ^{68}Ge source a measurement with 2 sleeves in position (0,0) [cm] was chosen as a reference. Measurement duration was equal to 6 h. It was assumed that the source activity was determined at noon. Taking into account an appropriate values one can obtain value of $R_{CORR,j}$:

$$R_{CORR,j} = 1.0008 R_j \quad (7.12)$$

As one can see the difference between $R_{CORR,j}$ and R_j is negligible and thus there is no need to perform calculation of $R_{CORR,j}$ for each measurement. Even for a calibration performed 24 hours earlier ($T_{cal}=1$ day) the corrected total count rate ($R_{CORR,j}$) is equal to $1.0029 R_j$. Therefore, in the further analysis R_j was taken as $R_{CORR,j}$.

The NEMA norm requires that at least 10 000 true coincidences should be collected per slice but there is no exact slice definition. It is only mentioned that single slice should be rebinned to assign counts in oblique LORs to a proper image slice, but due to the J-PET detector geometry position of annihilation and position of gamma quanta interaction with scintillator are well defined and there is no need to perform single slice

rebinning. The exact method of counts measurement per slice is unclear and for further analysis slice is defined as a region with size equal to 1 cm. Grouping into slices was performed based on annihilation position as it was done in [125]. Gamma quanta can interact with the whole active length of a scintillator as one can see in Fig. 7.2.

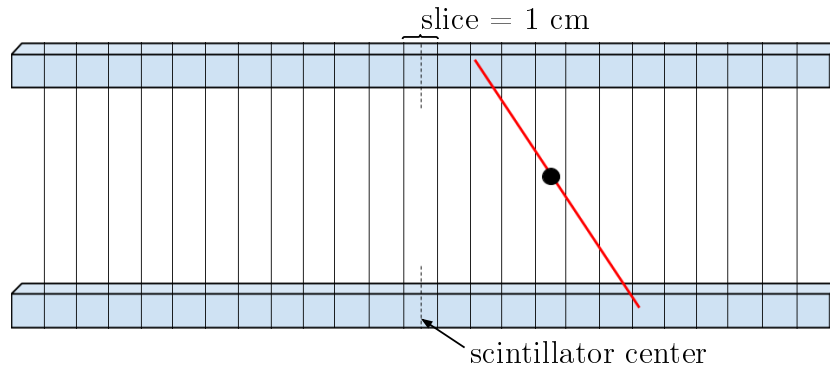


Figure 7.2: Pictorial representation of a scintillator divided into 1 cm wide slices. Scintillator center (dotted line) is located exactly in the middle of the central slice. Figure and number of slices are not to scale.

Profiles in this 3D mode were drawn for each sleeve measurement in position (0,0) [cm] as well as position (0,10) [cm]. Exemplary histogram for 1 and 5 sleeves in position (0,0) [cm] are shown in Fig. 7.3.

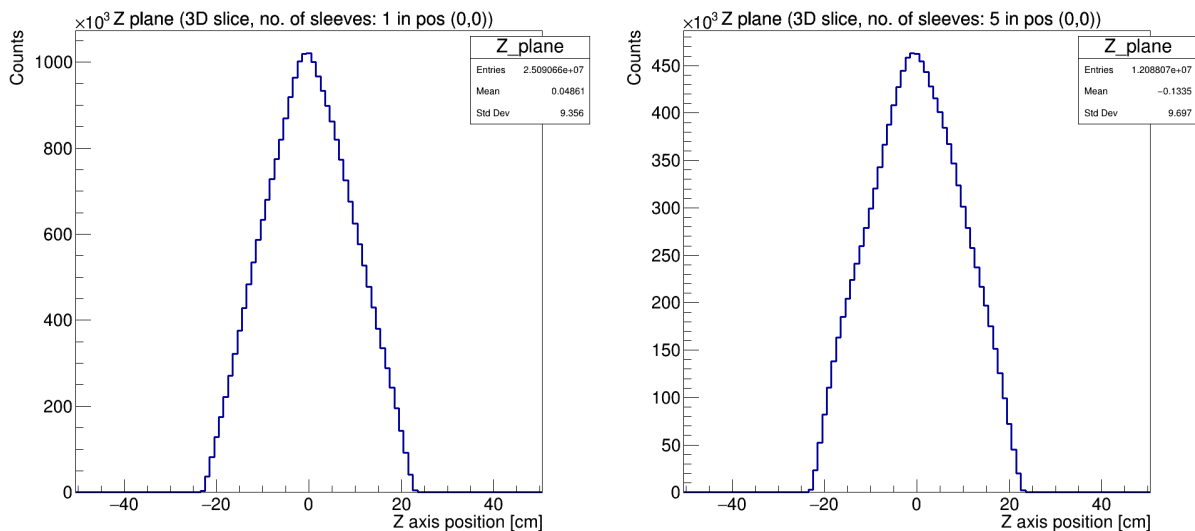


Figure 7.3: Profile for 1 sleeve (left) and 5 sleeves (right) in position (0,0) [cm] drawn based on information about annihilation position.

In the next step, the total count rate R_j was drawn as a function of accumulated wall thickness (combined thickness of sleeves walls) and it was fitted with Eq. 3.16 as one can

see in Fig. 7.4. Number of counts for each measurement was normalized to its duration. The exact measurement time was obtained based on number of time windows and this procedure is described below in details.

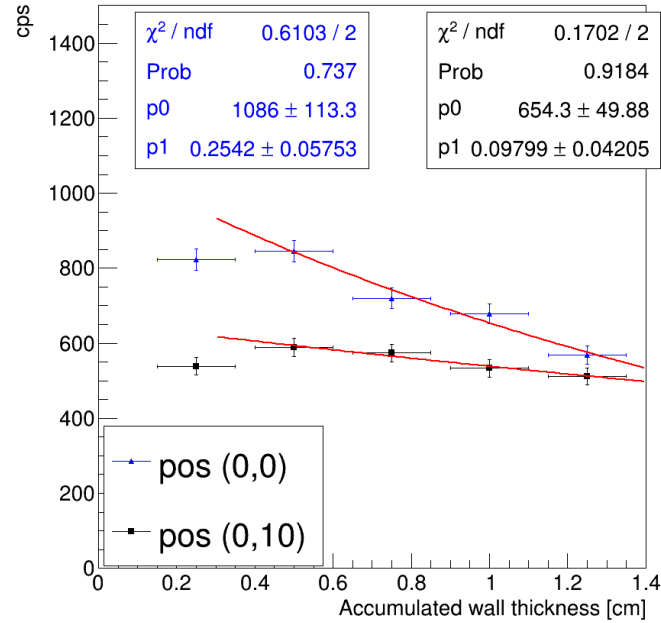


Figure 7.4: R_j as a function of accumulated wall thickness with fit performed according to Eq. 3.16. Count rate per second (cps) decreases with the increasing wall thickness. Graphs drawn for measurement in position (0,0) [cm] and (0,10) [cm].

Windows are sequential periods of time in which measurement is conducted and data is collected. Time windows have been counted at the very first analysis level (see Sec. 4.4) even for corrupted signals from the detector and therefore they provide calculation of the understated measurement time.

Measurement duration (T_{meas}) can be obtained from the following formula:

$$T_{meas} = \frac{\sum_{i=1}^n tw_i}{f} \quad (7.13)$$

where tw_i means number of time windows from i -th file while f stands for the FPGA clock frequency equal to 50 kHz. The accuracy of measurement duration obtained based on this method is at the level of seconds and results one can find in Tab 7.1.

As one can see in Fig. 7.4 the first points corresponding to the measurement with one sleeve (accumulated wall thickness equal to 0.25 cm) for position (0,0) [cm] as well as for position (0,10) [cm] were not taken into account in the data fit since they do not follow the trend of the rest of the data. One can find a reason of this strange result in Sec. 6.3

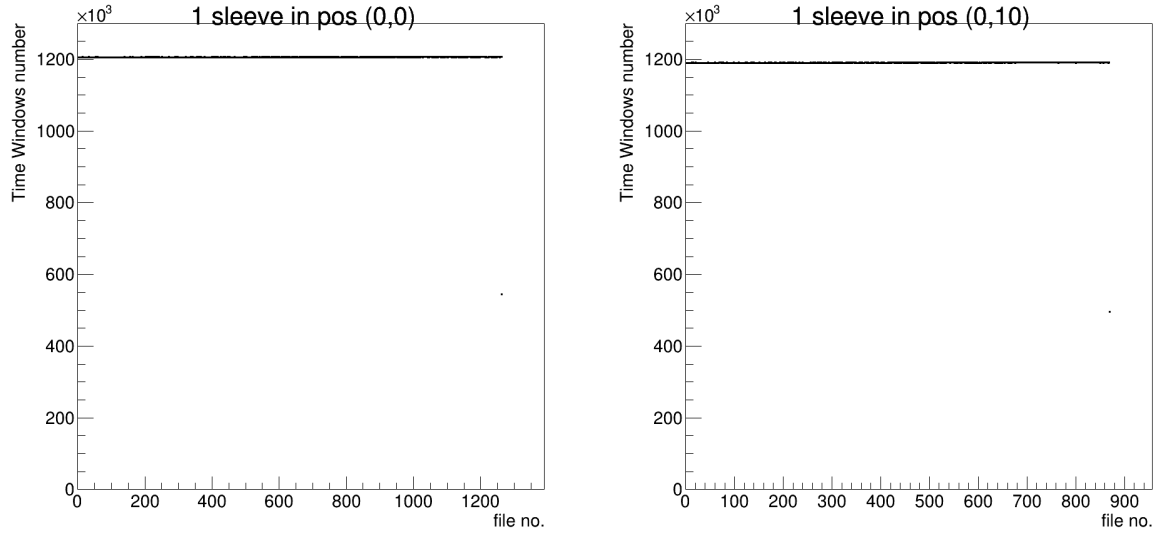


Figure 7.5: Number of time windows per file for masurement with 1 sleeve in position (0,0) [cm] (left) and (0,10) [cm] (right). Last point with smaller number of time windows correspond to the last measurement file which was saved with smaller amount of data.

Table 7.1: Measurement duration obtained based on time windows counting method.

	Position (0,0) [s]	Position (0,10) [s]
1 sleeve	30454.7	20702.4
2 sleeves	21054.2	21128.1
3 sleeves	20775	28835.6
4 sleeves	33486	21199.7
5 sleeves	21252.8	21099.5

and more specifically in Tab. 6.1. For a thorough explanation, average positrons range in aluminum (1.31 mm) is larger than sleeve thickness (1.25 mm). Thus, smaller number of positrons annihilate in the first sleeve than in two sleeves and due to this fact one can observe smaller number of counts.

System sensitivity can be calculated from Eq. 3.17 and its uncertainty can be obtained using the error propagation law:

$$\delta(S) = \frac{\delta(R_{CORR,0})}{A_{cal}} \quad (7.14)$$

Result of system sensitivity for measurements with the PET Sensitivity Phantom in positions (0,0) [cm] and (0,10) [cm] can be found below:

$$S_0 = \frac{1086 \text{ cps}}{8333 \text{ kBq}} = 0.130 \pm 0.014 \frac{\text{cps}}{\text{kBq}} \quad (7.15)$$

$$S_{10} = \frac{654.3 \text{ cps}}{8291 \text{ kBq}} = 0.0789 \pm 0.0061 \frac{\text{cps}}{\text{kBq}} \quad (7.16)$$

Axial sensitivity profile for the smallest tube in the central position can be computed and drawn after calculation of system sensitivity:

$$S_i = \frac{R_{1,i}}{R_1} \cdot S_0 \quad (7.17)$$

where $R_{1,i}$ stands for counts per second in i -th slice and R_1 stands for total cps for the smallest tube and S_0 is the system sensitivity. The results of these calculations are presented in Fig. 7.6.

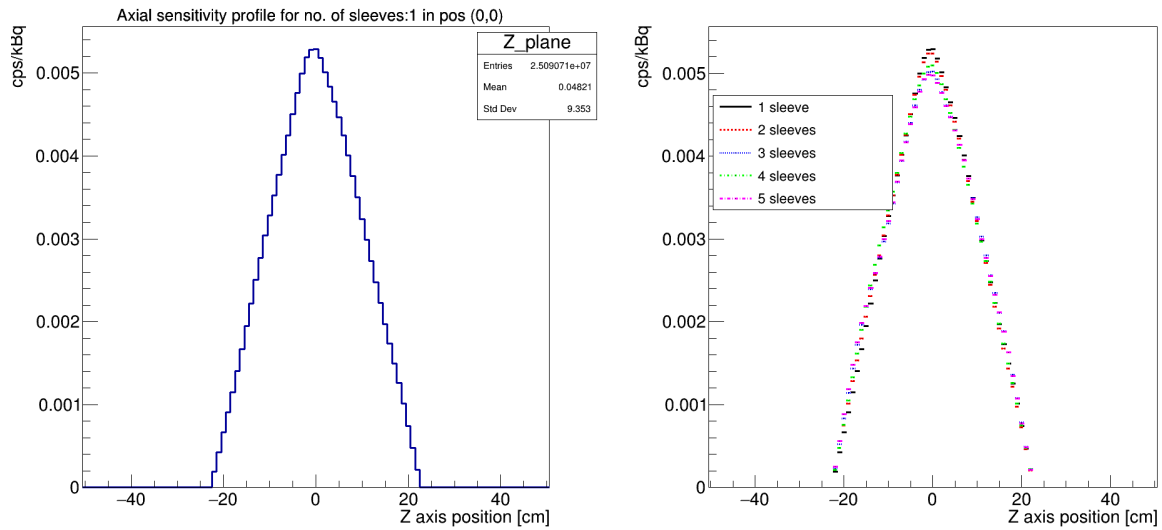


Figure 7.6: (left) Axial sensitivity profile in the central position for the smallest sleeve. (right) Axial sensitivity profiles comparison between measurements with different number of sleeves in central position. Difference between one and two sleeves is almost negligible.

7.2 Spatial resolution

From the very beginning, PET detectors have been improved and optimized with regard to the spatial resolution by usage of different detector elements' sizes and geometry. A high value of spatial resolution translates to high imaging resolution, which is really important in estimation of tracer concentration in tissue, especially when tissue size is comparable to detector spatial resolution [136]. Result of measurements with point source at several positions along the detector field-of-view becomes the best-case and relatively easy comparison between different PET detectors available on the market.

To perform measurements of detector spatial resolution, a ^{18}F shall be used as a radionuclide according to the NEMA norm, but one can find also in literature a large number of studies performed with ^{22}Na source as a radionuclide, e.g. a novel calibration scheme for PET detectors with ^{22}Na sources was successfully developed and validated and is widely used in Japan [119,137]. Besides the source used in measurements, NEMA norm says that activity of the source should be sufficiently low to meet one of the following conditions:

- the percent of dead time losses are less than 5%,
- the random coincidence rate is less than 5% of total event rate.

These conditions are exactly the same as for measurements with the PET Sensitivity Phantom and were discussed in details in Sec. 7.1, but there is a necessity of performing calculations once again due to different source activity used in the detector resolution estimation:

- in order to determine the dead time losses one can obtain the number of expected counts per scintillator using the formula 7.1 with activity of ^{22}Na source in the day of measurement (3.869 MBq) instead of activity of ^{68}Ge source:

$$N_{scint} = \frac{0.0174}{4\Pi} \cdot 3.869 \cdot 1E6 \cdot 20\% \approx 1071 \frac{1}{s} \quad (7.18)$$

In the next step, one can calculate the relation between measured counting rate and the real counting rate using the Eq. 7.5:

$$\frac{M}{N_{scint}} = 0.99998 \quad (7.19)$$

Count losses per scintillator due to the J-PET detector dead time is smaller than 1%.

- in order to determine the random coincidence rate one can use the Eq. 7.7 with 4 ns time window as τ and 1071 counts per seconds as n_1 and n_2 :

$$n_{random} = 0.009 \frac{1}{s} \quad (7.20)$$

The random coincidences rate is less than 1% of the total event rate in case of the J-PET detector when using the source with activity of 3.869 MBq.

Measurements with ^{22}Na source were performed between 27th and 29th of January 2020 and the change of activity was at the level of few kilobecquerels. The change in number of counts per second associated with an activity decrease is negligible from the point

of view of above conditions. Measurements with the sodium source were performed for each position separately as it was mention in Sec. 5.3. Preselected data was reconstructed with Filtered Back-Projection (FBP) algorithm and analyzed according to the NEMA norm [138].

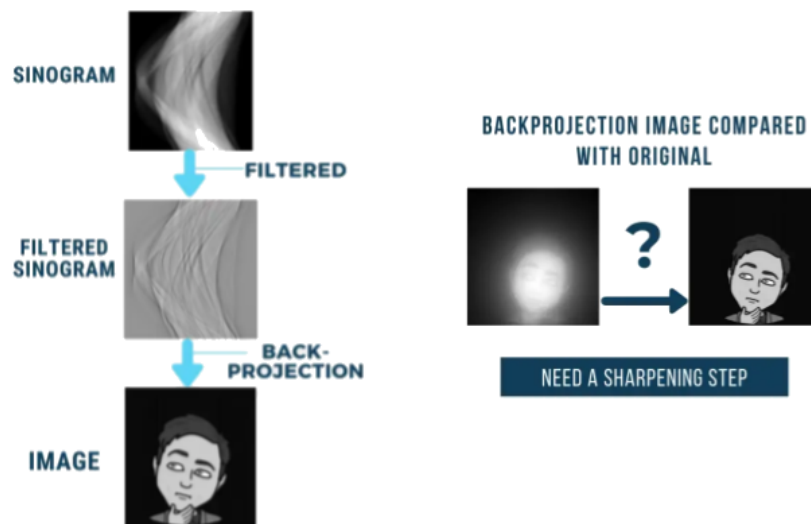


Figure 7.7: Graphical explanation of steps of Filtered Back-Projection is shown on left panel of the figure. Filters are necessary to sharpen obtained image. This correction can be performed on the level of sinogram. Figure adapted from [139].

Filtered Back-Projection includes three steps as one can see in Fig. 7.7:

- forward projection - data is stored in a form of sinogram,
- filtering - filters are used to perform deblurring operation on sinogram,
- back projection - filtered sinogram is back projected into image domain [140].

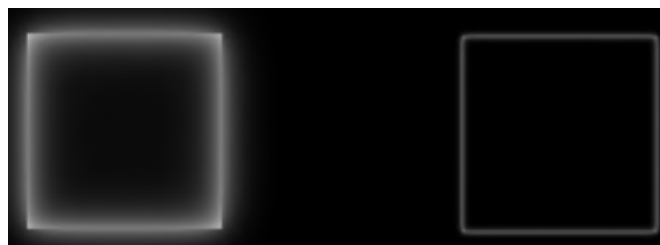


Figure 7.8: Image before (left) and after (right) filtration operation. Figure adapted from [138].

During the filtration operation each sinogram angle is transformed to the Fourier space and multiplied by high-pass frequency filter which supresses low frequencies and raises high

frequencies. The mathematical derivation of filtration in frequency-domain was described in [138]. High pass filters allow to sharpen image on its edges, but it increases also the statistical noise (see Fig. 7.8). High pass RamLak filter is usually combined with low pass filters in order to reduce this amplification [141]. Relation between gain and frequency is shown in Fig. 7.9.

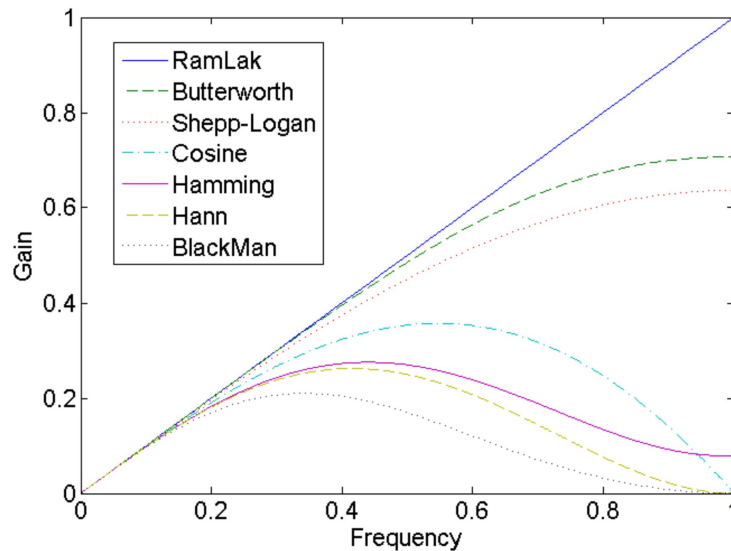


Figure 7.9: Shape of filters used in Filtered Back-Projection. Horizontal axis represents the frequency contribution to the image while the vertical axis is the current frequency multiplier. RamLak, Butterworth and Shepp-Logan belong to high-resolution filters. Cosine, Hamming and Hann filters reduce noise better than high-resolution filters. Figure adapted from [142].

After filtration operation, Inverse Fourier Transform has to be performed to obtain filtered sinogram and to obtain 2D image reconstructed from this sinogram the Inverse Radon Transform has to be used [138]. To keep image details and to find out the best-case compromise between value of the spatial resolution and noise level, study of the frequency cutoff value has to be performed. Studies performed and presented in [138] shown that in case of simulated NEMA phantom the best results were obtained for Shepp-Logan filter with cutoff value equal to 0.75. Due to these results, studies of best-case cutoff value for experimental data were performed for the Shepp-Logan filter for source placed in position $(0,1,0)$ [cm].

Sinogram and 2D reconstructed image were generated by FBP algorithm for each slice along z -axis (see Fig. 7.10). Z -axis was divided into 101 slices including additional slice (called slice 0) for central position and fifty slices on the left and right side of scintillator middle point.

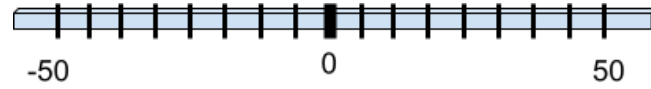


Figure 7.10: Graphical explanation of dividing scintillator into 101 slices. There is fifty slices on the left and right side according to scintillator center. Additional slice has been done for scintillator middle point. Slices are evenly distributed along scintillator. Figure not to scale.

In post-processing analysis, each reconstructed image was read bin by bin and converted to root and more readable Portable Network Graphic file (see Fig. 7.11). As it was mentioned earlier, each image was read bin by bin. Post-processing algorithm was looking for the highest bin and its intensity in each slice and saved these informations for each slice along the z -axis to one file. 3D image was created as a result of merging of all the 2D reconstructed images.

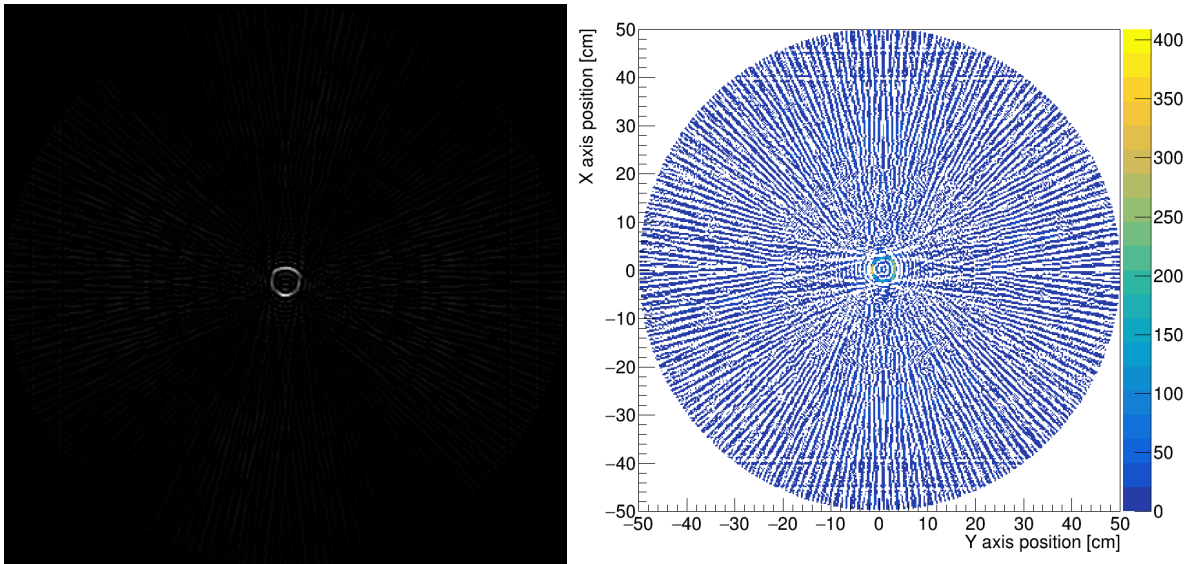


Figure 7.11: Results of image reconstruction performed with FBP algorithm for source in position $(0,1,0)$ [cm] with Shepp-Logan filter and cutoff value equal to 0.3 is presented on left panel. Presented image was obtained for slice 0 along z -axis. Post-analysis result of reconstructed image is presented on right panel. Circle shape is observed for xy plane instead of expected point size source due to too low cutoff value.

In the next step, the one-dimensional response function was drawn through the distribution peak for all three directions according to the NEMA norm. The maximum value for each profile was determined by parabolic fit to the peak point and two adjacent pixels. The FWHM was determined by linear interpolation between neighboring bins at one half of this maximum value as one can see in Fig. 7.12.

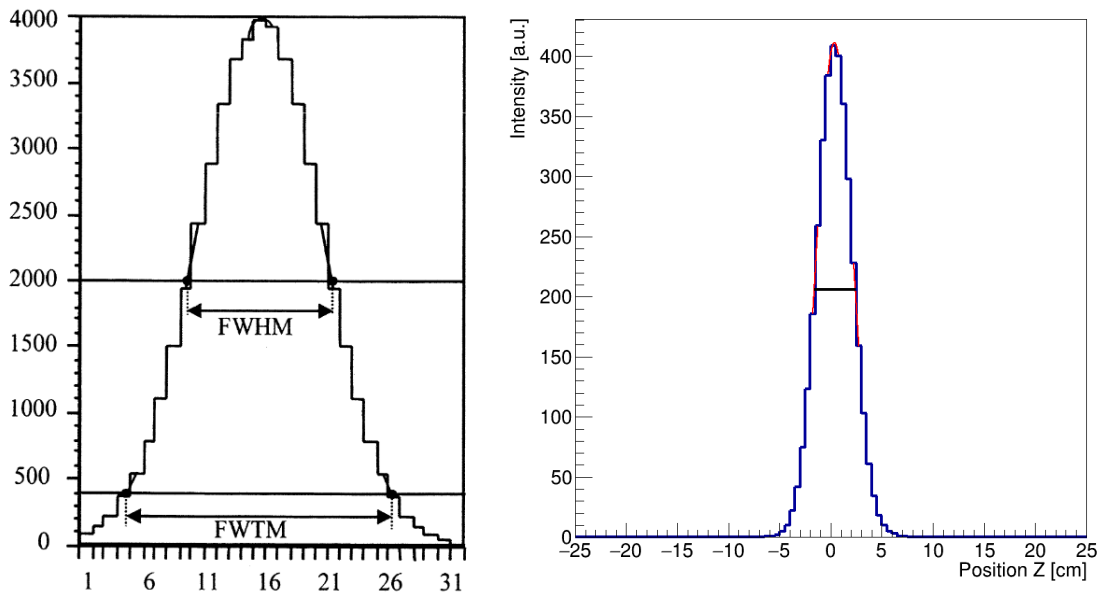


Figure 7.12: (left) One-dimensional response function with parabolic fit to the maximum and FWHM and FWTM determination indicated. Figure adapted from [143]. (right) Response function along the z -axis formed for experimental data from measurements with source in position $(0,1,0)$ [cm] with indicated graphical determination of distribution maximum and FWHM value.

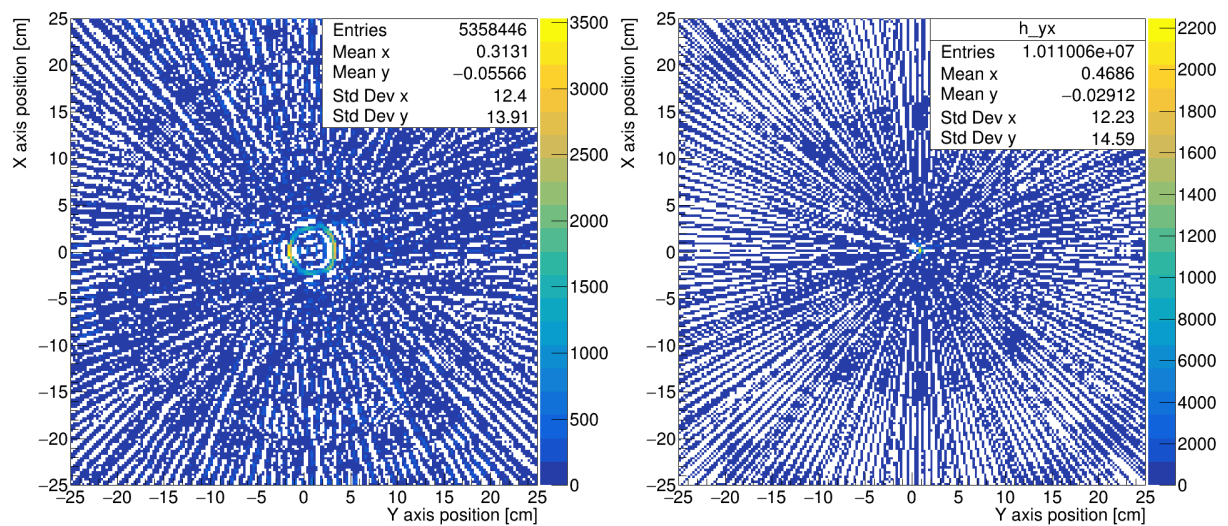


Figure 7.13: Control histogram for the 3D image in the xy plane for source placed in position $(0,1,0)$ [cm] reconstructed with Shepp-Logan filter and cutoff value equal to 0.3 (left) and 3.0 (right), respectively.

FWHM value can be easily determined for distribution along z -axis, but the shape of the distributions along x - and y -axis strongly depends on the applied cutoff value. For xy plane visible in Fig. 7.13, a circular shape was visible instead of expected point shape. This effect disappears for larger cutoff value.

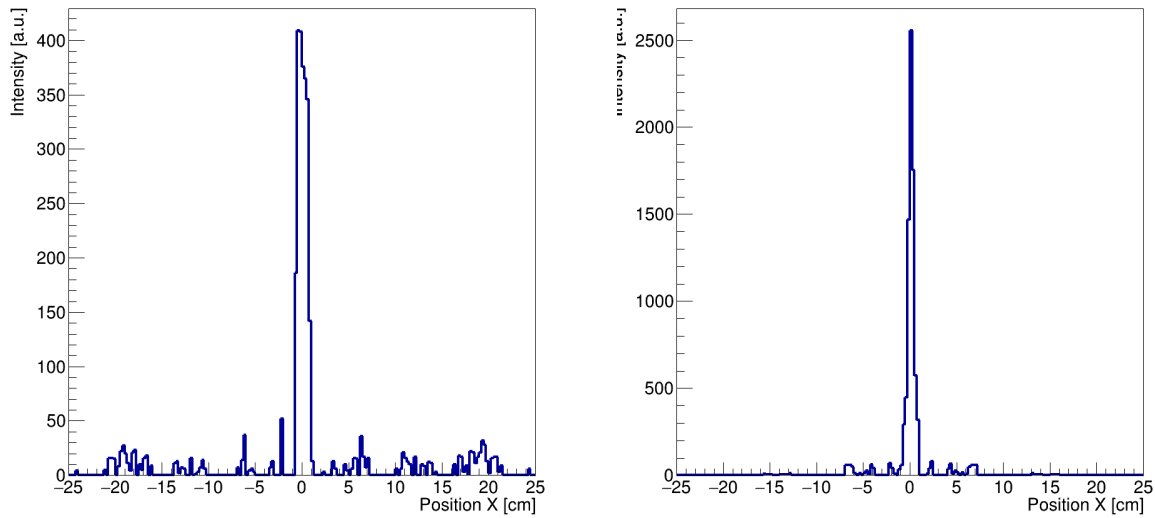


Figure 7.14: Distribution along x -axis for source placed in position $(0,1,0)$ [cm] for reconstructed image with Shepp-Logan filter and cutoff value equal to 0.3 (left) and 3.0 (right).

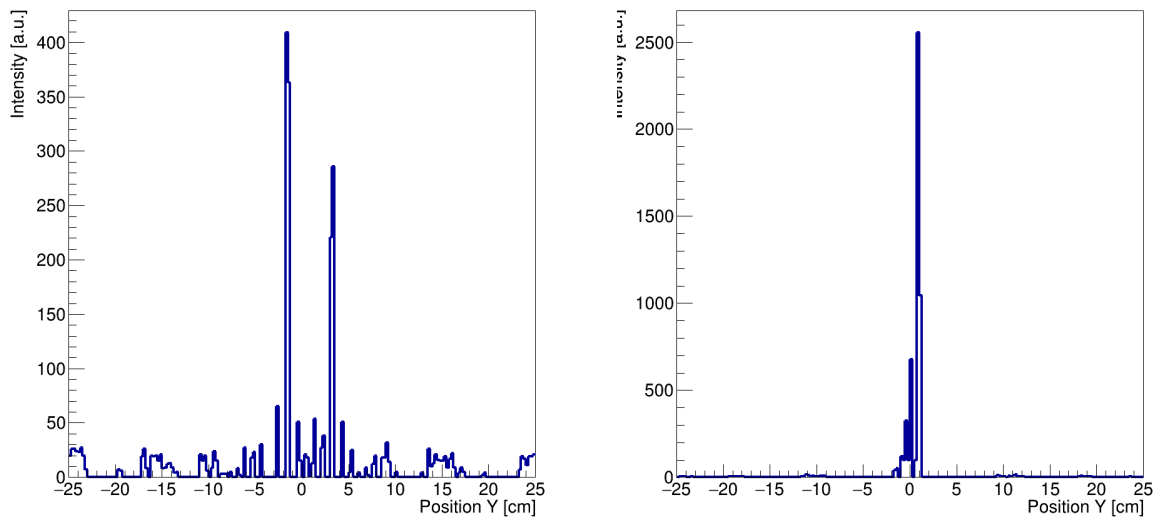


Figure 7.15: Distribution along y -axis for source placed in position $(0,1,0)$ [cm] for reconstructed image with Shepp-Logan filter and cutoff value equal to 0.3 (left) and 3.0 (right). Two peaks visible on left panel come from two maxima visible on left panel of Fig. 7.13.

The best-case cutoff value was determined based on the estimated value of FWHM. Two methods of determination of FWHM value with its uncertainty was implemented in post-process analysis. Preliminary cutoff value was set to 3.0 due to results obtained for distribution along y -axis.

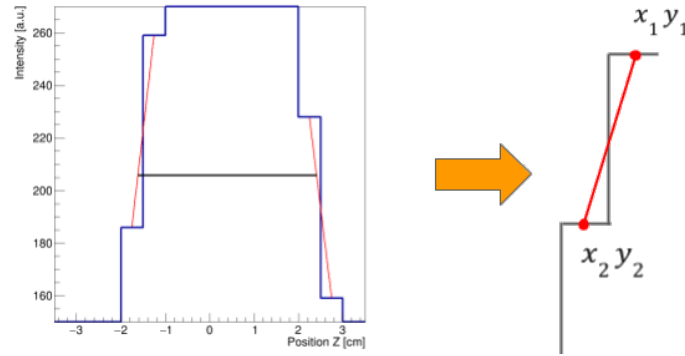


Figure 7.16: Graphical explanation of determination of linear fit between middle point of two neighbouring bins.

In first method linear interpolation between two adjacent bins was performed based on the calculations of bins center point on the left and right side of the distribution. Parameters of the linear fit from left side of the distribution (see Fig. 7.16) was found based on two equations:

$$y_1 = a_{left}x_1 + b_{left} \quad (7.21)$$

$$y_2 = a_{left}x_2 + b_{left} \quad (7.22)$$

Subtracting these two equations from each other one can obtain parameters a_{left} and b_{left} of the linear fit between two bins from left side and their uncertainty:

$$y_1 - y_2 = a_{left}(x_1 - x_2) \quad (7.23)$$

$$a_{left} = \frac{y_1 - y_2}{x_1 - x_2} \quad (7.24)$$

$$\delta a_{left} = \sqrt{\left(\frac{\partial a_{left}}{\partial x_1}\right)^2 \Delta x_1^2 + \left(\frac{\partial a_{left}}{\partial x_2}\right)^2 \Delta x_2^2} \quad (7.25)$$

$$b_{left} = y_1 - a_{left}x_1 \quad (7.26)$$

$$\delta b_{left} = \sqrt{\left(\frac{\partial b_{left}}{\partial a_{left}}\right)^2 \Delta a_{left}^2 + \left(\frac{\partial b_{left}}{\partial x_1}\right)^2 \Delta x_1^2} \quad (7.27)$$

where: $\Delta x = \Delta x_1 = \Delta x_2$ equals to $\frac{\text{binwidth}}{\sqrt{3}}$. The uncertainty of y was not taken into account, because it is not the direct number of counts on the histogram, y stands for the intensity counted by reconstruction.

The same operation was performed to find linear fit for right side of the distribution. The FWHM value was calculated as:

$$FWHM = x_{right} - x_{left} \quad (7.28)$$

where:

$$x_{left} = \frac{H_{1/2} - b_{left}}{a_{left}} \quad (7.29)$$

The equation for x_{left} comes from the formula:

$$H_{1/2} = a_{left}x_{left} + b_{left} \quad (7.30)$$

$H_{1/2}$ stands for one half of the maximum determined from the parabolic fit to the peak of the distribution, while x_{left} and x_{right} are the intersection points of FWHM interpolation and linear fit from left and right side. The uncertainty of FWHM estimation can be calculated from the error propagation law:

$$\Delta FWHM = \sqrt{\Delta x_{right}^2 + \Delta x_{left}^2} \quad (7.31)$$

This method works very well for linear fit performed for left and right side of the distribution and is great for determination of FWHM value, but calculated uncertainty seems to be overestimated as one can see for results obtained for Shepp-Logan filter and cutoff value equal to 3.0 for x -axis in Fig. 7.17, y -axis in Fig. 7.18 and z -axis in Fig. 7.19, especially for positions close to edge of detector field-of-view. Thus, especially for distribution along x - and y -axis, where only few bins are used to FWHM value and its uncertainty estimation, there is no point of uncertainty calculations. Better solution, which can be used in this case, is a constant uncertainty equal to half of bin width. Taking into account the used FBP algorithm parameters, the uncertainty can be set on the level of 0.13 cm. On the other hand, the distribution along z -axis seems to be perfect to be fitted with Gaussian function in order to decrease value of estimated uncertainty.

Gaussian Fitting Function in ROOT environment was the second method used to estimation of FWHM value and its uncertainty for distribution along z -axis was calculated as:

$$\Delta FWHM = \sqrt{\left(\frac{\partial FWHM}{\partial \sigma}\right)^2 \Delta \sigma^2} = \sqrt{8 \ln 2} \Delta \sigma \quad (7.32)$$

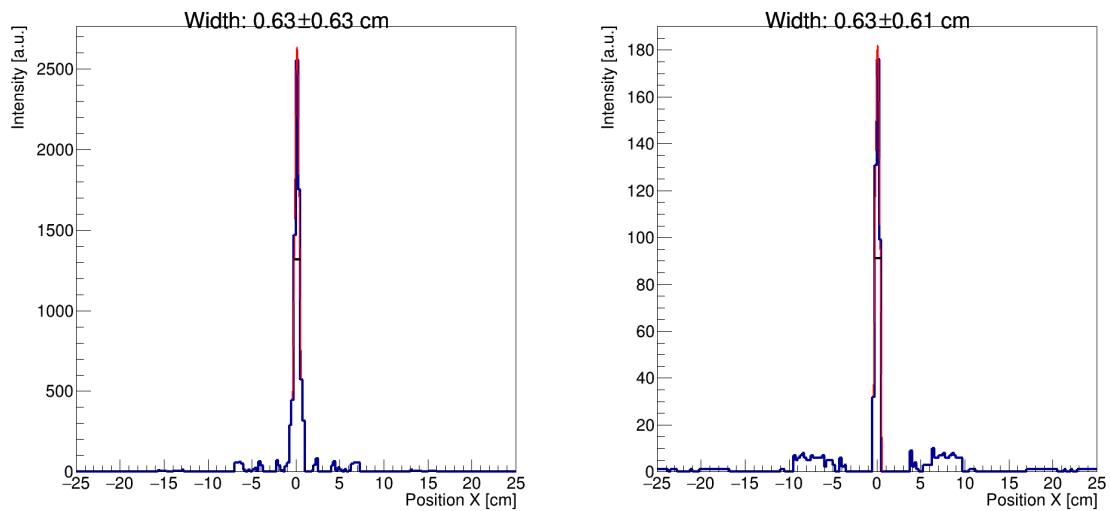


Figure 7.17: FWHM and its uncertainty estimation for distribution along x -axis performed with first method for position $(0,1,0)$ [cm] visible on left panel and for position $(0,20,-18.75)$ [cm] visible on right panel. The background comes from scattered and random coincidences as well as prompt gammas from ^{22}Na decay.

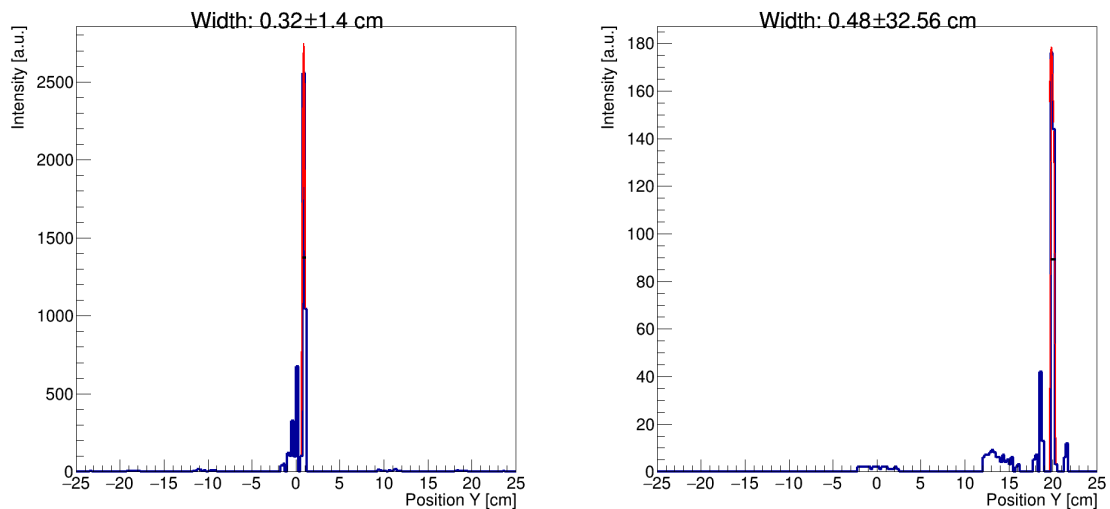


Figure 7.18: FWHM and its uncertainty estimation for distribution along y -axis performed with first method for position $(0,1,0)$ [cm] visible on left panel and for position $(0,20,-18.75)$ [cm] visible on right panel. The background comes from scattered and random coincidences as well as prompt gammas from ^{22}Na decay.

Results obtained for distribution along z -axis with Gaussian fit shows much more reasonable value of FWHM uncertainty as one can see in Fig. 7.20.

Studies of cutoff value show that cutoff set to 0.3 was too small and a circular shape

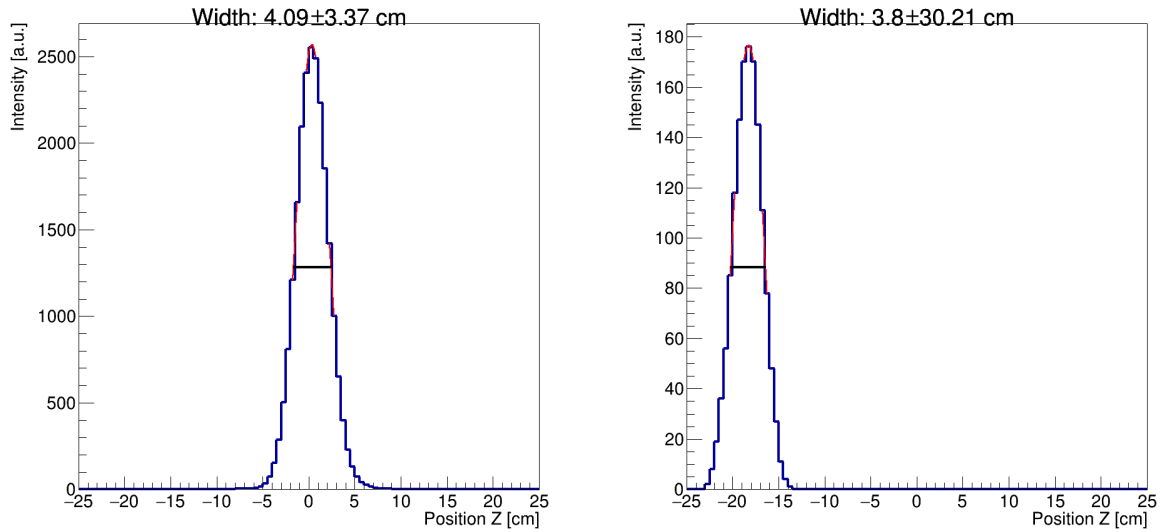


Figure 7.19: FWHM and its uncertainty estimation for distribution along z -axis performed with first method for position $(0,1,0)$ [cm] (left panel) and for position $(0,20,-18.75)$ [cm] (right panel).

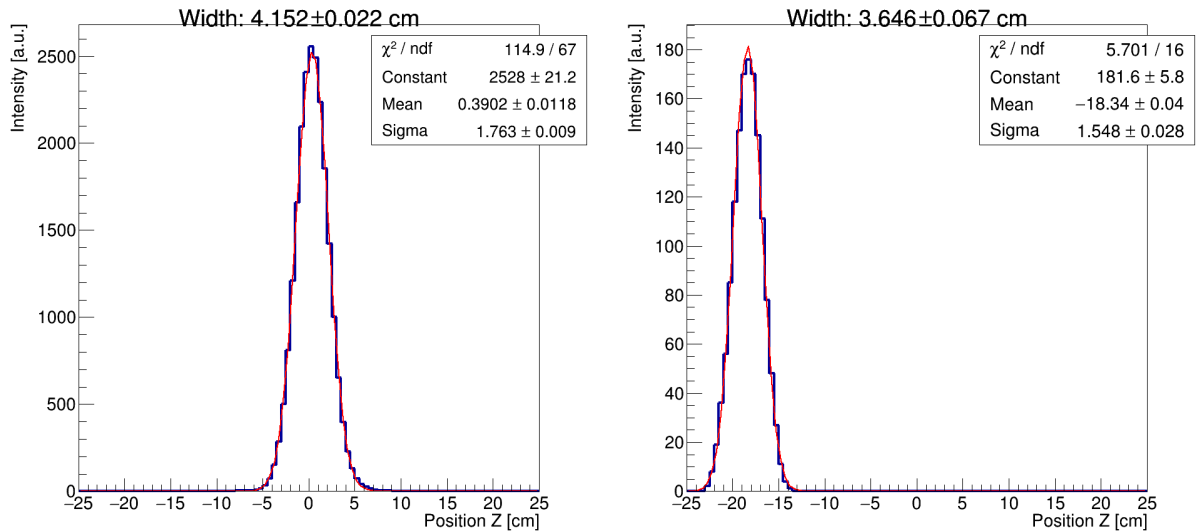


Figure 7.20: Intensity distribution along z -axis fitted with Gaussian function drawn for position $(0,1,0)$ [cm] is visible on left panel and for position $(0,20,-18.75)$ [cm] is visible on right panel of the figure.

was observed for xy plane which generates the two peaks visible for distribution along y -axis. These two peaks and circular shape disappeared for cutoff value equal to 3.0. During post-processing analysis a few values of cutoff were checked such as cutoff value equal to 0.3, 0.5, 0.75, 1.0, 2.0, 3.0, 4.0 and 5.0.

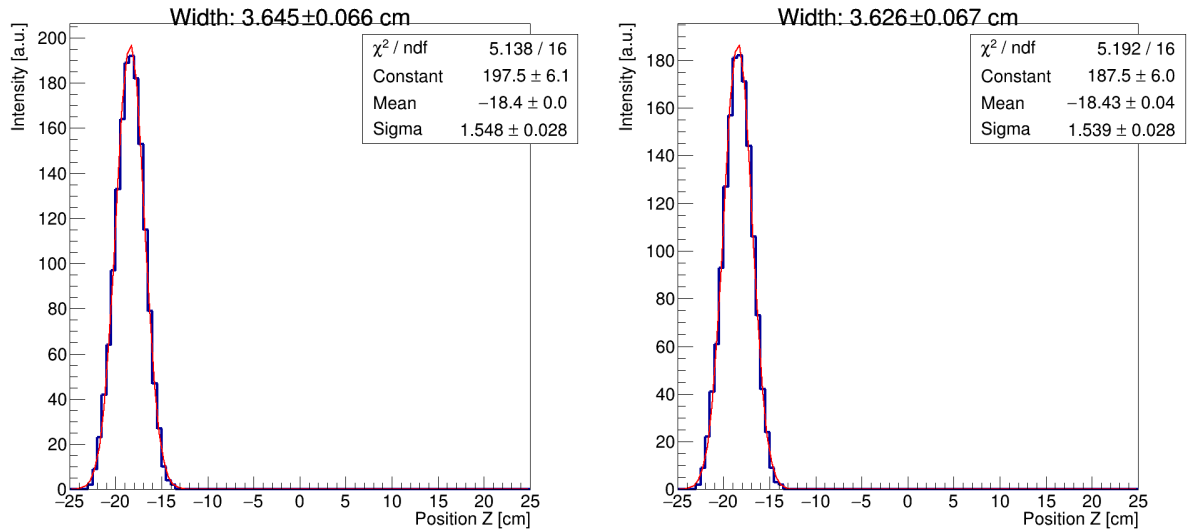


Figure 7.21: Intensity distribution along z -axis drawn for (0,20,-18.75) [cm] for cutoff value equal to 4.0 (left) and 5.0 (right).

The best-case cutoff value was equal to 3.0. Results for cutoff value equal to 4.0 and 5.0 were very similar to results observed for cutoff equal to 3.0, especially for positions close to edge of the detector field-of-view, as one can see in Fig. 7.20 and Fig. 7.21. There was no reason to go too far with cutoff value. The value of best-case cutoff (3.0) for experimental data is bigger than the value for Monte Carlo simulations (0.75) [144].

The best-case cutoff value was chosen based on FWHM value. For distribution along x - and y -axis, the value of FWHM was estimated based on linear fit from left and right side of the distribution and linear interpolation between these two sides, while the uncertainty was decided to be constant for each position. The Gaussian function was fitted to the distribution along z -axis to estimate FWHM value and its uncertainty due to overestimated uncertainty value obtained with first method.

In the last step of the post-processing analysis, studies of influence of different filters on FWHM value were performed for the cutoff equal to 3.0 for two positions: center of the detector and the edge of the detector field-of-view. Results of these studies one can find in the Tab. 7.2. Results show that the best filter for the experimental data would be the Ridgelet filter. For this filter, the FWHM value was the smallest one for two most important positions from the point of view of changing the FWHM value with position along y - and z -axis. For these two positions tendency of decreasing FWHM value for Ridgelet filter has been observed and makes it possible to assume that this tendency would be kept for other source positions.

Obtained results allowed to perform the final analysis of data from measurements with sodium source placed inside J-PET detector in six positions specified by the NEMA norm.

Table 7.2: Results of FWHM value with its uncertainty in cm for different filters shown in columns for two source positions: (0,1,0) [cm] and (0,20,-18.75) [cm] for x -, y - and z -axis.

Position [cm] /filter	Cosine	Hamming	Hann	Ridgelet	Shepp-Logan
(0,1,0)					
x	0.59 ± 0.13	0.60 ± 0.13	0.60 ± 0.13	0.53 ± 0.13	0.63 ± 0.13
y	0.28 ± 0.13	0.28 ± 0.13	0.28 ± 0.13	0.26 ± 0.13	0.32 ± 0.13
z	4.136 ± 0.017	4.137 ± 0.018	4.138 ± 0.018	4.121 ± 0.030	4.152 ± 0.022
(0,20,-18.75)					
x	0.66 ± 0.13	0.66 ± 0.13	0.67 ± 0.13	0.61 ± 0.13	0.63 ± 0.13
y	0.48 ± 0.13	0.48 ± 0.13	0.49 ± 0.13	0.41 ± 0.13	0.48 ± 0.13
z	3.685 ± 0.056	3.692 ± 0.058	3.687 ± 0.057	3.640 ± 0.108	3.646 ± 0.067

As it was mention in Sec. 3.1, the accuracy of the source positioning for the transaxial plane should be equal to ± 0.2 cm for source at 1 cm offset position and ± 0.5 cm for source at 10 cm and 20 cm offset position, while for the axial directions it should be equal to ± 0.2 cm for all source positions. Moreover, for each response function shall be collected at least one hundred thousand counts.

Table 7.3: Reconstructed source position along x -, y - and z -axis. One can find also number of measured counts for each position in the last column.

Position [cm]	X position [cm]	Y Position [cm]	Z Position [cm]	Number of counts
(0,1,0)	0.13	0.88	0.25	6 270 028
(0,1,-18.75)	0.13	0.88	-18.25	1 849 532
(0,10,0)	0.38	9.88	0.25	5 012 518
(0,10,-18.75)	0.38	10.13	-18.25	1 627 895
(0,20,0)	0.38	19.63	1.25	5 224 987
(0,20,-18.75)	0.13	19.88	-18.25	1 872 025

Reconstructed position of source along each axis was checked during post-process analysis (see Tab. 7.3). Center of the highest bin was assumed as the most likely source position. The difference between assumed and measured position along x -axis is in the range of 0.13 cm - 0.38 cm, while for y -axis the positioning accuracy is below 0.2 cm and only for position (0,20,0) is below 0.4 cm. The difference between assumed and measured position along z -axis is in the range of 0.25 - 0.5 cm. Positioning accuracy for

transaxial plane is below 0.5 cm as NEMA norm suggests, while for the axial direction this accuracy is larger. Larger value for z -axis can be caused by different geometry of the J-PET detector in comparison to commercial scanners. The resolution along z -axis is worst in comparison to resolution along x - and y -axis. Moreover, the highest bin was taken into account as a source position and for distribution along z -axis a Gaussian shape is observed instead of a peak. Measured number of counts, as one can find in Tab. 7.3, for each position is larger than 1 million. Largest value is observed for positions close to detector center and the smallest one are observed for positions close to field-of-view edge.

Table 7.4: Results of FWHM value for six positions specified by the NEMA norm and obtained for Ridgelet filter with cutoff value equal to 3.0.

Position [cm]	FWHM x [cm]	FWHM y [cm]	FWHM z [cm]
(0,1,0)	0.53 ± 0.13	0.26 ± 0.13	4.121 ± 0.030
(0,1,-18.75)	0.74 ± 0.13	0.30 ± 0.13	3.726 ± 0.067
(0,10,0)	0.68 ± 0.13	0.66 ± 0.13	3.643 ± 0.054
(0,10,-18.75)	0.75 ± 0.13	0.34 ± 0.13	3.68 ± 0.11
(0,20,0)	0.65 ± 0.13	0.48 ± 0.13	4.054 ± 0.060
(0,20,-18.75)	0.61 ± 0.13	0.41 ± 0.13	3.64 ± 0.11

The PSF value at full-width-at-half-maximum for the J-PET detector are specified in the Tab. 7.4. FWHM value for distribution along x -axis is larger than FWHM value for distribution along y -axis. This effect probably comes from the position of plexi panel inside the J-PET detector during measurements with sodium source and possible gamma quanta scatterings inside plexi. The spatial resolution is the worst along z -axis due to different geometry of J-PET detector as it was mentioned above. These values were expected, because in commercial scanners the spatial resolution is determined by crystal size and long scintillators were used instead of crystals in J-PET scanner.

NEMA norm contains requirement of calculations of spatial resolution defined as well as full-width-at-tenth-maximum (FWTM), but due to literature studies and information posted by PET devices manufacturers the FWHM value is very often reported as the spatial resolution for a given device [145–150].

7.3 Scatter fraction

False coincidences, associated with annihilation photons scatterings, lead to unwanted noise and introduce artefacts to the reconstructed image which cannot be compensated by the scatter correction algorithms [151]. There are two methods of measurements of

the detector sensitivity to scattered radiation described in NEMA NU-2-2012 [89] and respectively in Sec. 3.2. First method required random events measurement performed by one of two possible approaches:

- delayed window method - in commercial PET tomographs signals from a single detector are delayed by time which is significantly larger than the scanner resolution time. This delay is introduced by additional circuitry and this solution was not applied during J-PET detector construction [152, 153]. Although, this method can be applied in post-processing analysis and it was not performed in this work.
- singles rated method - random coincidences rate is calculated based on a single events rate on each detector in a ring during acquisition. Each photon energy deposition in a crystal generates a pulse which is passed to time pick-off unit and later to the gate generator. Gate generator opens a gate with duration equal to τ . If signals overlap each other in coincidence time window then they are passed to the sorting circuitry. Randoms rate (R_{ij}) can be calculated from the formula:

$$R_{ij} = 2\tau S_i S_j \quad (7.33)$$

where S_i and S_j stand for single-photon event rate in detectors i and j , respectively, while τ stands for coincidence time window. This method has one main disadvantage, always overestimates the true to random coincidences rate [52, 152–155]. This solution was not applied in electronic system used in the J-PET detector. Although, coincidences can be sorted in post-processing analysis, this method was not implemented in J-PET Framework and it is not explained in the NEMA norm. On the other hand, random coincidences estimation for unattenuated source placed in the center of the J-PET detector was performed in the case of sensitivity measurements.

In the second method only three final acquisitions are used to perform calculations of scattered fraction and this was not possible in case of this work due to the source type used during measurements with the J-PET detector.

Measurements with a dedicated PET Scatter Phantom were described in details in Sec. 5.2. A ^{68}Ge radioactive source was used instead of ^{18}F suggested in the NEMA norm [156, 157]. Activity of ^{68}Ge source in the day of measurement was equal to 8.49 MBq and due to long half-life does not change significantly during 19 hours acquisition. Literature studies shown that the activity of ^{18}F during scatter fraction measurements varied from 851.20 MBq to even 2.59 GBq, but in the studies performed with ^{68}Ge the activity was equal to 6.4 MBq [97, 112, 157, 158]. The corrected initial activity was calculated, exactly in the same way as for measurements with PET Sensitivity Phantom, from the formula:

$$A_{cal} = 8494.5 \text{ kBq} \cdot \frac{700 \text{ mm}}{500 \text{ mm}} = 11892.3 \text{ kBq} \quad (7.34)$$

Activity region was centered with respect to the PET Scatter Phantom and field-of-view of the J-PET detector. Phantom was also centered in the transverse and axial FOV.

According to the source type used during measurements with PET Scatter Phantom and the J-PET detector, only a single 19 hours long acquisition was performed instead of regular measurements at different activity levels. This long measurement allowed to fulfill the condition of 500 000 prompt counts collected per acquisition. Collected data was preselected according to the condition described in Ch. 6.

In relation to the data processing instruction included in the NEMA norm, a single sinogram should be created for each slice from oblique sinograms with a Single Slice Rebinning (SSRB) technique. To apply this condition to the preselected data, a dedicated module was prepared in the J-PET Framework software, which saved events in the format required by the post-processing algorithm. Coordinates of the interaction point of gamma quanta with the scintillator material along x -, y - and z -axis were saved to the text file. In next step, this text file was read by algorithm creating sinograms based on information about place of interaction. Algorithm, using the SSRB method, was prepared and implemented by the member of the J-PET reconstruction group, Sz. Parzych, for the data coming from the GATE simulations. This algorithm was modified and prepared for analysis of the experimental data. All steps of post-processing analysis are explained in details in the text below.

Coordinates of two hits position of interaction with scintillator ((x_1, y_1) and (x_2, y_2)) were used to define line-of-response for a given event as one can see in Fig. 7.22. Based on these coordinates, it is possible to formulate the equation of the straight line passing through these two points. It is easy to calculate parameters a and b of the line:

$$a = \frac{y_1 - y_2}{x_1 - x_2} \quad (7.35)$$

$$b = y_1 - ax_1 \quad (7.36)$$

In the general form the LOR equation can be written in the following form:

$$Ax + By + C = 0 \quad (7.37)$$

for which:

$$B = 1 \quad (7.38)$$

$$A = -a \quad (7.39)$$

$$C = -b \quad (7.40)$$

To create a sinogram it is necessary to find the radial offset r and the angle ϕ as it was described in Sec. 2.4. The radial offset is the distance between the center of the detector (x_0, y_0) and the LOR (x_r, y_r) as one can see on right panel of Fig. 7.22:

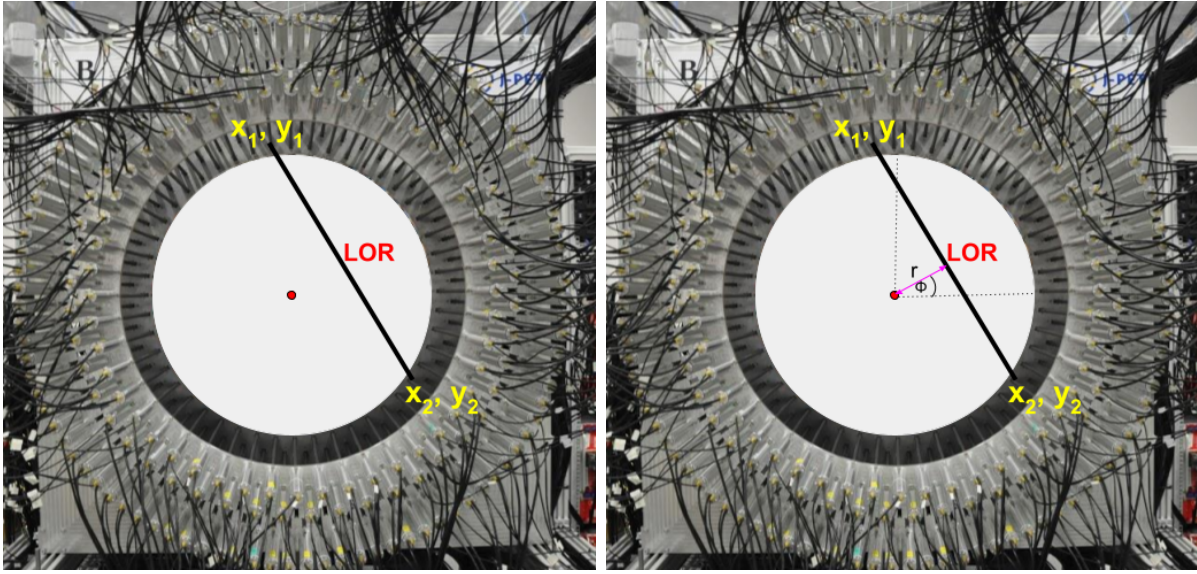


Figure 7.22: (left) LOR defines as a line between two interaction points. (right) Conversion from line-of-response to the sinogram format.

$$r = \sqrt{x_r^2 + y_r^2} \quad (7.41)$$

where:

$$x_r = \frac{B(Bx_0 - Ay_0) - AC}{A^2 + B^2} = \frac{-b}{a + \frac{1}{a}} \quad (7.42)$$

$$y_r = \frac{A(-Bx_0 - Ay_0) - BC}{A^2 + B^2} = -\frac{1}{x} \cdot x_r \quad (7.43)$$

The angle ϕ can be calculated from the formula:

$$\phi = \text{atan2}(y_r, x_r) \quad (7.44)$$

Each slice was defined in the same way as for analysis of the data gathered with PET Sensitivity Phantom. The only difference is that each scintillator was divided into one hundred parts along the scintillator length and, hence, the axial field-of-view equal to 50 cm was taken into account. Each line-of-response was transformed to the sinogram format according to the calculations presented above and assigned to a given slice with a Single Slice Rebinning (SSRB) method. In this technique, each LOR is assigned axially to the transaxial plane lying exactly in the midway between two detectors which register gamma quanta in a coincidence mode and as result a set of 2D sinograms is created [151, 159–162]. Graphical explanation is shown in Fig. 7.23. This technique works good only if line source position is parallel to scanner's axis and can speed up the calculations because only two dimensional sinograms are processed instead of a big set of three dimensional sinograms.

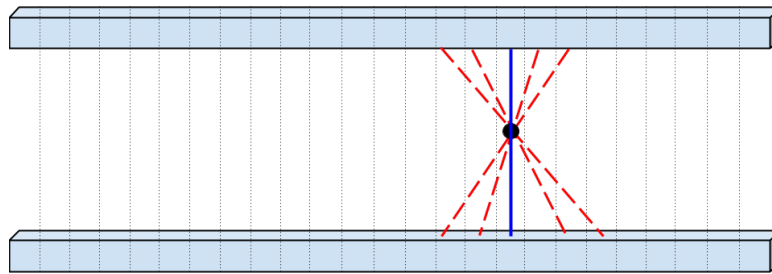


Figure 7.23: Each scintillator was divided into one hundred parts along its length. The red dashed lines show the LORs which correspond to emission slice represented as blue solid line. Each LOR is assigned to a given transaxial slice if it intersects axial midpoint of a given slice. Figure drawn based on [161].

All pixels, located at a distance larger than 12 cm from the center of transaxial FOV, were set to zero according to analysis instruction included in the NEMA norm. In the next step, all sinograms were aligned and summed up into one final sinogram shown in left panel of Fig. 7.24, and a sum projection was produced from the final sinogram.

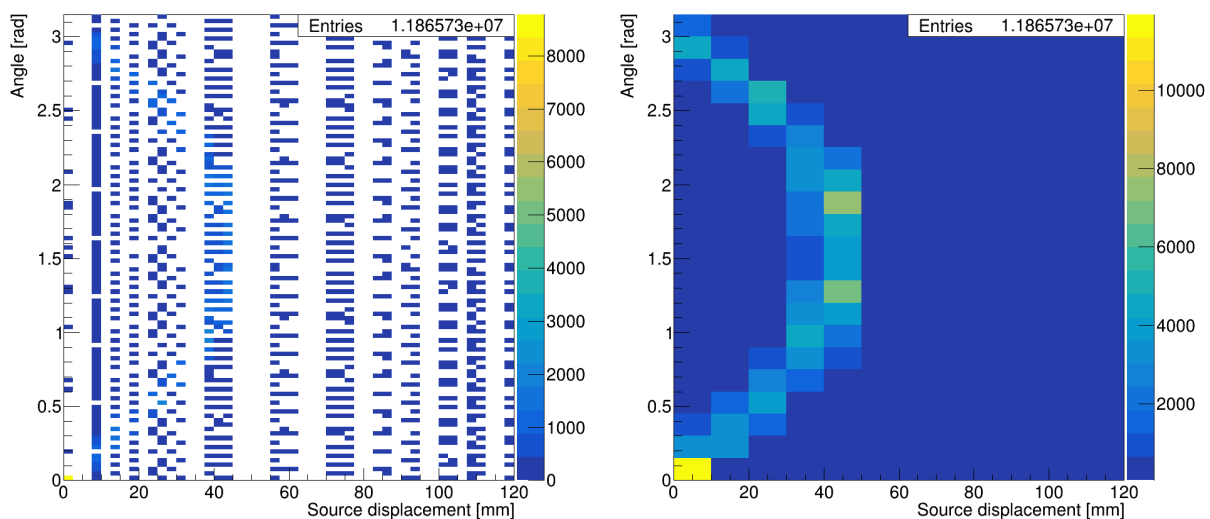


Figure 7.24: (right) Each LOR was transformed to the sinogram format and assigned to a given slice with a Single Slice Rebinning (SSRB) method. Final sinogram was obtained as a sum of all aligned sinograms. (left) Final sinogram was rebinned in the ROOT environment to highlight the visible shape. This sinogram was not used in further analysis.

The value of counts per pixel from left and right side of the projection profile at ± 20 mm from the sinogram center (see Fig. 3.3) were calculated based on linear interpolation between two nearest pixels as one can see in right panel of Fig. 7.25.

Parameters of linear interpolation were calculated in the same way as for measurements

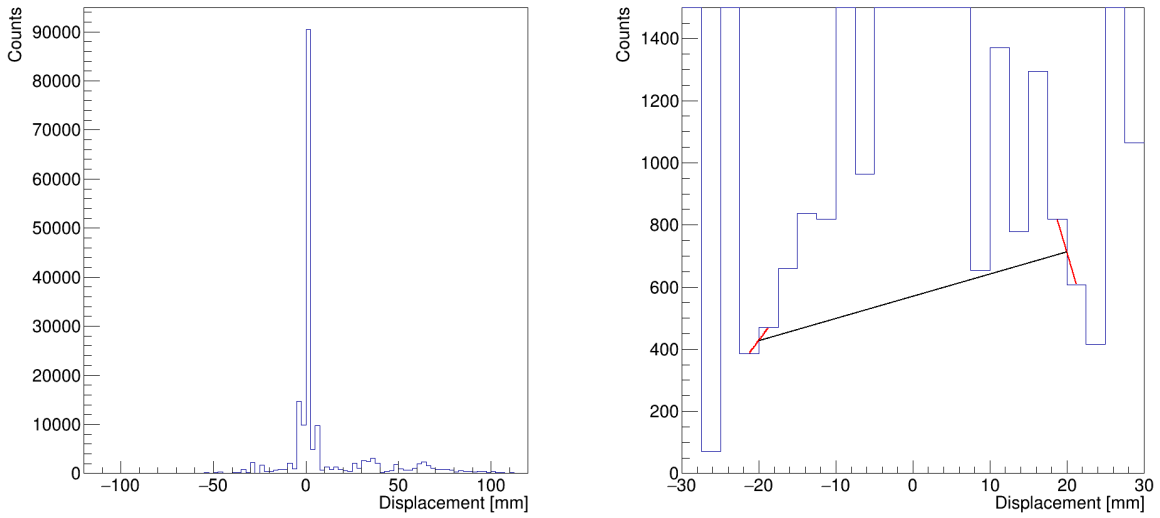


Figure 7.25: (right) Projection profile drawn over final sinogram. (left) Linear interpolation between two nearest bins at ± 20 mm.

with point sources and PSF estimation (see Fig. 7.16). Based on Eq. 7.23 and Eq. 7.24 and substituting ± 20 mm for x_{left} and x_{right} , respectively, one can obtain number of counts per pixel:

$$C_L = 428 \text{ counts} \quad (7.45)$$

$$C_R = 713 \text{ counts} \quad (7.46)$$

NEMA norm suggest to multiply average value of C_L and C_R by the number of pixels and add this product to the integral of counts outside the ± 20 mm region. However, in this work, to obtain number of random and scattered counts (C_{r+s}) a sum of surface area of the rectangle and triangle under the line can be calculated and added to the integral of outside counts (see Fig. 7.26). This approach is more precise than the solution proposed in the NEMA norm. Number of counts in central region (inside the ± 20 mm area) is equal to:

$$C_{central} = 22821 \pm 152 \text{ [counts]} \quad (7.47)$$

while number of counts outside this region is equal to:

$$C_{side} = 41644 \pm 268 \text{ [counts]} \quad (7.48)$$

The total number of counts was calculated as the integral of the full projection profile. The uncertainty of number of counts in all cases was calculated as a square root of number of counts.

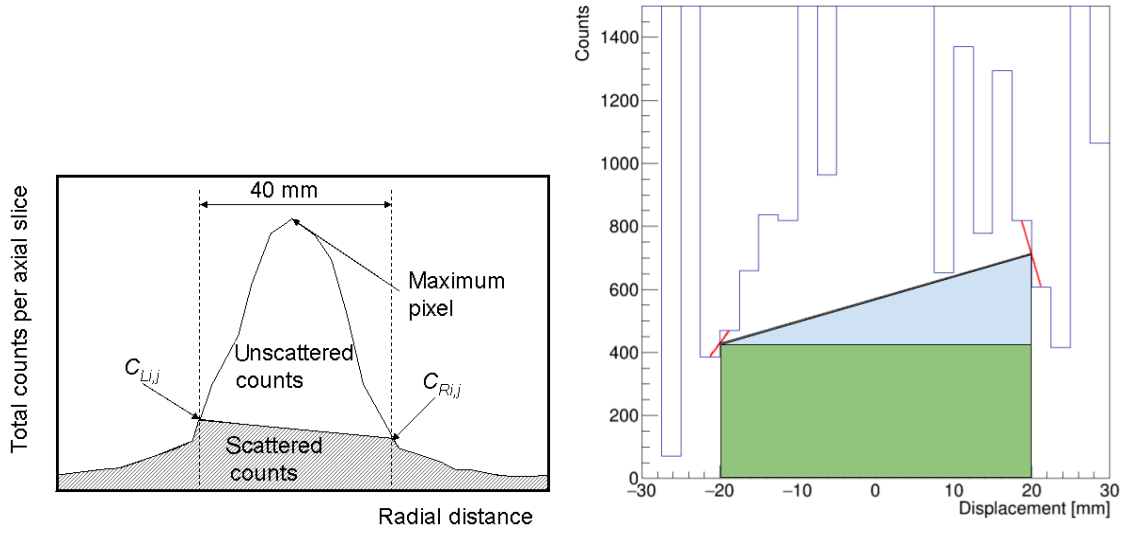


Figure 7.26: (left) Projection sum profile with the ± 20 mm range marked. Average value of C_L and C_R is multiplied by number of pixels to obtain number of scattered counts. Figure adapted from [96]. (right) Number of scattered counts is calculated as a sum of the area of rectangle (green) and triangle (blue) under the line connecting C_L and C_R .

$$C_{TOT} = 182074 \pm 427 \text{ [counts]} \quad (7.49)$$

Scatter fraction was calculated according to the instruction for system without possibility of random coincidences measurement:

$$SF = \frac{C_{r+s}}{C_{TOT}} = 35.41 \pm 0.19[\%] \quad (7.50)$$

The uncertainty of the scatter fraction was calculated from the error propagation law as:

$$\Delta SF = \sqrt{\frac{\Delta C_{central}^2}{C_{TOT}^2} + \frac{\Delta C_{side}^2}{C_{TOT}^2} + \left(-\frac{C_{central} + C_{side}}{C_{TOT}}\right)^2 \Delta C_{TOT}^2} \quad (7.51)$$

Based on the number calculated above, it was also possible to estimate total event rate (R_{TOT}), true event rate (R_t), random event rate (R_r) and scatter event rate (R_s).

$$R_{TOT} = \frac{1}{T_{acq}} C_{TOT} = 2.7442 \pm 0.0065 \left[\frac{\text{counts}}{\text{s}} \right] \quad (7.52)$$

where T_{acq} stands for the acquisition time equal to 66348 s. This time was calculated exactly in the same way as for measurements with the PET Sensitivity Phantom.

$$R_t = \frac{1}{T_{acq}} (C_{TOT} - C_{r+s}) = 1.773 \pm 0.012 \left[\frac{\text{counts}}{\text{s}} \right] \quad (7.53)$$

$$R_r = R_{TOT} - \frac{R_t}{1 - SF} = -0.001s \pm 0.027 \left[\frac{\text{counts}}{s} \right] \quad (7.54)$$

$$R_s = \frac{SF}{1 - SF} R_t = 0.972 \pm 0.011 \left[\frac{\text{counts}}{s} \right] \quad (7.55)$$

Uncertainties of above parameters were calculated according to the error propagation law. Result of random event rate show up that there was almost no random events detected in this measurement.

The last parameter included in the NEMA norm is the noise equivalent count rate:

$$R_{NEC} = \frac{R_t^2}{R_{TOT}} = 1.145 \pm 0.016 \left[\frac{\text{counts}}{s} \right] \quad (7.56)$$

Due to the single long acquisition it was not possible to determine these parameters as a function of average concentration of the effective activity of the radiotracer and to report peaks of true count rate ($R_{t,peak}$) and noise equivalent count rate ($R_{NEC,peak}$). There is also no point to estimate the average radioactivity concentration. Moreover, all parameters presented above were estimated from a single sinogram instead of set of sinograms from a set of acquisitions. Each formula has been adapted to the measurement conditions.

Chapter 8

Summary and results discussion

The results of determination of performance characteristics of the J-PET tomograph are presented in this thesis. Studies were performed according to the NEMA NU-2 2012 standard which defines measurement procedure and data processing standards. This norm provides consistent estimation and reporting of the performance parameters of the Positron Emission Tomographs available worldwide and allows to compare these parameters between different manufacturers.

8.1 Sensitivity

Sensitivity measurements were performed with PET Sensitivity Phantom at position (0,0) and (0,10) [cm] along detector x - and y -axis. Five different measurements were performed for each position according to five different combined thickness of the phantom. The radionuclide used in this performance tests was ^{68}Ge instead of suggested ^{18}F which was motivated by studies presented in [112].

The corrected activity of the source used during measurements was calculated, but in the final approach it was decided to use real value of the source activity due to the source dimension, which covered fully the detector axial field-of-view.

Measurement acquisition time was an important parameter in case of estimation of count rate with no attenuation. The real measurement duration was estimated based on the number of time windows for a given FPGA clock frequency. The accuracy of this estimation was on the levels of seconds.

Literature studies presents system sensitivity on the level of $13.82 \frac{\text{cps}}{\text{kBq}}$ and $17.83 \frac{\text{cps}}{\text{kBq}}$ for the 0 and 10 cm-off-center, respectively, for CareMiBrain, a dedicated brain PET scanner developed by Oncovision in Spain [163]. In case of GE Healthcare Discovery MI PET/CT and Discovery MI-DR TOF PET/CT systems the sensitivity is equal to $13.3 \frac{\text{cps}}{\text{kBq}}$ and $6.3 \frac{\text{cps}}{\text{kBq}}$ for the central field-of-view and $13.4 \frac{\text{cps}}{\text{kBq}}$ and $6.8 \frac{\text{cps}}{\text{kBq}}$ for the 10 cm radial

offset, respectively [164]. Sensitivity is equal to $20.080 \frac{\text{cps}}{\text{kBq}}$ and $20.121 \frac{\text{cps}}{\text{kBq}}$ for the center and 10 cm radial offset for the Discovery IQ system [165].

The sensitivity results for the J-PET system for 0 and 10 cm radial offset are equal to $0.130 \pm 0.014 \frac{\text{cps}}{\text{kBq}}$ and $0.0789 \pm 0.0061 \frac{\text{cps}}{\text{kBq}}$, respectively. Big difference between results obtained from literature studies, measurements and simulation comes from different J-PET detector geometry. Measurements were performed with J-PET detector build of 192 scintillator strips, but there are a lot of gaps between them. In simulations a total body J-PET detector was implemented with a double layer of scintillators with additional WLS strips and full cylindrical coverage. Moreover, the simulated system has larger axial field-of-view. For the full version of the J-PET system the results obtained from simulations and published by P. Kowalski et al. in [5] shown sensitivity on the level of $38 \frac{\text{cps}}{\text{kBq}}$ for the center of the tomograph.

Low sensitivity of the J-PET detector was improved with the new prototype described in Ch. 9 and will be further enhanced by utilizing two detection layers instead of one. The other limitation is the scintillator material. In case of crystals the detection efficiency can be increased by thickness increase to even 70% for single detection and 50% for detection in coincidence mode [166]. In case of plastic scintillators, the efficiency is on the level $\sim 20\%$, but there are plans to increase scintillator thickness to 30 mm and the number of layers in future prototype and therefore to increase detection efficiency [167]. Moreover, increase of the axial field-of-view can also increase the system sensitivity as it was mentioned before. Results of the simulations are promising and the proposed solutions will be introduced and tested in next versions of the J-PET detector [5, 167].

8.2 Spatial resolution

Detector spatial resolution was estimated based on measurements with point source placed in six positions parallel to the tomograph long axis specified by the NEMA norm:

- at the center of the axial field-of-view (FOV) and at the three-eighths of the axial FOV calculated from the FOV center,
- at 1 cm, 10 cm and 20 cm in the transverse direction.

Data acquired at each position was collected separately. The radionuclide used in this tests was ^{22}Na instead of suggested ^{18}F , but literature studies presents the growing importance and use of sodium radioactive source in daily control routine. Due to slightly different energy emission spectrum between ^{22}Na and ^{18}F , a ^{22}Na becomes a good candidate to replace ^{18}F in spatial resolution measurements.

Data from each measurement was preselected and reconstructed with Filtered Back Projection in relation to the instruction included in the norm. Studies of different reconstruction filters and cutoff values were performed. The best results were obtained for the Ridgelet filter and cutoff value equal to 3.0. In post-processing analysis the one-dimensional response function was drawn through the distribution peak for all three directions for each measurement position. The maximum value for each profile along x - and y -axis was determined by parabolic fit to the highest bin and two adjacent bins. The FWHM value was determined by linear interpolation at one half of this maximum value. To determine FWHM value along z -axis, a Gaussian Fitting Function was used.

Table 8.1: Spatial resolution of different PET systems [94, 168]. Spatial resolution values for the J-PET detector were averaged over axial positions for 1, 10 and 20 cm offset.

Spatial resolution	Distance [cm]	J-PET [cm]	Celesteion PET/CT [cm]	Discovery MI PET/CT 3 Rings [cm]	Biograph mCT Flow PET/CT [cm]
tangential	1	0.635 ± 0.092	0.47	0.436	0.433
radial	1	0.280 ± 0.092	0.45	0.465	0.433
axial	1	3.850 ± 0.028	0.44	0.447	0.425
tangential	10	0.715 ± 0.092	0.48	0.475	0.472
radial	10	0.500 ± 0.092	0.46	0.554	0.516
axial	10	3.667 ± 0.048	0.46	0.544	0.585
tangential	20	0.630 ± 0.092	0.53	0.518	0.648
radial	20	0.445 ± 0.092	0.58	0.741	0.555
axial	20	3.788 ± 0.053	0.47	0.578	0.780

Comparison of the spatial resolution between the J-PET detector and scanners available on the market one can find in Tab. 8.1. Measurements with different PET systems presented in the table were performed according to the NEMA NU-2 2012 norm. Tangential, radial and axial resolution for radius equal to 1, 10 and 20 cm was averaged over both axial positions according to the report instruction included in the norm. The biggest difference between the J-PET tomograph and commercial scanners is visible for the axial value of spatial resolution. Worse value of spatial resolution along z -axis of the J-PET detector comes from different geometry and used materials in comparison to commercial one. Axially arranged long plastic scintillators have smaller efficiency and negligible cross-section for the photoelectric effect on the contrary to the radially arranged crystals.

Detector width has significant impact on spatial resolution [145]. Spatial resolution along x - and y -axis is of the same order for J-PET detector and commercial ones. Especially radial spatial resolution of the J-PET detector is comparable or even better in comparison to other PET scanners presented in the table.

Axial spatial resolution of the J-PET detector can be improved by the wavelength-shifting (WLS) arrays. Tests performed by the J-PET group gave results of spatial resolution of 5 mm along the scintillation strip [131, 169, 170]. Axial sensitivity can be also improved by decreasing scintillator length or by replacing vacuum photomultiplier tubes by silicon photomultipliers. This solutions are and will be tested in future prototypes [125].

8.3 Scatter fraction

Scatter fraction measurements were performed with the PET Scatter Phantom placed at the dedicated bed and centered at the field-of-view centre. The insert with an radioactive source was placed with an 4.5 cm offset in the bed direction and centered according to the detector axial FOV. Measurements were performed with ^{68}Ge radioactive source instead of suggested ^{18}F . Germanium source is more often used in system calibration or daily quality control instead of measurements of scatter fraction, but it is possible to find literature studies of measurements with ^{68}Ge and PET Scatter Phantom [157, 171, 172]. Moreover, the activity of ^{68}Ge source found in the literature (eg. 6.4 MBq in [157]) was similar to the activity of the source at the day of measurement with the J-PET detector (8.49 MBq). In studies performed by Paulo R. R. V. Caribe et al., authors shown that the count rates of prompt photons, as well as true, random and scatter coincidences were lower for the same effective activity concentration for ^{68}Ga in comparison to results for ^{18}F as one can see in Fig. 8.1.

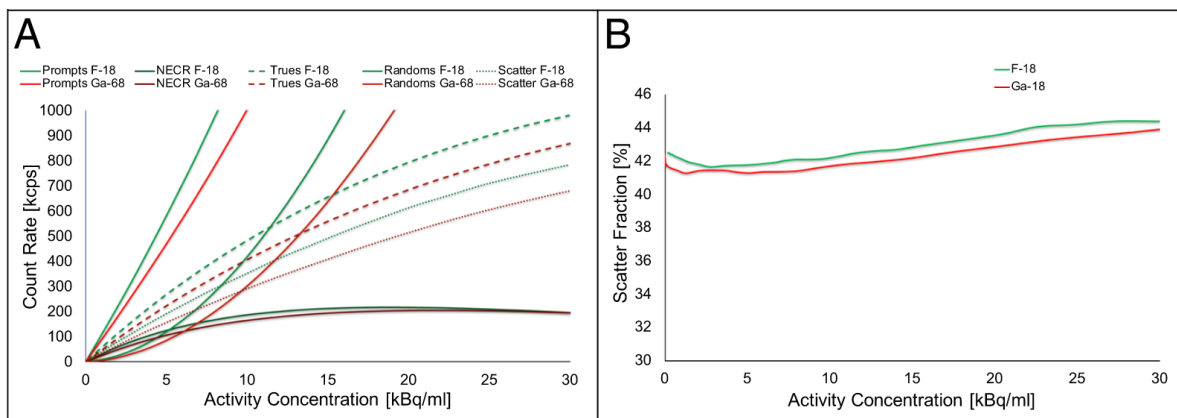


Figure 8.1: Count rates (left) and scatter fraction (right) for different activity concentration of ^{68}Ga and ^{18}F . Figure adapted from [112].

Data during measurement was collected as a single acquisition with 19 hours duration. Collected data was preselected and analyzed with a post-processing algorithm. A single sinogram was generated for each slice with Single Slice Rebinning method. In next step, sinograms were summed up into one final sinogram which was analyzed according to data processing instruction included in the NEMA norm.

Comparison of the scatter fraction between the J-PET detector and scanners available on the market one can find in Tab. 8.2. Parameters such as total event rate, true event rate, random event rate or scatter event rate cannot be compared due to different measurement condition and single acquisition instead of set of measurements for different activity levels. There was no possibility to estimate these parameters as a function of average source activity.

Table 8.2: Scatter fraction of different PET systems [94, 165, 168].

Parameter	J-PET	Celesteion PET/CT [cm]	Discovery MI PET/CT 3 Rings	Biograph mCT Flow PET/CT	Discovery IQ
SF [%]	35.41 ± 0.19	37.3	41.7	33.5	37.94

There was also no possibility of peak true count rate or peak noise equivalent count rate estimation due to the same reasons. Besides this complications, the scatter fraction obtained for the J-PET detector is comparable to the commercial scanners. This result can be improved with measurements with ^{18}F and with the new prototype of the J-PET detector described in Ch. 9. These test will be performed in the future. Furthermore, simulations of realistic Total-Body J-PET detector present scatter fraction at the level of 38.8% which is still reasonable value [167].

Chapter 9

Prospects for development of the J-PET tomograph

The first total-body PET scanner has opened a new perspectives in patient diagnostics and treatment as well as in biomedical studies [173]. The uEXPLORER, with axial FOV equal to 194 cm, for the first time in the PET history can scan the entire body in a single acquisition. The main potential advantages of this system are faster and better imaging or usage of lower radiopharmaceutical dose as well as the possibility of total-body metabolism dynamics imaging. First tests of uEXPLORER revealed ~ 15 -60 times higher sensitivity in comparison to other PET scanners and ~ 3 mm spatial resolution [149]. On the other hand, the cost of a single total-body device can be a huge barrier to use it in clinical practice or even in research centres [4]. As one can see in Fig. 9.1, the main components of the price are SiPMs and scintillators costs. Thus, there is a cheaper solution which will enable the purchase of such device by all interested reaserch and hospital units [13].

There are few ideas presented for example in [4, 13] for cost decreasing and some of them can be found below:

- smaller scintillator thickness - scintillators are the most expensive components, even up to half of the device price. On the other hand, results presented in [174] shown that in case of LSO and $\text{LaBr}_3\text{:Ce}$ stopping power dropped with scintillator thickness from 66.2% (for 30 mm thickness) and 52.3% (50 mm) to 3.5% (5 mm) and 2.8% (10 mm), respectively. An advantage of using thinner crystals is improving the timing resolution up to 100-150 ps for scintillator thickness in range 3-10 mm [13].
- BGO as a detection material - BGO crystals has worst energy and timing resolutions due to light yield and scintillation time in comparison to LYSO, but it is characterized by an excellent attenuation coefficient and stopping power and has no intrinsic radiation. BGO can be at least twice cheaper than LSO, based on price pre-

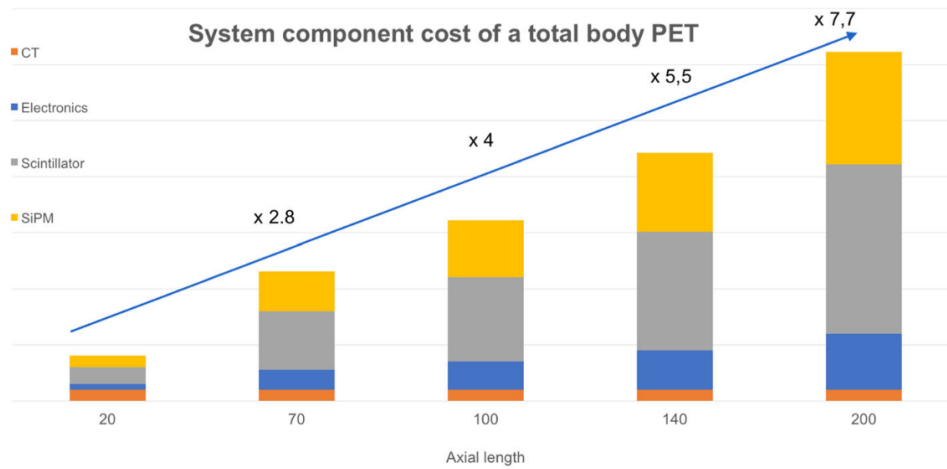


Figure 9.1: Estimated cost of specific components in relative units for different axial length versus 20 cm axial length. Figure adapted from [13].

sented on the Epic-Crystal website [175]. BGO can be easily grown in comparison to LSO or LYSO [176]. Design of low-cost and high-resolution PET based on BGO and SiPMs with 1 meter axial FOV was already presented in [177]. Results from tests of large BGO blocks ($50 \times 50 \times 15 \text{ mm}^3$) reported energy resolution better than 20% FWHM and DOI resolution equal to 5.3 mm FWHM [176]. Those results show that high-volume monolithic BGO crystals connected with SiPMs arrays can be used as PET detectors [176]. In the past BGO was considered as a worst candidate for TOF-PET system due to its long decay constant of 300 ns, but in recent years combination of event timing based on Cherenkov emission and energy discrimination have been reported as a potential solution for TOF-PET scanners [178]. BGO is the main competitor for L(Y)SO crystal, but nowadays is not commonly used in PET scanners due to important limitation of the coincidence timing resolution which for two currently operating scanners: Siemens Biograph Reveal 16 (LSO crystals) and GE Discovery-ST (BGO crystals) is equal to 0.5 ns and 5.8 ns, respectively [179,180].

- plastic scintillators - the main advantage of organic scintillators is their price (80 times less than LYSO), good timing properties and lower light attenuation [13]. On the other hand, their stopping power is much lower in comparison to crystals and this fact has to be also considered. Moreover, scatter coincidences discrimination is much more difficult due to Compton scattering which is the main process in the gamma quanta interactions with plastic scintillators. On the other hand, their design in a form of long strips may be used to create PET insert for existing and operating CT or MRI tomographs. Furthermore, long strips allow for significant reduction of required number of electronic channels [13]. Results of simulation per-

formed for a LYSO crystal with thickness equal to 1.81 cm (exactly the same size as in the case of uEXPLORER) and plastic scintillator with the thickness equal to 6 cm presented in [181] has shown that sensitivity gain increases more than twentyfold for total body PET based on plastics in comparison to current whole-body PET scanners based on LYSO crystals (see Fig. 9.2).

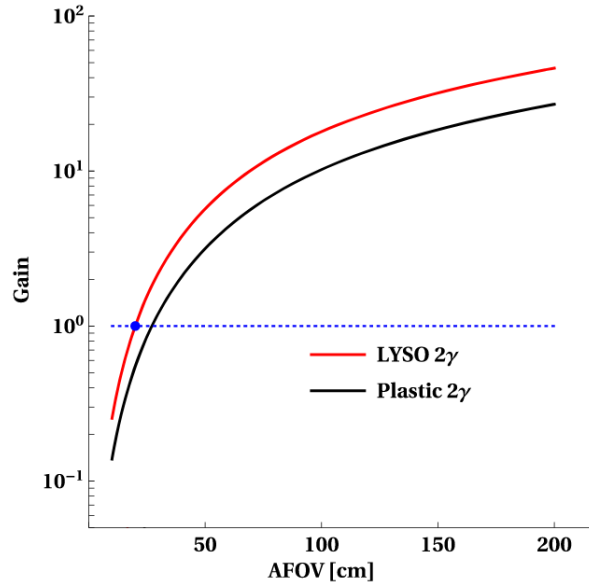


Figure 9.2: Relative sensitivity gain in function of axial field-of-view for standard 2γ presented for LYSO crystals and plastic scintillators. Blue dotted line stands for sensitivity gain for PET based on LYSO crystals with AFOV=20 cm and for standard 2γ imaging. Figure adapted from [181].

Based on experience with the J-PET prototype described in this thesis, a novel modular J-PET tomograph is currently under development. Modular J-PET prototype consists of 24 detection modules. One module is build of 13 plastic scintillators (BC-404) with dimensions equal to $6 \times 25 \times 500 \text{ mm}^3$ each. The main advantages of BC-404 scintillators are their high light output (68% Anthracene), good timing properties (0.7 ns rise time and 1.8 ns decay time) as well as good light attenuation length equal to 140 cm [60]. Each scintillator is wrapped with 3-M Vikuiti Enhanced Specular Reflector and DuPont B Kapton foils. The 3-M Vikuiti ESR is ultra-high reflectivity and non-metallic film while Kapton is a black light-tight foil which provides good protection from daylight [182–184]. Each scintillator is read-out at both ends by a matrix of four ($6 \times 6 \text{ mm}^2$) Hamamatsu silicon photomultipliers (model S13361). Signals registered by the modular J-PET prototype are probed in voltage domain by the FPGA based MVT system and collected by triggerless data acquisition system [4].

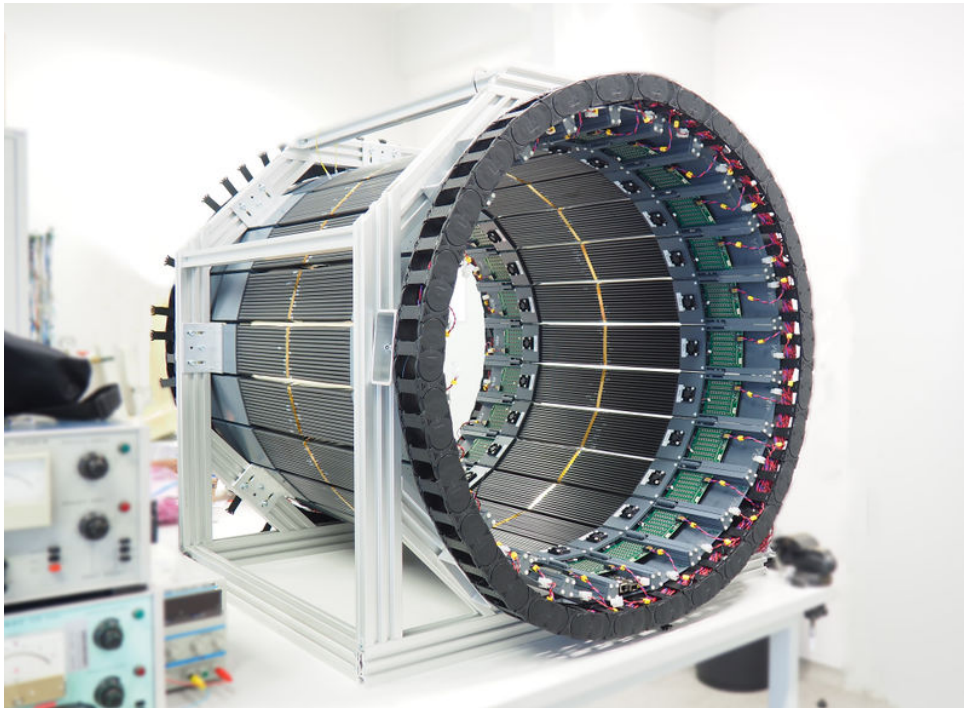


Figure 9.3: Photography of modular J-PET scanner with 50 cm AFOV. Weight of this prototype is equal to about 60 kg what makes it mobile and portable [4]. Figure courtesy of J-PET group.

This technology can be easily used to build a cost-effective total-body scanner, an extended version of the whole-body modular J-PET. J-PET design allows to use axially arranged scintillators strips with length up to 2.5 m, in contrary to radially arranged crystals used in commercial PET devices. Modular J-PET prototype showed that it is possible to build light and portable scanner which can be easily reconfigured and customized to existing CT or MRI devices or even customized to patients with clinical obesity [4].

Price of the uEXPLORER is a serious barrier for hospitals and, moreover, purchase of this device is unreachable for developing countries, even in Europe. Thus, the only solution is drastic price reduction for which, unfortunately, the BGO application in PET devices will not provide satisfactory results. Future of the cost-effective PET diagnostics lies in plastic scintillators and implementation of the J-PET idea.

Chapter 10

Conclusions

The main aim of the thesis was to determine performance characteristics of the J-PET tomograph. Jagiellonian Positron Emission Tomography scanner is a prototype build from 192 plastic scintillators. Scintillators, divided into three axially arranged layers, form a cylindrical chamber [1–7]. J-PET detector is optimized for detection of back-to-back gamma quanta coming from electron-positron annihilations. Those gamma quanta interact with plastic scintillator predominantly via Compton scattering. Produced in this way light signals are detected by two photomultipliers placed at two opposite ends of each scintillator strip. The use of plastic scintillators is an innovative concept and their low price in comparison to commercially used crystals opened a perspective for construction of cost-effective total-body PET scanner. Determination of the J-PET detector performance characteristics is needed in order to check its competitiveness with PET scanners available on the market and its possibility of clinical applications. Performance characteristics were estimated according to the NEMA NU 2-2012 norm, a world-wide standard for PET scanners. Detailed description of NEMA norm and J-PET scanner was presented in Ch. 3 and Ch. 4, respectively.

The J-PET detector required a dedicated calibrations as time and velocity calibration as well as an energy calibration. Time and velocity calibration play an important role in order to estimate with good accuracy the annihilation position. J-PET detector was successfully calibrated with a novel calibration method with a ^{22}Na source placed in a fixed position at the center of the detection system [121]. Calibration was based on measurements of time difference between annihilation and deexcitation photons. Energy calibration procedure was needed to align the gain between different photomultipliers [126]. This calibration procedure was performed based on data gathered with 5 sleeves of the PET Sensitivity Phantom with ^{68}Ge line source inside. Responses of all detection modules were equalized by resealing of the Compton edge values to the 340 keV. Calibration procedures and preselection conditions were presented in Ch. 6. Data selection criteria were focused

on decrease of the background originating from scattered and random coincidences.

Sensitivity of the J-PET detector was estimated based on results from measurements with the PET Sensitivity Phantom. Measurement duration was an important parameter in case of count rate estimation and a dedicated method which utilizes the number of time windows for a given FPGA clock frequency was applied. The obtained sensitivity values of the J-PET scanner for 0 and 10 cm radial offset are equal to $0.130 \pm 0.014 \frac{\text{cps}}{\text{kBq}}$ and $0.0789 \pm 0.0061 \frac{\text{cps}}{\text{kBq}}$, respectively.

Detector spatial resolution was estimated based on measurements with point source placed in six positions inside the J-PET detector. Data was collected for each source position separately and reconstructed with Filtered Back-Projection algorithm. Spatial resolution value vary between different positions and for 1 cm offset is equal to 0.635 ± 0.092 cm (tangential), 0.280 ± 0.092 cm (radial) and 3.850 ± 0.028 cm (axial), respectively. Spatial resolution for 10 cm offset is equal to 0.715 ± 0.092 cm (tangential), 0.500 ± 0.092 cm (radial) and 3.667 ± 0.048 cm (axial), respectively. Spatial resolution value is equal to 0.630 ± 0.092 cm, 0.445 ± 0.092 cm, 3.788 ± 0.053 cm for 20 cm axial position.

Scatter fraction value for the J-PET detector was estimated based on results obtained from measurement with the PET Scatter Phantom. Collected data was analyzed with Single Slice Rebinning method [185]. Scatter fraction for the J-PET system was determined as 35.41 ± 0.19 [%].

Detailed description of measurements and analysis performed by author of the thesis was presented in Ch. 5 and Ch. 7.

Low result of sensitivity obtained for the J-PET detector in comparison to commercial PET scanners is correlated with detector geometry and sparse arrangement of scintillators strips. On the other hand, tangential and radial spatial resolution of the J-PET system is of the same order as for commercial devices. Worse value of axial resolution comes from axially arranged plastic scintillators. Scatter fraction is at the same level as for scanners available on the market. Detailed discussion of the J-PET performance characteristics and their comparison to commercial PET scanners was presented in Ch. 8.

Limitations of the J-PET detector were improved with the new prototype described in Ch. 9. Modular J-PET scanner consists of 24 detection modules covered fully the axial field-of-view. There is almost no gaps between scintillators. Moreover, in this prototype the vacuum photomultipliers were replaced with silicon photomultipliers. Tests on the next generation of modules with WLS arrays gave promising results of axial spatial resolution on the level of 5 mm. New modules will be utilized with the next, Total Body version of the scanner. Sensitivity of the J-PET detector is worse in comparison to other scanners, but can be easily improved in future by utilizing of two detection layers, increase of axial field-of-view, increase of scintillator thickness and reduction of gaps between scintillators.

J-PET detector, described in this thesis, is the first full scale prototype of the PET scanner based on plastic scintillators. Presented results show that J-PET scanner can be a significant competitor in the PET market to the commercial PET scanners based on crystal technology.

List of Abbreviations

2D two dimensional
3D three dimensional
¹⁸FDG fluorodeoxyglucose
 Δt time difference
AFOV axial field-of-view
APD avalanche photodiode
BGO Bismuth Germanate
c speed of light
CT Computed Tomography
DAQ Data Acquisition
dSiPM digital SiPM
EC electron capture
FOV field-of-view
FPGA Field-Programmable Gate Array
FWHM full width at half maximum
FWTM full width at tenth-maximum
IEC International Electrotechnical Commission
J-PET Jagiellonian PET
JSON JavaScript Object Notation
LBS Lutetium (Lu) based scintillators
LOR line-of-response
LSO Lutetium Oxyorthosilicate
LVDS Low-Voltage Differential Signaling
LYSO Lutetium-Yttrium Oxyorthosilicate
MRI Magnetic Resonance Imaging
MVT Multi-Voltage Threshold
NEC noise equivalent count
NEMA National Electrical Manufacturers Association
PDE photon detection efficiency

PET Positron Emission Tomography
PHA pulse-height analyzer
PMT photomultiplier tube
PSF point spread function
SF scatter fraction
SiPM silicon photomultiplier
SNR signal-to-noise ratio
SSRB Single Slice Rebbining
TDC Time-to-Digital Converter
TOF time-of-flight
TOT time-over-threshold
TRB Trigger Read-out Board
U.S. United States
WHO World Health Organization

Bibliography

- [1] P. Moskal, Sz. Niedźwiecki, T. Bednarski, E. Czerwiński, Ł. Kapłon, E. Kubicz, I. Moskal, **M. Pawlik-Niedźwiecka**, N. G. Sharma, M. Silarski, M. Zieliński, N. Zoń et al. *Test of a single module of the J-PET scanner based on plastic scintillators. Nuclear Instruments and Methods in Physics Research A*, **764**:317–321, 2014.
- [2] P. Moskal, O. Rundel, et al. *Time resolution of the plastic scintillator strips with matrix photomultiplier readout for J-PET tomograph. Physics in Medicine and Biology*, **61**:2025–2047, 2016.
- [3] S. Niedźwiecki, ..., **M. Pawlik-Niedźwiecka** et al. *J-PET: A New Technology for the Whole-body PET Imaging. Acta Physica Polonica B*, **48**:1567–1576, 2017.
- [4] P. Moskal, E. Ł. Stępień. *Prospects and clinical perspectives of total-body PET imaging using plastic scintillators. PET Clinics*, **15 (4)**:439–452, 2020.
- [5] P. Moskal, P. Kowalski, R. Y. Shopa, L. Raczyński et al. *Simulating NEMA characteristics of the modular total-body J-PET scanner-an economic total-body PET from plastic scintillators. Physics in Medicine & Biology.*, **66 (17)**:175015, 2021.
- [6] P. Moskal, A. Gajos, M. Mohammed, ..., **M. Pawlik-Niedźwiecka**, et al. *Testing CPT symmetry in ortho-positronium decays with positronium annihilation tomography. Nature Communications*, **12**:5658, 2021.
- [7] P. Moskal, K. Dulski, ..., **M. Pawlik-Niedźwiecka**, et al. *Positronium imaging with the novel multiphoton PET scanner. Science Advances*, **7**:eabh4394, 2021.
- [8] A. Alavi, T. J. Werner, E. Ł. Stępień, P. Moskal. *Unparalleled and revolutionary impact of PET imaging on research and day to day practice of medicine. Bio-Algorithms and Med-Systems*, **17 (4)**:203–212, 2021.
- [9] Our World in Data. *Causes of Death*, <https://ourworldindata.org/causes-of-death#what-do-people-die-from>. (accessed January 20, 2022).

- [10] World Health Organization. *Cancer*, <https://www.who.int/news-room/fact-sheets/detail/cancer>. (accessed January 20, 2022).
- [11] Cancer Research UK. *Worldwide cancer risk factors*, <https://www.cancerresearchuk.org/health-professional/cancer-statistics/worldwide-cancer/risk-factors#heading-Zero>. (accessed January 20, 2022).
- [12] Cleveland Clinic. *PET Scan*, <https://my.clevelandclinic.org/health/diagnostics/10123-pet-scan>. (accessed January 20, 2022).
- [13] S. Vandenberghe, P. Moskal, J. S. Karp. *State of the art in total body PET*. *EJNMMI Physics*, **7 (1)**:35, 2020.
- [14] A. Berger. *How does it work? Positron emission tomography*. *BMJ*, **326 (7404)**:1449, 2003.
- [15] S. Basu, A. Alavi. *Revolutionary impact of PET and PET-CT on the day-to-day practice of medicine and its great potential for improving future health care*. *Nuclear Medicine Review*, **12 (1)**:1–13, 2009.
- [16] P. J. Slomka, T. Pan, G. Germano. *Recent Advances and Future Progress in PET Instrumentation*. *Seminars in Nuclear Medicine*, **46 (1)**:5–19, 2016.
- [17] Stanford Health Care. *What Is Positron Emission Tomography (PET) Scan?*, <https://stanfordhealthcare.org/medical-tests/p/pet-scan.html>. (accessed January 20, 2022).
- [18] Radiology Info. *Positron Emission Tomography - Computed Tomography (PET/CT)*, <https://www.radiologyinfo.org/en/info/pet#97f37e2b495d4ebf9e04656d8062e557>. (accessed January 20, 2022).
- [19] A. Kaushik, A. Jaimini, M. Tripathi et al. *Estimation of radiation dose to patients from (18) FDG whole body PET/CT investigations using dynamic PET scan protocol*. *Indian Journal of Medical Research*, **142 (6)**:721–731, 2015.
- [20] United States Environmental Protection Agency. *Radiation Sources and Doses*, <https://www.epa.gov/radiation/radiation-sources-and-doses>. (accessed January 20, 2022).
- [21] Joint Research Centre. Radioactivity Environmental Monitoring. *European Atlas of Natural Radiation*, <https://remon.jrc.ec.europa.eu/About/Atlas-of-Natural-Radiation/Download-page>. (accessed January 20, 2022).

- [22] New Choice Health. *How much does a PET scan cost?*, <https://www.newchoicehealth.com/pet-scan/cost>. (accessed January 20, 2022).
- [23] Agencja Oceny Technologii Medycznych i Taryfikacji, Wydział Taryfikacji. *"Pozytonowa tomografia emisyjna (PET)*, http://www.aotm.gov.pl/www/wp-content/uploads/2016/08/AOTMiT_WT_553_19_2015_PET_raport.pdf". 2016 (accessed June 25, 2018).
- [24] BioSkaner. *Cennik badań PET*, <https://bioskaner.eu/badania/pet-mr/cennik-badan-pet/>. (accessed January 20, 2022).
- [25] Medical Device and Diagnostic Industry. *5 of the most expensive medical devices*, <https://www.mddionline.com/business/5-most-expensive-medical-devices/gallery?slide=4>. (accessed January 20, 2022).
- [26] Heartland Imaging Centers. *Why Are MRIs So Expensive at Hospitals?*, <https://heartlandimagingcenters.com/2021/03/19/why-are-mris-so-expensive-at-hospitals/>. (accessed January 20, 2022).
- [27] P. Moskal. Matrix device and method for determining the location and time of reaction of the gamma quanta and the use of the device to determine the location and time of reaction of the gamma quanta in positron emission tomography, 2009-07-16. Patent number: PL 218733, EP 2454611, JP 5824773, US 8,969,817.
- [28] P. Moskal. Strip device and method for determining the location and time of reaction of the gamma quanta and the use of the device to determine the location and time of reaction of the gamma quanta in positron emission tomography, 2012-02-16. Patent number: EP 2454612, JP 5824774, US 8,859,973.
- [29] K. Szymański, P. Moskal, ..., **M. Pawlik**, et al. *Simulations of gamma quanta scattering in a single module of the J-PET detector*. *Bio-Algorithms and Med-Systems*, **10**:71, 2014.
- [30] N. G. Sharma, M. Silarski,..., **M. Pawlik-Niedźwiecka**, et al. *J-PET: A Novel TOF-PET scanner using organic scintillators*. *Journal of Chemical and Pharmaceutical Sciences. Special Issue*, **4**, 2016.
- [31] L. Raczyński, W. Wiślicki, W. Krzemień, P. Kowalski, ..., **M. Pawlik-Niedźwiecka**, et al. *Calculation of the time resolution of the J-PET tomograph using kernel density estimation*. *Physics in Medicine & Biology*, **62**:5076–5097, 2017.

- [32] W. Krzemień, M. Silarski, K. Stola, D. Trybek, ..., **M. Pawlik** et al. *J-PET analysis framework for the prototype TOF-PET detector*. *Bio-Algorithms and Med-Systems*, **10** (1):33–36, 2014.
- [33] E. Czerwiński, M. Zieliński, ..., **M. Pawlik**, et al. *Database and data structure for the novel TOF-PET detector developed for J-PET project*. *Bio-Algorithms and Med-Systems*, **10**:79, 2014.
- [34] P. Kowalski, L. Raczyński, ..., **M. Pawlik-Niedźwiecka**, et al. *Determination of the map of efficiency of the Jagiellonian Positron Emission Tomograph (J-PET) detector with the GATE package*. *Bio-Algorithms and Med-Systems*, **10**:85, 2014.
- [35] G. Korcyl, P. Moskal, ..., **M. Pawlik**, et al. *Trigger-less and reconfigurable data acquisition system for positron emission tomography*. *Bio-Algorithms and Med-Systems*, **10**:37–40, 2014.
- [36] A. Słomski, Z. Rudy, ..., **M. Pawlik**, et al. *3D PET image reconstruction based on the maximum likelihood estimation method (MLEM) algorithm*. *Bio-Algorithms and Med-Systems*, **10**:1–7, 2014.
- [37] W. Wiślicki, ..., **M. Pawlik**, et al. *Computing support for advanced medical data analysis and imaging*. *Bio-Algorithms and Med-Systems*, **10**:53, 2014.
- [38] M. Pałka, ..., **M. Pawlik** et al. *A novel method based solely on FPGA units enabling measurement of time and charge of analog signals in Positron Emission Tomography*. *Bio-Algorithms and Med-Systems*, **10**:41–45, 2014.
- [39] L. Raczyński, P. Moskal, P. Kowalski, W. Wiślicki, ..., **M. Pawlik-Niedźwiecka**, et al. *Novel method for hit-position reconstruction using voltage signals in plastic scintillators and its application to Positron Emission Tomography*. *Nuclear Instruments and Methods in Physics Research A*, **764**:186–192, 2014.
- [40] P. Białas, J. Kowal, A. Strzelecki, ..., **M. Pawlik**, et al. *List-mode reconstruction in 2D strip PET*. *Bio-Algorithms and Med-Systems*, **10**:9–12, 2014.
- [41] T. Bednarski, E. Czerwiński, P. Moskal, ..., **M. Pawlik**, et al. *Calibration of photomultipliers gain used in the J-PET detector*. *Bio-Algorithms and Med-Systems*, **10**:13–17, 2014.
- [42] P. Moskal, T. Bednarski, Sz. Niedźwiecki, M. Silarski, ..., **M. Pawlik-Niedźwiecka**, et al. *Synchronisation and calibration of the 24-modules J-PET prototype with 300 mm axial field of view*. *IEEE Transactions on Instrumentation and Measurement*, **70**:2000810, 2021.

- [43] P. Moskal, N. Zoń, et al. *A novel method for the line-of-response and time-of-flight reconstruction in TOF-PET detectors based on a library of synchronized model signals*. *Nuclear Instruments and Methods in Physics Research A*, **775**:54–62, 2015.
- [44] M. Skurzok, M. Silarski, ..., **M. Pawlik-Niedzwiecka**, et al. *Time calibration of the J-PET detector*. *Acta Physica Polonica A*, **132**:1641, 2017.
- [45] M. Dadgar, P. Kowalski. *Gate simulation study of the 24-module J-PET scanner: data analysis and image reconstruction*. *Acta Physica Polonica B*, **51**:309, 2020.
- [46] B. M. Fischer, B. A. Siegel, W. A. Weber, K. von Bremen, T. Beyer, A. Kalemis. *PET/CT is a cost-effective tool against cancer: synergy supersedes singularity*. *European Journal of Nuclear Medicine and Molecular Imaging*, **43 (10)**:1749–1752, 2016.
- [47] B. Mazoye. *PET in neurological research and diagnostics*. *Nuclear Medicine Review*, **15 (C)**:C17–C19, 2012.
- [48] S. Tavernier, A. Gektin, B. Grinyov, W. W. Moses. *Radiation Detectors for Medical Applications*. Springer, 2006.
- [49] G. B. Saha. *Basics of PET Imaging: Physics, Chemistry, and Regulations*. Springer, 2010.
- [50] S. D. Bass, S. Mariazzi, P. Moskal, E. Stępień. *Colloquium: Positronium physics and biomedical applications*. *Reviews of Modern Physics*, **95**, 2023.
- [51] S. R. Cherry, J. Sorenson, M. Phelps. *Physics in Nuclear Medicine*. Elsevier Health Sciences, 2003.
- [52] D. L. Bailey, D. W. Townsend, P. E. Valk, M. N. Maisey. *Positron Emission Tomography: Basic Sciences*. Springer, 2005.
- [53] S.R. Cherry, M. Dahlbom. *PET: Physics, Instrumentation, and Scanners*. Springer, 2006.
- [54] J. T. Bushberg, J. A. Seibert, E. M. Leidholdt, J. M. Boone. *The Essential Physics of Medical Imaging*. Lippincott Williams and Wilkins, 2002.
- [55] M. M. Khalil (ed.). *Basic Science of PET Imaging*. Springer, 2017.
- [56] C. W. E. Eijk. *Inorganic scintillators in medical imaging*. *Physics in Medicine & Biology*, **47**:R85, 2002.

- [57] Qwerty123uiop. *PhotoMultiplierTubeAndScintillator.svg*. Wikipedia, the free encyclopedia, 2013 (accessed July 9, 2018).
- [58] S. N. Ahmed. *Physics and Engineering of Radiation Detection*. Academic Press, 2007.
- [59] Eljen Technology. <https://eljentechnology.com/>. (accessed July 11, 2018).
- [60] Saint-Gobain Crystals. <https://www.crystals.saint-gobain.com/>. (accessed July 11, 2018).
- [61] C. Poole (ed.) P. Worsfold, A. Townshend. *Encyclopedia of Analytical Science*. Elsevier, 2005.
- [62] Hamamatsu. *Photomultiplier tubes. Photomultiplier tubes and related products. Product Catalogue*. 2010.
- [63] M. Dahlbom. *Physics of PET and SPECT Imaging*. CRC Press, Taylor & Francis Group, 2017.
- [64] S. R. Cherry, T. Jones, J. S. Karp, J. Qi, W. W. Moses, R. D. Badawi. *Total-Body PET: Maximizing Sensitivity to Create New Opportunities for Clinical Research and Patient Care*. *Journal of Nuclear Medicine*, **59** (1):3–12, 2018.
- [65] X. Zhang, J. Zhou, S. R. Cherry, R. D. Badawi, J. Qi. *Quantitative image reconstruction for total-body PET imaging using the 2-meter long EXPLORER scanner*. *Physics in Medicine & Biology*, **62** (6):2465–2485, 2017.
- [66] M. Wernick, J. Aarsvold. *Emission Tomography: The Fundamentals of PET and SPECT*. Academic Press, 2004.
- [67] A. Ciarmiello, L. Mansi (ed). *PET-CT and PET-MRI in Neurology: SWOT Analysis Applied to Hybrid Imaging*. Springer, 2016.
- [68] E. Berg, S. R. Cherry. *Innovations in Instrumentation for Positron Emission Tomography*. *Seminars in Nuclear Medicine*, **48** (4):311–331, 2018.
- [69] J. S. Karp. *Time-of-flight PET*. *PET Center of Excellence Newsletter*, **3** (4), 2006.
- [70] J. S. Karp, S. Surti, M. E. Daube-Witherspoon, G. Muehllehner. *Benefit of Time-of-Flight in PET: experimental and clinical Results*. *Journal of Nuclear Medicine*, **49** (3):462–470, 2008.

- [71] S. Surti, A. Kuhn, M. E. Werner, A. E. Perkins, J. Kolthammer, J. S. Karp. *Performance of Philips Gemini TF PET/CT scanner with special consideration for its time-of-flight imaging capabilities*. *Journal of Nuclear Medicine*, **48** (3):471–480, 2007.
- [72] GE Healthcare. *Discovery MI with LightBurst Digital 4-Ring Detector*, http://promed-sa.com/wp-content/uploads/2020/08/Discovery-MI-4Ring-Data-Sheet_DOC1700317.pdf. (accessed November 5, 2018).
- [73] Siemens Healthineers. *Biograph Vision. See a whole new world of precision*, https://www.ordineingegneripisa.it/obj/files/documenti/2018.2.23.10.46.26_834.pdf. (accessed November 5, 2018).
- [74] S. Vandenberghe, E. Mikhaylova, E. D’Hoe, P. Mollet, J. S. Karp. *Recent developments in time-of-flight PET*. *EJNMMI Physics*, **3** (1):3, 2016.
- [75] Philips. *Vereos Digital PET/CT. Online specifications*, <https://www.usa.philips.com/healthcare/product/HC882446/vereos-digital-petct-proven-accuracy-inspires-confidence/specifications>. (accessed November 26, 2018).
- [76] G. B. Saha. *Radiopharmaceuticals and Methods of Radiolabeling*. In: *Fundamentals of Nuclear Pharmacy*. Springer, 1992.
- [77] Bureau International des Poids et Mesures. *Table of radionuclides. Monographie BIPM-5*, <https://www.bipm.org/documents/20126/53814638/Monographie+BIPM-5+-+Volume+5+%282010%29.pdf/16dbe6ec-914a-9228-ed5a-8dcb9cea7de0>. (accessed November 27, 2018).
- [78] Table de Radionucléides. *123I*, lnhb.fr/nuclides/I-123_tables.pdf. (accessed May 3, 2023).
- [79] S. Vallabhajosula. *(18)F-labeled positron emission tomographic radiopharmaceuticals in oncology: an overview of radiochemistry and mechanisms of tumor localization*. *Seminars in Nuclear Medicine*, **37** (6):400–419, 2007.
- [80] A. Nagaki, M. Onoguchi, N. Matsutomo. *Patient weight-based acquisition protocols to optimize (18)F-FDG PET/CT image quality*. *Journal of Nuclear Medicine Technology*, **39** (2):72–76, 2011.
- [81] E. E. Kim, M.-C. Lee, T. Inoue, W.-H. Wong (ed.). *Clinical PET and PET/CT: Principles and Applications*. Springer, 2012.

- [82] J. Cabello, S. I. Ziegler. *Advances in PET/MR instrumentation and image reconstruction. The British Journal of Radiology*, **91** (1081), 2018.
- [83] M. A. Spurrier, P. Szupryczynski, K. Yang, A. A. Carey, C. L. Melcher. *Effects of Ca²⁺ Co-Doping on the Scintillation Properties of LSO:Ce. IEEE Transactions on Nuclear Science*, **55** (3):1178–1182, 2008.
- [84] J. W. Cates, C. S. Levin. *Advances in coincidence time resolution for PET. Physics in Medicine & Biology*, **61** (6):2255–2264, 2016.
- [85] S. R. Cherry, R. D. Badawi, J. S. Karp, W. W. Moses, P. Price, T. Jones. *Total-body imaging: Transforming the role of positron emission tomography. Science Translational Medicine*, **9** (381):eaaf6169, 2017.
- [86] S. R. Cherry. *The 2006 Henry N. Wagner Lecture: Of mice and men (and positrons)—advances in PET imaging technology. Journal of Nuclear Medicine*, **47** (11):1735–1745, 2006.
- [87] E. Berg et al. Physical performance of the first total-body explorer pet scanner and preclinical applications with mini-explorer systems. IEEE Medical Imaging Conference – Total-Body PET Imaging Workshop, 2018.
- [88] R. Badawi et al. Initial results from the world’s first total-body positron emission tomograph. RSNA Annual Meeting, 2018.
- [89] National Electrical Manufacturers Association (NEMA). *Standards Publication NU 2-2012: Performance Measurements of Positron Emission Tomographs*. NEMA, Rosslyn, VA, 2012.
- [90] International Electrotechnical Commission (IEC). *International Standard: Radionuclide imaging devices – Characteristics and test conditions – Part 1: Positron emission tomographs (IEC 61675-1)*. IEC, Geneva, Switzerland, 2008.
- [91] C. X. Wang, W. E. Snyder, G. Bilbro, P. Santago. *Performance evaluation of filtered backprojection reconstruction and iterative reconstruction methods for PET images. Computers in Biology and Medicine*, **28** (1):13–24, 1998.
- [92] K. Rakoczy. *Development of the Event Display and the adaptation of various image reconstruction algorithms for the J-PET tomography scanner*. Bachelor’s thesis, Jagiellonian University, 2017.

- [93] S. Michopoulou, E. O'Shaughnessy, K. Thomson, M. J. Guy. *Discovery Molecular Imaging Digital Ready PET/CT performance evaluation according to the NEMA NU2-2012 standard*. *Nuclear Medicine Communications*, **40 (3)**:270–277, 2019.
- [94] T. Kaneta, M. Ogawa, N. Motomura, H. Iizuka, T. Arisawa, A. Hino-Shishikura, K. Yoshida, T. Inoue. *Initial evaluation of the Celesteion large-bore PET/CT scanner in accordance with the NEMA NU2-2012 standard and the Japanese guideline for oncology FDG PET/CT data acquisition protocol version 2.0*. *EJNMMI Research*, **7 (1)**:83–95, 2017.
- [95] D. L. Bailey; J. L. Humm; A. Todd-Pokropek; A. van Aswegen (ed.). *Nuclear Medicine Physics: A Handbook For Teachers And Students*. International Atomic Energy Agency, 2015.
- [96] International Atomic Energy Agency. *Quality Assurance for PET and PET/CT Systems*. IAEA Human Health Series No. 1, 2009.
- [97] D. Vandendriessche, J. Uribe, H. Bertin, F. De Geeter. *Performance characteristics of siliconphotomultiplier based 15-cm AFOV TOF PET/CT*. *EJNMMI Physics*, **6 (1)**:8–25, 2019.
- [98] P. Moskal, T. Bednarski, et al. *Strip-PET: a novel detector concept for the TOF-PET scanner*. *Nuclear Medicine Review*, **15C**:68–69, 2012.
- [99] P. Moskal, P. Salabura, M. Silarski, J. Smyrski, J. Zdebik, M. Zieliński. *Novel detector systems for the Positron Emission Tomography*. *Bio-Algorithms and Med-Systems*, **7**:73–78, 2011.
- [100] P. Moskal, T. Bednarski, Sz. Niedźwiecki, M. Silarski, E. Czerwiński, T. Kozik, J. Chhokar, ..., **M. Pawlik-Niedźwiecka** et al. *Synchronization and Calibration of the 24-Modules J-PET Prototype With 300-mm Axial Field of View*. *IEEE Transactions on Instrumentation and Measurement*, **70**, 2021.
- [101] M. Pałka, P. Strzempek, G. Korcyl et al. *Multichannel FPGA based MVT system for high precision time (20 ps RMS) and charge measurement*. *Journal of Instrumentation*, **12**:P08001, 2017.
- [102] W. Krzemień, A. Gajos, K. Kacprzak, K. Rakoczy, G. Korcyl. *J-PET Framework: Software platform for PET tomography data reconstruction and analysis*. *SoftwareX*, **11**, 2020.

- [103] S. Sharma, et al. *J-PET detection modules based on plastic scintillators for performing studies with positron and positronium beams*. *Journal of Instrumentation*, **18**:C02027, 2023.
- [104] Sz. Niedźwiecki. *Double-strip prototype of polymer time-of-flight positron emission tomograph based on multi-level analog electronics*. PhD thesis, Jagiellonian University, 2019.
- [105] Hamamatsu. *R9800 Datasheet*, <https://www.hamamatsu.com/eu/en/product/type/R9800/index.html>. 2014 (accessed September 24, 2020).
- [106] G. Korcyl, ..., **M. Pawlik-Niedźwiecka** et al. *Evaluation of Single-Chip, Real-Time Tomographic Data Processing on FPGA SoC Devices*. *IEEE Transactions on Medical Imaging*, **37** (11):2526–2535, 2018.
- [107] W. Krzemień, ..., **M. Pawlik-Niedźwiecka**, et al. *Overview of the software architecture and data flow for the J-PET tomography device*. *Acta Physica Polonica B*, **47**:561, 2016.
- [108] G. Korcyl, ..., **M. Pawlik-Niedźwiecka**, et al. *Sampling FEE and Trigger-less DAQ for the J-PET Scanner*. *Acta Physica Polonica B*, **47**:491, 2016.
- [109] W. Krzemień, A. Gajos, A. Gruntowski, K. Stola, D. Trybek et al. *Analysis framework for the J-PET scanner*. *Acta Physica Polonica A*, **127**:1491, 2015.
- [110] Isotop Rosatom. *Germanium-68*. (accessed August 13, 2020).
- [111] A. Sanchez-Crespo. *Comparison of Gallium-68 and Fluorine-18 imaging characteristics in positron emission tomography*. *Applied Radiation and Isotopes*, **76**:55–62, 2013.
- [112] P. R. R. V. Caribe, M. Koole, Yves D’Asseler, Timothy W. Deller, K. Van Laere and S. Vandenberghe. *NEMA NU 2–2007 performance characteristics of GE Signa integrated PET/MR for different PET isotopes*. *EJNMMI Physics*, **6** (1), 2019.
- [113] B. E. Zimmerman, J. T. Cessna, R. Fitzgerald. *Standardization of $^{68}\text{Ge}/^{68}\text{Ga}$ Using Three Liquid Scintillation Counting Based Methods*. *Journal of Research of NIST*, **113** (5):265–280, 2008.
- [114] C. Le Loirec, C. Champion. *Track structure simulation for positron emitters of medical interest. Part I: The case of the allowed decay isotopes*. *Nuclear Instruments and Methods in Physics Research Section A*, **582** (2):644–653, 2007.

- [115] A. Gonzalez-Montoro, F. Sanchez, P. Bruyndonckx, G. Cañizares, J. M. Benlloch, A. J. Gonzalez. *Novel method to measure the intrinsic spatial resolution in PET detectors based on monolithic crystals. Nuclear Instruments and Methods in Physics Research Section A*, **920**:58–67, 2019.
- [116] Eckert and Ziegler. Isotope production. *Industrial Radiation Sources. Product Information*. 2008.
- [117] I. Bartosova, V. Slugen, J. Veternikova, S. Sojak, M. Petriska, A. Bouhaddane. *Non-destructive research methods applied on materials for the new generation of nuclear reactors. Journal of Physics: Conference Series*, **516**, 2014.
- [118] K. Gong, S. R. Cherry, J. Qi. *On the assessment of spatial resolution of PET systems with iterative image reconstruction. Physics in Medicine & Biology*, **61** (5):N193–202, 2016.
- [119] T. Murata, K. Miwa, N. Miyaji et al. *Evaluation of spatial dependence of point spread function-based PET reconstruction using a traceable point-like ^{22}Na source. EJNMMI Physics*, **3** (1):26, 2016.
- [120] S. Misciagna (ed.). *Positron Emission Tomography. Recent Developments in Instrumentation, Research and Clinical Oncological Practice*. IntechOpen, 2013.
- [121] K. Dulski, M. Silarski, P. Moskal. *A Method for Time Calibration of PET Systems Using Fixed beta+ Radioactive Source. Acta Physica Polonica B*, **51**:195, 2020.
- [122] Canon. Celesteion. Performance specifications, <https://us.medical.canon/download/ct-br-celesteion-specs>. (accessed April 3, 2020).
- [123] S. A. Nehmeh, Y. E. Erdi, H. Kalaigian, K. S. Kolbert, T. Pan, H. Yeung, O. Squire, A. Sinha, S. M. Larson, J. L. Humm. Correction for oral contrast artifacts in CT attenuation-corrected PET images obtained by combined PET/CT. *Journal of Nuclear Medicine*, **44** (12):1940–1944, 2003.
- [124] A. Strzelecki. *Image reconstruction and simulation of strip Positron Emission Tomography scanner using computational accelerators*. PhD thesis, Jagiellonian University, 2016.
- [125] P. Kowalski, W. Wiślicki, R.Y. Shopa, L. Raczyński, K. Klimaszewski, ..., **M. Pawlik-Niedźwiecka** et al. *Estimating the NEMA characteristics of the J-PET tomograph using the GATE package. Physics in Medicine & Biology*, **63**:165008, 2018.

- [126] S. Sharma, J. Chhokar, ..., **M. Pawlik-Niedźwiecka** et al. *Estimating relationship between the time over threshold and energy loss by photons in plastic scintillators used in the J-PET scanner. EJNMMI Physics*, **7**:39, 2020.
- [127] A. Osovizky, J. Paran, F. Vulasky et al. *Mathematical Calculation and Software Simulation of Positron Emitters Activity Concentration in a Duct. Conference of the Nuclear Societies in Israel*, 1999.
- [128] R. Biswas, H. Sahadath, A. Sattar Mollah, Md. Fazlul Huq. *Calculation of gamma-ray attenuation parameters for locally developed shielding material: Polyboron. Journal of Radiation Research and Applied Sciences*, **9 (1)**:26–34, 2016.
- [129] J. Zeb, W. Arshad, A. Rashid, P. Akhter. *Gamma shielding by aluminum (Al-shielder manual). Pakistan Institute of Nuclear Science and Technology*, 2010.
- [130] P. Kowalski, W. Wiślicki, L. Raczyński, ..., **M. Pawlik-Niedźwiecka** et al. *Scatter Fraction of the J-PET Tomography Scanner. Acta Physica Polonica B*, **47**:549, 2016.
- [131] **M. Pawlik-Niedźwiecka** et al. *Preliminary studies of J-PET detector spatial resolution. Acta Physica Polonica A*, **132**:1645, 2016.
- [132] Sz. Niedźwiecki. *Studies of detection of gamma radiation with use of organic scintillator detectors in view of positron emission tomography*. Master thesis, Jagiellonian University, 2011.
- [133] V. Bécares, J. Blázquez. *Detector Dead Time Determination and Optimal Counting Rate for a Detector Near a Spallation Source or a Subcritical Multiplying System. Science and Technology of Nuclear Installations*, 2012.
- [134] private correspondence, G.Korcył, Sz. Niedźwiecki, S. Sharma.
- [135] Ewelina Czaicka. *Liniowy model pozytonowego tomografu emisyjnego*. Master thesis, Jagiellonian University, 2008.
- [136] Y. Chu, M.-Y. Su, M. Mandelkern, O. Nalcioglu. *Resolution improvement in positron emission tomography using anatomical Magnetic Resonance Imaging. Technology in Cancer Research & Treatment*, **5 (4)**:311–317, 2006.
- [137] T. Hasegawa, K. Oda, Y. Wada et al. *Validation of novel calibration scheme with traceable point-like ^{22}Na sources on six types of PET scanners. Annals of Nuclear Medicine*, **27 (4)**:346–354, 2013.
- [138] K. Rakoczy. *Adaptation of image reconstruction algorithms with time-of-flight for the J-PET tomography scanner*. Master thesis, Jagiellonian University, 2019.

- [139] How Radiology Works. <https://howradiologyworks.com/filtered-backprojection-fbp-illustrated-guide-for-radiologic-technologists/>. (accessed January, 2023).
- [140] IAEA. Human Health Campus. 3D image reconstruction. <https://humanhealth.iaea.org/HHW/MedicalPhysics/NuclearMedicine/ImageAnalysis/3Dimagereconstruction/index.html>. (accessed March, 2023).
- [141] M. Lyra, A. Ploussi. *Filtering in SPECT Image Reconstruction*. *International Journal of Biomedical Imaging*, 2011.
- [142] Reconstruction. <http://oftankonyv.reak.bme.hu/tiki-index.php?page=Reconstruction>. (accessed March, 2023).
- [143] National Electrical Manufacturers Association (NEMA). *Standards Publication NU 2-2018: Performance Measurements of Positron Emission Tomographs*. NEMA, Rosslyn, VA, 2018.
- [144] M. Lyra, A. Ploussi, M. Rouchota, S. Synefia. *Filters in 2D and 3D Cardiac SPECT Image Processing*. *Cardiology Research and Practice*, 2014.
- [145] W. W. Moses. *Fundamental Limits of Spatial Resolution in PET*. *Nuclear Instruments and Methods in Physics Research A*, **648** (1):S236–S240, 2011.
- [146] D. Morimoto-Ishikawa, K. Hanaoka, S. Watanabe et al. *Evaluation of the performance of a high-resolution time-of-flight PET system dedicated to the head and breast according to NEMA NU 2-2012 standard*. *EJNMMI Physics*, **9** (1):88, 2022.
- [147] E. Prieto, J. M. Martí-Climent, J. Arbizu, P. Garrastachu, I. Domínguez, G. Quincoces, M. J. García-Velloso, P. Lecumberri, M. Gómez-Fernández, J.A. Richter. *Evaluation of spatial resolution of a PET scanner through the simulation and experimental measurement of the recovery coefficient*. *Computers in Biology and Medicine*, **40** (1):75–80, 2010.
- [148] A. M. J. Paans. *Positron emission tomography*, <https://cds.cern.ch/record/1005065/files/p363.pdf>. CERN, 2006 (accessed online March 10, 2022).
- [149] B. A. Spencer, E. Berg, J. P. Schmall, N. Omidvari, E. K. Leung, Y. G. Abdelhafez, S. Tang, Z. Deng, Y. Dong, Y. Lv, J. Bao, W. Liu, H. Li, T. Jones, R. D. Badawi, S. R. Cherry. *Performance Evaluation of the uEXPLORER Total-Body PET/CT Scanner Based on NEMA NU 2-2018 with Additional Tests to Characterize PET Scanners with a Long Axial Field of View*. *Journal of Nuclear Medicine*, **62** (6):861–870, 2021.

- [150] G. A. Prenosil, H. Sari, M. Furstner, A. Afshar-Oromieh, K. Shi, A. Rominger, M. Hentschel. *Performance Characteristics of the Biograph Vision Quadra PET/CT system with long axial field of view using the NEMA NU 2-2018 Standard*. *Journal of Nuclear Medicine*, **63** (3):476–484, 2022.
- [151] M. E. Daube-Witherspoon, J. S. Karp, M.E. Casey, F. P. DiFilippo, H. Hines, G. Muehllehner, V. Simcic, C. W. Stearns, L. E. Adam, S. Kohlmyer, V. Sossi. *PET performance measurements using the NEMA NU 2-2001 standard*. *Journal of Nuclear Medicine*, **43** (10):1398–1409, 2002.
- [152] J. F. Oliver, M. Rafecas. *Modelling Random Coincidences in Positron Emission Tomography by Using Singles and Prompts: A Comparison Study*. *PLoS One*, **11** (9):e0162096, 2016.
- [153] N. Belcari et al. *A novel random counts estimation method for PET using a symmetrical delayed window technique and random single event acquisition*. *2009 IEEE Nuclear Science Symposium Conference Record (NSS/MIC)*, pages 3611–3614, 2009.
- [154] D. Brasse, P. E. Kinahan, C. Lartizien, C. Comtat, M. Casey, C. Michel. *Correction methods for random coincidences in fully 3D whole-body PET: impact on data and image quality*. *Journal of Nuclear Medicine*, **46** (5):859–867, 2005.
- [155] J. F. Oliver, M. Rafecas. *Improving the singles rate method for modeling accidental coincidences in high-resolution PET*. *Physics in Medicine & Biology*, **55** (22):6951–6971, 2010.
- [156] M. M. Ahasan. *Evaluation of Scatter Fraction (SF) of a 16-Ring Positron Emission Tomography (PET) System*. *Bangladesh Journal of Medical Physics*, **4** (1):81–86, 2013.
- [157] T. W. Deller, M. M. Khalighi, F. P. Jansen, G. H. Glover. *PET Imaging Stability Measurements During Simultaneous Pulsing of Aggressive MR Sequences on the SIGNA PET/MR System*. *Journal of Nuclear Medicine*, **59** (1):167–172, 2018.
- [158] S. D. Sharma, R. Prasad, B. Shetye, V. Rangarajan, D. Deshpande, S. K. Shrivastava, K. A. Dinshaw. *Whole-body PET acceptance test in 2D and 3D using NEMA NU 2-2001 protocol*. *Journal of Medical Physics*, **32** (4):150–155, 2007.
- [159] C. Labbe. *Determination of a Set of Existing Algorithms For Comparative Evaluation*, https://stir.sourceforge.net/links/parapet/Task1_3.AlgorithmSurvey.pdf. 2004 (accessed May 3, 2023).

- [160] I. Buvat. *Tomographic reconstruction: a guided tour*, http://irene.guillemet.org/coursem/Recon_MAIA_2016.pdf. 2016 (accessed May 3, 2023).
- [161] K. M. A. Abushab. *Simulation and image reconstruction of clinical TOF-PET scanners*. PhD thesis, Universidad Complutense De Madrid, 2013.
- [162] Radiology Key. *PET Image Reconstruction: Methodology and Quantitative Accuracy*, <https://radiologykey.com/pet-image-reconstruction-methodology-and-quantitative-accuracy/>. (accessed May 3, 2023).
- [163] L. Moliner, M. J. Rodríguez-Alvarez, J. V. Catret et al. *NEMA Performance Evaluation of CareMiBrain dedicated brain PET and Comparison with the whole-body and dedicated brain PET systems*. *Scientific Reports*, **9**:15484, 2019.
- [164] A. Chicheportiche, R. Marciano, M. Orevi. *Comparison of NEMA characterizations for Discovery MI and Discovery MI-DR TOF PET/CT systems at different sites and with other commercial PET/CT systems*. *EJNMMI Physics*, **7 (1)**:4, 2020.
- [165] A. Jha, S. Mithun, A. Singh, N. Purandare, S. Shah, A. Agrawal, V. Rangarajan. *NEMA NU-2 2012 performance evaluation of Discovery IQ: A high sensitivity PET System*. *Journal of Nuclear Medicine*, **56 (3)**:1847, 2015.
- [166] L. Eriksson, D. Townsend, M. Conti, M. Eriksson, H. Rothfuss, M. Schmand, M. E. Casey, B. Bendriem. *An investigation of sensitivity limits in PET scanners*. *Nuclear Instruments and Methods in Physics Research Section A*, **580 (2)**:836–842, 2007.
- [167] J. Baran, W. Krzemień et al. *Realistic Total-Body J-PET Geometry Optimization—Monte Carlo Study*. *arXiv:2212.02285*, in review, 2023.
- [168] P. Carib, Y. D’Asseler, S. Vandenberghe, M. Koole, A. M. Marques da Silva, H. Bertin. *NEMA NU 2012 Performance Evaluation of the SiPM-Based and conventional PMT-based Time-of-Flight systems*. *Proceedings of the 24 Brazilian congress on medical physics*, XXIV Congresso Brasileiro de Física Medica, 2019.
- [169] J. Smyrski, D. Alfs, ..., **M. Pawlik-Niedźwiecka**, et al. *Measurement of gamma quantum interaction point in plastic scintillator with WLS strips*. *Nuclear Instruments and Methods in Physics Research Section A*, **851**:39–42, 2017.
- [170] J. Smyrski, D. Alfs, ..., **M. Pawlik**, et al. *Application of WLS strips for position determination in Strip PET tomograph based on plastic scintillators*. *Bio-Algorithms and Med-Systems*, **10**:59, 2014.

- [171] W. Lehnert, S. R. Meikle, S. Siegel, D. Bailey, R. Banati, A. B. Rosenfeld. *Evaluation of transmission methodology for the microPET Focus 220 animal scanner. Physics in Medicine & Biology*, **51 (16)**:4003–4016, 2006.
- [172] M. M. Ahasan, D. J. Parker. *Initial Results from a Prototype Large (2m) Ring PET Scanner. Proceedings of the World Congress on Engineering*, **1**, 2008.
- [173] R. D. Badawi, H. Shi, P. Hu, S. Chen, T. Xu, P. M. Price, Y. Ding, B. A. Spencer, L. Nardo, W. Liu, J. Bao, T. Jones, H. Li, S. R. Cherry. *First Human Imaging Studies with the EXPLORER Total-Body PET Scanner. Journal of Nuclear Medicine*, **60 (3)**:299–303, 2019.
- [174] S. Surti, M. E. Werner, J. S. Karp. *Study of PET scanner designs using clinical metrics to optimize the scanner axial FOV and crystal thickness. Physics in Medicine & Biology*, **58 (12)**:3995–4012, 2013.
- [175] EPIC Scintillator. <http://www.epic-scintillator.com/>. (accessed February 12, 2021).
- [176] A. Gonzalez-Montoro et al. *Highly improved operation of monolithic BGO-PET blocks. Journal of Instrumentation*, **12**:C11027, 2017.
- [177] Y. Zhang, W.-H. Wong. *System Design Studies for a Low-cost High-resolution BGO PET with 1-meter Axial Field of View. Journal of Nuclear Medicine*, **58 (1)**:221, 2017.
- [178] S. E. Brunner, D. R. Schaart. *BGO as a hybrid scintillator / Cherenkov radiator for cost-effective time-of-flight PET. Physics in Medicine & Biology*, **62 (11)**:4421, 2017.
- [179] M. I. Freedenberg, R. D. Badawi, A. F. Tarantal, S. R. Cherry. *Performance and limitations of positron emission tomography (PET) scanners for imaging very low activity sources. Physica Medica*, **30 (1)**:104–110, 2014.
- [180] C. L. Melcher. *Scintillation crystals for PET. Journal of Nuclear Medicine*, **41 (6)**:1051–1055, 2000.
- [181] P. Moskal, D. Kisielewska, Z. Bura, ..., **M. Pawlik-Niedźwiecka** et al. *Performance assessment of the 2gamma positronium imaging with the total-body PET scanners. EJNMMI Physics*, **7**:44–60, 2020.
- [182] 3M. <https://www.3m.com>. (accessed March 24, 2021).
- [183] Dupont. <https://www.dupont.com>. (accessed March 24, 2021).

-
- [184] Ł. Kapłon. *Technical Attenuation Length Measurement of Plastic Scintillator Strips for the Total-Body J-PET Scanner*. *IEEE Transactions on Nuclear Science*, **67** (10):2286–2289, 2020.
- [185] private correspondence, Sz. Parzych.